

ISSN 2587-1943

#14

VOLUME 7, 2
DECEMBER 2023

Editor-in-Chief
Niyazi Özdemir
Hikmet Esen

Deputy Editor-in-Chief
Abdullah Kapıcıoğlu

Managing Editor
Cihangir Kale

A

E

I

J

R

JOURNAL

INTERNATIONAL JOURNAL OF INNOVATIVE ENGINEERING APPLICATIONS



Editor-in-Chief

Prof. Dr. Niyazi ÖZDEMİR

Prof. Dr. Hikmet ESEN

Deputy Editor-in-Chief

Asst. Prof. Dr. Abdullah KAPICIOĞLU

Executive Editors

Prof. Dr. Messaoud SAIDANI

Prof. Dr. Niyazi BULUT

Prof. Dr. Kemal LEBLEBİCİOĞLU

Asst. Prof. Dr. Salwa BOUADILA

Managing Editor

Dr. Cihangir KALE

Subject Editors

Prof. Dr. Arif HEPBAŞLI

Prof. Dr. Asaf VAROL

Prof. Dr. Asım BALBAY

Prof. Dr. Elhoussine AZROUL

Prof. Dr. Engin AVCI

Prof. Dr. Fatih POYRAZ

Prof. Dr. Hacı Mehmet BAŞKONUŞ

Prof. Dr. Hasan TOĞRUL

Prof. Dr. İbrahim CAN

Prof. Dr. İnanç ÖZGEN

Prof. Dr. Mehmet EROĞLU

Prof. Dr. Murat KÖKSAL

Prof. Dr. Ömer YILDIRIM

Prof. Dr. Resul ÇÖTELİ

Prof. Dr. Şükrü TALAŞ

Prof. Dr. Tahir KHAN

Assoc. Prof. Dr. Alper POLAT

Assoc. Prof. Dr. Erkan BAHÇE

Assoc. Prof. Dr. Faruk KARACA

Assoc. Prof. Dr. Fethi DAĞDELEN

Assoc. Prof. Dr. Filiz ÖZGEN

Assoc. Prof. Dr. Özen ÖZER

Assoc. Prof. Dr. Reza BAKHTIARI

Assoc. Prof. Dr. Serdar MERCAN

Asst. Prof. Dr. Berivan YILMAZER POLAT

Asst. Prof. Dr. Fehmi ASLAN

Asst. Prof. Dr. Nagihan KARAASLAN AYHAN

Asst. Prof. Dr. Üyesi Ferit AK

Asst. Prof. Dr. Üyesi Yusuf DOĞAN

Asst. Prof. Dr. Vembu ANANTHASWAMY

Layout / Language Editor

M.Sc. Buğra ŞEN

Asst. Prof. Dr. Habip ŞAHİN

International Journal of Innovative Engineering Applications is published June and December.

Adress for the manuscripts and correspondence:

Uluslararası Yenilikçi Mühendislik Uygulamaları Dergisi
Firat Üniversitesi Kampüsü, Teknoloji Fakültesi, Merkez–Elazığ

Tel: +90 424 237 0000/ Ext.7655

e-mail: ijieatr@gmail.com

ISSN: 2587-1943

Elazığ-2023

#14

IJIEA

IJIEA

volume 7 issue 2

CONTENTS / İÇİNDEKİLER

Title / Başlık Author(s) / Yazar(lar)	Page(s) / Sayfa(lar)
IMPLEMENT OF LLRNET TO 5G-NR ON LINK-LEVEL SIMULATION <i>BAĞLANTI SEVİYESİ SİMÜLASYON ÜZERİNDE LLRNET'İN 5G-NR'YE UYGULANMASI</i> Bircan Çalışır <i>Research Article [en] Araştırma Makalesi [tr]</i>	158-163
GENETIC ALGORITHM BASED APPROACH FOR ALGORITHMIC TRADING IN FINANCIAL MARKETS <i>FİNANSAL PİYASALARDA ALGORİTMİK TİCARET İÇİN GENETİK ALGORİTMA TEMELİ YAKLAŞIM</i> Yunus Santur, Mustafa Ulaş, Murat Karabatak <i>Research Article [en] Araştırma Makalesi [tr]</i>	164-169
THE GEOMETRIES OF STABLE ISOTOPES IN TOOTH ENAMEL AND THEIR RADIATION CYCLES AND ARCHAEOLOGICAL SIGNIFICANCE <i>DİŞ MİNESİNDEKİ KARARLI İZOTOPLARIN GEOMETRİLERİ VE RADYASYON DÖNGÜLERİ VE ARKEOLOJİK ÖNEMİ</i> A. Bahar Mergen, Mücahit Yılmaz, Ezman Karabulut, Fatih Ahmet Çelik <i>Research Article [en] Araştırma Makalesi [tr]</i>	170-174
ENERGY CONSUMPTION FORECAST FOR THE BUILDING SECTOR IN TURKEY UNTIL 2030 <i>TÜRKİYE'DE 2030 YILINA KADAR BİNA SEKTÖRÜNDEKİ ENERJİ TÜKETİM TAHMİNİ</i> Nazile Yılankırkan, Esra Nur İçme <i>Research Article [en] Araştırma Makalesi [tr]</i>	175-181
A REGRESSION MODEL FOR FINDING OPTIMAL SOLAR PANEL INCLINATION ANGLES <i>OPTİMAL GÜNEŞ PANELİ EĞİM AÇILARINI BULMAK İÇİN BİR REGRESYON MODELİ</i> Mehmet Ali Kallioğlu <i>Research Article [en] Araştırma Makalesi [tr]</i>	182-187

IJIEA

volume 7 issue 2

CONTENTS / İÇİNDEKİLER

Title / Başlık Author(s) / Yazar(lar)	Page(s) / Sayfa(lar)
RESEARCHING THE PRODUCTION FEATURES OF SURGICAL INSTRUMENT MANUFACTURING WITH 3D PRINTING <i>CERRAHİ ALET İMALATININ 3 BOYUTLU YAZICI İLE ÜRETİM ÖZELLİKLERİNİN ARAŞTIRILMASI</i> <i>Fatma Nazlı Özsolak</i> <i>Research Article [en] Araştırma Makalesi [tr]</i>	188-194
NUMERICAL ANALYSIS OF DOUBLE GEOPOLYMER CONCRETE LAYER WITH DIFFERENT PROPERTIES <i>Berivan Yilmazer Polat</i> <i>Research Article [en] Araştırma Makalesi [tr]</i>	195-200
MODELING A SOLAR POWER PLANT WITH ARTIFICIAL NEURAL NETWORKS <i>YAPAY SİNİR AĞLARI İLE GÜNEŞ ENERJİSİ SANTRALİNİN MODELLENMESİ</i> <i>Seren Arslan, Hikmet Esen, Engin Avcı, Can Cengiz</i> <i>Research Article [en] Araştırma Makalesi [tr]</i>	201-206
A REVIEW AND EVALUATION STUDY OF MAXIMUM POWER POINT TRACKING TECHNIQUES FOR PV SYSTEMS <i>PV SİSTEMLERDE KULLANILAN MAKSİMUM GÜÇ NOKTASI İZLEME TEKNİKLERİNİN İNCELENMESİ VE DEĞERLENDİRİLMESİ</i> <i>Fuad Alhaj Omar</i> <i>Review Article [en] Derleme Makalesi [tr]</i>	207-230



IMPLEMENT OF LLRNET TO 5G-NR ON LINK-LEVEL SIMULATION

Bircan Çalışır^{*1} 

¹Firat University, Faculty of Engineering, Department of Electrical and Electronical Engineering, Elazığ, Turkey

Abstract

Original scientific paper

Modern receivers apply smooth demodulation and demapping processes to received symbols, using bit log-likelihood ratios (LLRs). Known as "LLRnet" demodulator architecture is offered that is a global educatable neural network attributed in this paper. The calculation of the optimal LLR algorithm includes the calculation of each bit in the LLR value and requires the assessment of whole lattice points as high dimensional which is unpractical for the QAM modulation. Known the most in the literature the Maximum Likelihood (ML) detector shows very high computational complexity that is used in the QAM scheme. Besides LLRnet developed achievement importantly, all calculational complexity is also reduced. Via estimating exact log-likelihood, how to create symbols, and channel corruptions for training a neural network LLRnet is shown in this paper. New and contemporary radio communication systems, such as 5G-NR (New Radio) and DVB (Digital Video Broadcasting) for satellite, DVB (S.2 Second Generation) utilize the LLR approach that calculates soft bit values with FEC (Forward Error Correction) algorithms and utilizes demodulated smooth bit values. This article aims a link-level simulation study to implement of LLRnet to DVB S2 and 5G-NR. The motivation of this study is seen that performing machine learning techniques on physical layer scheme, makes LLRnet a powerful example for practicability. This paper offers to compare Max-Log Approximate LLR, Exact LLR, and LLRnet methods for 16, 32 and 128 QAM.

Keywords: LLR, modulation, radio communication, OFDM.

BAĞLANTI SEVİYESİ SİMÜLASYON ÜZERİNDE LLRNET'İN 5G-NR'YE UYGULANMASI

Özet

Orijinal bilimsel makale

Modern alıcılar, bit log-olasılık oranlarını (LLR'ler) kullanarak alınan sembollere yumuşak demodülasyon ve de-mapping işlemleri uygular. Optimal LLR algoritmasının hesaplanması, LLR değerindeki her bir bitin hesaplanmasını içerir ve QAM modülasyonu için pratik olmayan, tüm kafes noktalarının yüksek boyutlu olarak değerlendirilmesini gerektirir. Literatürde en çok bilinen Maksimum Olabilirlik (ML) dedektörü, QAM şemasında kullanılan çok yüksek hesaplama karmaşıklığı gösterir. Bu makalede atfedilen, küresel bir eğitilebilir sinir ağı olan "LLRnet" demodülatör mimarisi sunulmaktadır. LLRnet başarıyı önemli ölçüde geliştirmesinin yanı sıra, tüm hesaplama karmaşıklığını da azaltır. Bu yazı, bir sinir ağının LLRnet'i eğitmek için tam log-olasılığını tahmin etmesini, sembollerin nasıl oluşturulacağını ve kanal bozulmalarının nasıl olacağını göstermektedir. Uydular için 5G-NR (Yeni Radyo) ve DVB (Dijital Video Yayını), DVB (S.2 İkinci Nesil) gibi yeni ve çağdaş radyo iletişim sistemleri, FEC (İleri Hata Düzeltme) ile yumuşak bit değerlerini hesaplayan algoritmalar ve demodüle edilmiş düzgün bit değerlerini kullanan LLR yaklaşımını kullanır. Bu makale, LLRnet'in DVB S2 ve 5G-NR'ye uygulanması için bağlantı düzeyinde bir simülasyon çalışması sunmaktadır. Bu çalışmada, makine öğrenmesi tekniklerinin fiziksel katman şeması üzerinde gerçekleştirilmesinin LLRnet'i uygulanabilirlik açısından güçlü bir örnek haline getirdiği görülmektedir. Yine bu makale, 16, 32 ve 128 QAM için Max-Log Approximate LLR, Tam LLR ve LLRnet yöntemlerini karşılaştırmayı önerir.

Anahtar Kelimeler: LLR, modülasyon, radyo haberleşmesi, OFDM.

1 Introduction

Demapping symbols on the receiver side back into their original bits is an important stage in any radio communication system. The log-likelihood ratio (LLR) is representatively stated the value of trust on demodulation process of the symbol. The log-MAP makes an exact assessment of the LLR [1], calculating the rate with the

MAP (Maximum A Posteriori) possibilities of two hidden theories of bit. Even though statistically optimum, the dimension of the symbol constellation and the complexity of computation of the log-MAP algorithm scale, and applies directly to real systems. A popular approach to optimum log-MAP, a goal to design convenient systems, is the reputed max-log-MAP algorithm [2]. Generally, the approximated max log-MAP method eliminates the

*Corresponding author.

E-mail address: bkamislioglu@firat.edu.tr (B. Çalışır)

Received 04 August 2022; Received in revised form 12 June 2023; Accepted 17 July 2023

2587-1943 | © 2023 IJIEA. All rights reserved.

Doi: <https://doi.org/10.46460/ijiea.1155627>

requirement of calculating complex exponential and logarithmic functions but expends a large number of processes that scale according to the modulation order.

In quadrature amplitude modulation (QAM) structure, the maxlog-MAP got below to a decreased complication of linear function and could be so applied using a lookup table (LUT). This means the natural constellation mapping symmetries of QAM and, the QAM can separate into two free PAM (Pulse Amplitude Modulations) in the imaginary and real components on the signal [3-6].

Deep learning has recently found its place in many applications and has achieved successful results. Deep learning (DL) is used for signal detection of OFDM-IM (orthogonal frequency division multiplexing with index modulation) systems [7]. A new deep learning (DL) aided receiver is developed for NOMA joint signal detection in [8]. DL is utilized here as receiver and used for channel estimation, equalization, and demodulation aims. In [9], a new deep learning based application is used for joint channel estimation and signal detection in OFDM systems. Channel Estimation Network (CENet) is specifically method designed to relay the conventional interpolation procedure in estimation layout.

In this work, we proposed a named "LLRnet" method that is an efficient machine-learning structure for universal smooth demodulation. While the demapping process is briefed as symbol to bit LLRs work, just, neural network is seen as an excellent method that approximates functions effectively. Obtained results from simulations show the LLRnet succeeds in achieving excellently the target demodulation performance. LLRnet is reduced seriously computational burden and reproduces the exact log-MAP algorithm for QAM constellations.

This paper is planned in this order. Section II describes The LLR estimation problem. The proposed LLRnet architecture is introduced in Section III. Results of simulation of the performance of LLRnet in the case of some work implementations such as the cellular 5G and the satellite DVBS.2 standards are given in Section IV, finally, a few deducing notes are contained in Section V.

1.1 Problem Modelling

In this section, link-level simulation study to implement of LLRnet to 5G-NR will realize for the remainder of this paper explored.

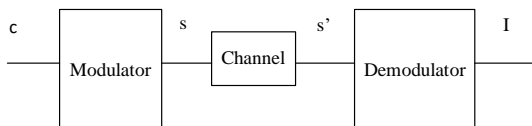


Figure 1. A communication system.

A basic radio communication technology as illustrated in Figure 1 comprises a modulator, composite channel and demodulator. Coded bits that are given in Figure 1 pointed out by $c \in \{0,1\}$ and sequence of modulated symbols are shown by $s = \{s_1, \dots, s_N\} T \in C, C \subset CN, N \in Z > 0$. As a result $c = \{c_1, \dots, c_M\} T \in \{0,1\}M$, is admitted to being some arbitrary M vector of successive bits in the stream is modulated to a complicated symbol s by N-dimensional

[10, 11]. The symbol transmitting includes a composite channel, the physical channel additionally, and an abstraction of other crucial transceiver operation steps Pre-code process to transmit over MIMO (Multiple Input Multiple Output) techniques on the transmitter part, mapping for OFDM (Orthogonal Frequency- Division Multiplexing), and DAC (Digital Analog Conversion) for analog radio carriers are created by the composite channel. ADC (Analog Digital Conversion), mix down to base band, synchronization, filtering, demodulation of OFDM, MIMO demodulation, and estimation and equalization of the channel are realized on the receiver part, by the composite channel. The mentioned steps are standard for transceiver processing and are not related to the demapping, or smooth demodulation of the transceiver signal to bit LLRs particularly. On the receiver side, the demodulator traces the complex-valued symbol estimate of the compound channel, $s^{\wedge} \in CN$, and the impact of the compound channel is defined by the correlation among the transmitting and tracing signals s, and s^{\wedge} by turns. Though not certain, the compound channel is representatively shaped as an AWGN (Adding White Gauss Noises) given n for the intention of smooth demodulation to bit LLRs as seen Equation 1 [12].

$$s' = s + n \tag{1}$$

On the demodulator sides, we demap the traced signal, s^{\wedge} , in a vector of prediction of the M-bit LLRs, $l \in RM$, based on reliance on the conclusion of each of the inventive coded bits to facilitate advanced decoding in the following stage.

LLRs vector for the i'th entry, l_i , based on the logarithm of the MAP relation given in Equation 2 [12] On the receiver side, $C_i^{\delta} \in C$ i'th bit is equal to $\delta \in \{0, 1\}$ and corresponds to the subseries of constellation dots.

$$l_i = \log \left(\frac{P_r(c_i=0,s')}{P_r(c_i=1,s')} \right) \quad i = 1, \dots, M \tag{2}$$

A certain calculation of the log-MAP statement, in the investigated model output is given in Equation 3 [12]. In Equation 3, σ^2 is defined as noise variance.

$$l_i = \log \frac{\sum_{s \in C_i^0} \exp(-\frac{\|s' - s\|_2^2}{\sigma^2})}{\sum_{s \in C_i^1} \exp(-\frac{\|s' - s\|_2^2}{\sigma^2})} \quad i = 1, \dots, M \tag{3}$$

Approximated LLR estimates remove from a facilitated formula, known to all as the max-log-MAP on the exact log-MAP process as seen in Equation 4 [12].

$$l_i = \frac{1}{\sigma^2} (\min_{s \in C_i^1} \|s' - s\|_2^2 - \min_{s \in C_i^0} \|s' - s\|_2^2) \tag{4}$$

The advantageous feature of the approximated max-log-MAP de-mapping law is that eliminates the requirement for calculating functions of complex exponential and logarithmic. For QAM constellations, while to be violently sub optimal the max-log-MAP is a characteristically the widespread de-mapper because of degraded to a sole LUT application of part-wise linear functions, which is measured SNR linearly [9-12].

2 OFDM Modulation

Quadrature amplitude modulation (QAM) is a developed modulation layout broadly utilized in radio communication technologies that consubstantiate amplitude modulation and phase modulation. In digital signal modulation, QAM obtains a higher rate than widespread amplitude and phase modulation, which promote just two kinds of symbols to separate 0 and 1. In amplitude modulation, 0 and 1 are separated by replacing the amplitude of carrier and in phase modulation, 0 and 1 are separated by replacing the phase of carrier. For example in QPSK, 2 bits per symbol (00, 01, 10, or 11) can be encoded through the following four phases: 0°, 90°, 180°, and 270°. In other hand QPSK is admitted as a particular sort of QAM, that is 4-QAM. In QAM, signals are loaded to two orthogonal carriers (representatively sin and cos), the carriers' amplitudes are adjusted, and added their amplitudes to create the signals modulated by both the phase and amplitude. The carriers are generally defined as I and Q signals. So, the mentioned modulation method is also described as I-Q modulation.

OFDM is described as a multi carrier digital modulation plan that broadens single subcarrier modulation by utilizing multiple subcarriers within the identical channel. OFDM uses a big number of orthogonal subcarriers which transmitted in parallel rather than provide a high rate sequence of data using one subcarrier. Traditional digital modulation schemes (such as QPSK, 16QAM, etc.) modulate each subcarrier with a at low symbol rate. However, the compound of many subcarriers lets resemblance data rates to traditional one carrier modulation layouts within equal bandwidths [3].

OFDM produces Q (Quadrature) and I (In-phase) elements of $c_n(m)$ in complex domain utilizing data bits. M length an IFFT (Inverse Fast Fourier Transform) applies and M complex data block is created in the time area. In the IFFT input, zero adds to unused sub-carriers. Relation of input and output of OFDM base band modulation scheme is noted in the discrete time area as given in Equation 5 [12].

$$s_n(k) = \sum_{m=0}^{(M-1)} c_n(m)e^{(j2\pi mk/M)} \tag{5}$$

In Equation 5, M expresses the number of subcarriers, and the data symbols with complex values ensured from a QAM constellation are indicated by $c_n(m)$. Taking into account that m is the subcarrier index and n is block index, $s(k)$ shows the complex valued output of data symbols of OFDM modulation process.

3 Smooth Demodulation With LLRNET

A neural network named as LLRnet in order to learn a desired smooth demodulation layout is purposed to demap a symbol by valued complexity to this reel valuable LLRs of transmitted bits.

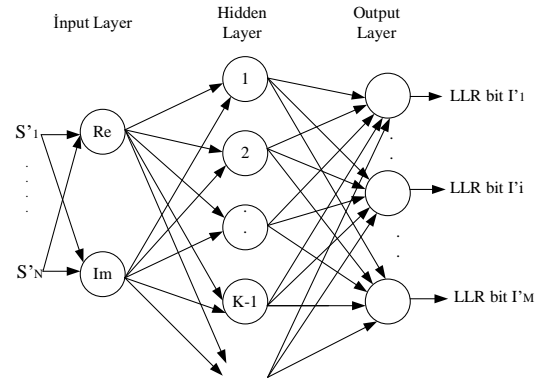


Figure 2. LLRnet structure [8].

The structure of LLRnet is depicted in Figure 2 and from figure, the received symbol prediction vector, \hat{s} , feeds the entrance of the LLRnet. LLRnet injects the output vectors of the two input loops into a secret bit sheet of K neurons.

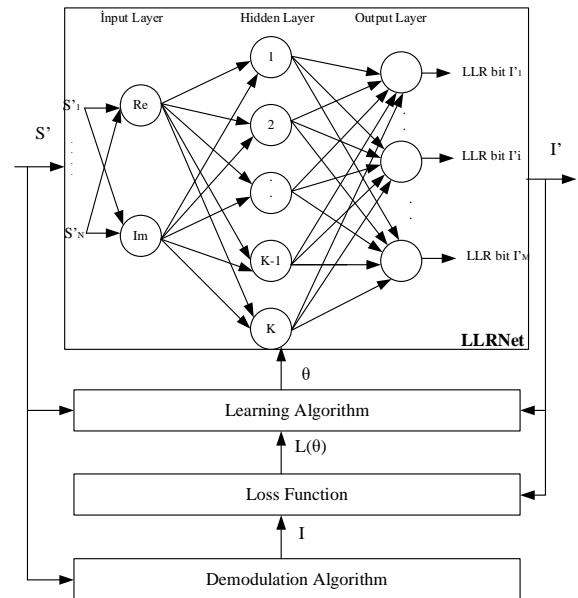


Figure 3. Training diagram of LLRnet structure [8].

The training diagram of the neural network demodulator is shown in Figure 3 schematically. Because the input-to-output function of the LLRnet fully consists of the setting of overall training coefficients, θ , as a training process, a gradient-based approximation could accept. The identical bit LLRs are calculated using a desired demapping algorithm for a specific batch of receipt signals $B, \hat{s}^b(b), b = 1, \dots, B$. Then both the traditionally calculated LLRs, $l(b)$, and the LLRs calculated via LLRnet, $I^b(b)$ feed a lost of function that is clearly described as a trained coefficients sequence function of the θ . Loss function can be defined as Equation 6 [12].

$$L^{MSE}(\theta) = \frac{1}{B} \sum_{b=1}^B \|I^b(b) - l(b)\|_2^2 \tag{6}$$

An arrest criterion is defined which can be either a constant count of repetitions, a sill value for the loss, or a count of repetitions with no reduced loss. The parameter set, θ is updated up to the stop criterion is satisfied. As the arrest criterion is satisfied and training is finished, the

LLRnet is admitted as the only demodulator, productively copying the functionality of the demanded smooth demodulator [13, 15].

The performance criteria of the defined network are mean square error (MSE). The performance criteria of the defined network are mean square error (MSE). The obtained last MSE worths from simulations explain the used neural network converging to an MSE worth that is at least 40 dB less than the mean square exact LLR worths given in Table 1.

Table 1. SNR and MSE relation.

SNR	MS _{LLR}	MSE _{last}
-5	4.43	6.80e-5
0	15.74	9.05e-5
5	60.01	8.50e-3

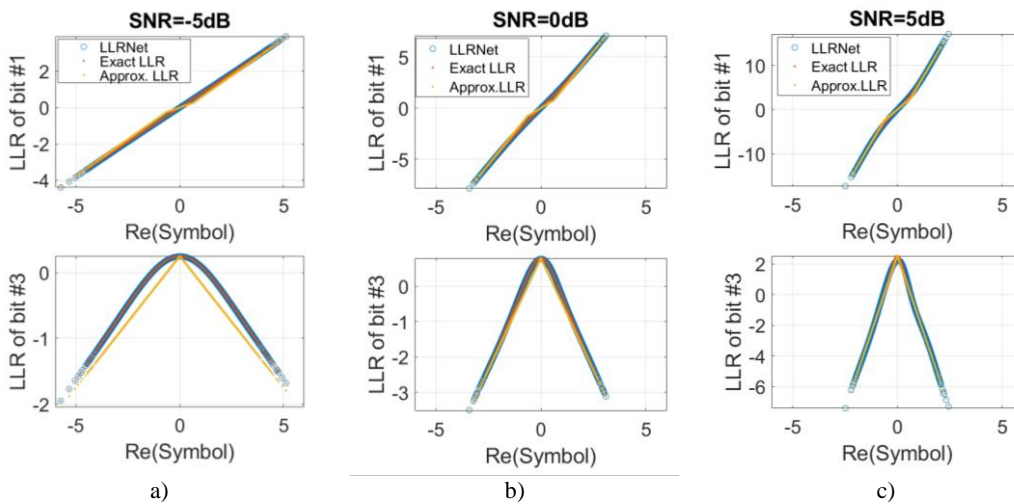


Figure 4. LLR comparison for 16-QAM (a for -5dB SNR, b for 0dB SNR, c for 5dB SNR).

LLR comparison of LLRNet, exact LLR and approximation LLR for 16-QAM (a for -5dB SNR, b for 0dB SNR, c for 5dB SNR) is illustrated in Figure 4. Simulations are realized for 1 bit and 3 bit for each SNR values. In Figure 5, LLR comparison of LLRNet, exact LLR and approximation LLR for 32-QAM (a for 0 dB SNR, b for 5 dB SNR, c for 10 dB SNR) is shown and

4 Simulation Examples

The proposed in this work LLRnet demodulation method is used in both PDSCH (Physically Down link Share Channel) with utilizing 5G-NR link and the 3GPP standard. QAM modulation is one of the modulation methods utilized for 5G NR. In this section correctness guess of LLRNet on the LLR worths for 16, 32, and 128 QAM modulation is explored. Considering an M-QAM modulation method that has AWGN channel circumstance, this approximation fits both the channel has frequency selective property and symbols are equalized. The consequent figures show computed LLR worths for the mentioned three algorithms.

simulations are applied for 1 bit, 3 bit and 5 bit for each SNR values. As seen in Figure 6, LLR comparison of LLRNet, exact LLR and approximation LLR for 128-QAM (a for 0 dB SNR, b for 10 dB SNR, c for 20 dB SNR) is obtained and applications are simulated for 1 bit, 3 bit and 5 bit for each SNR values

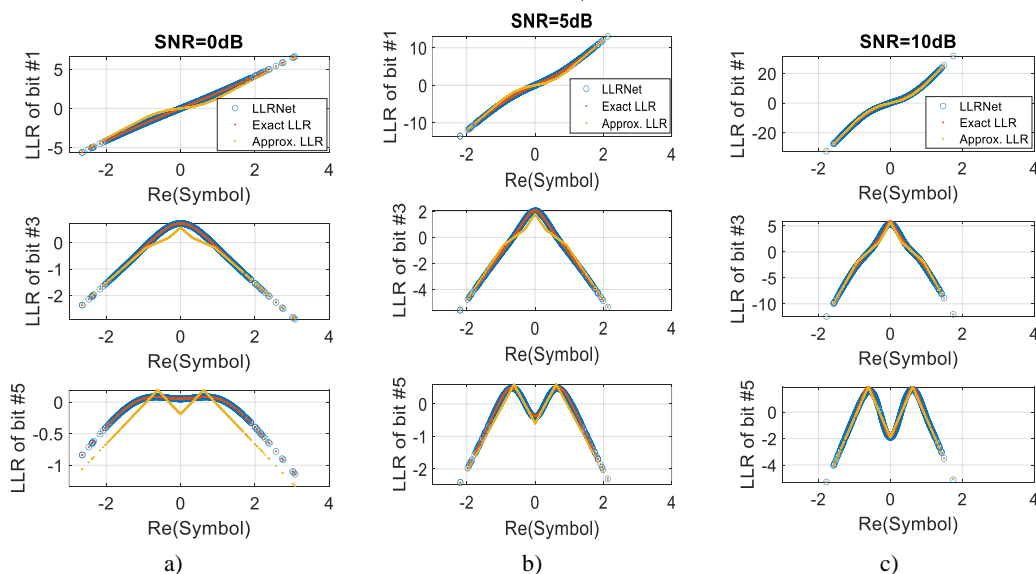


Figure 5. LLR comparison for 32-QAM (a for 0 dB SNR, b for 5 dB SNR, c for 10 dB SNR).

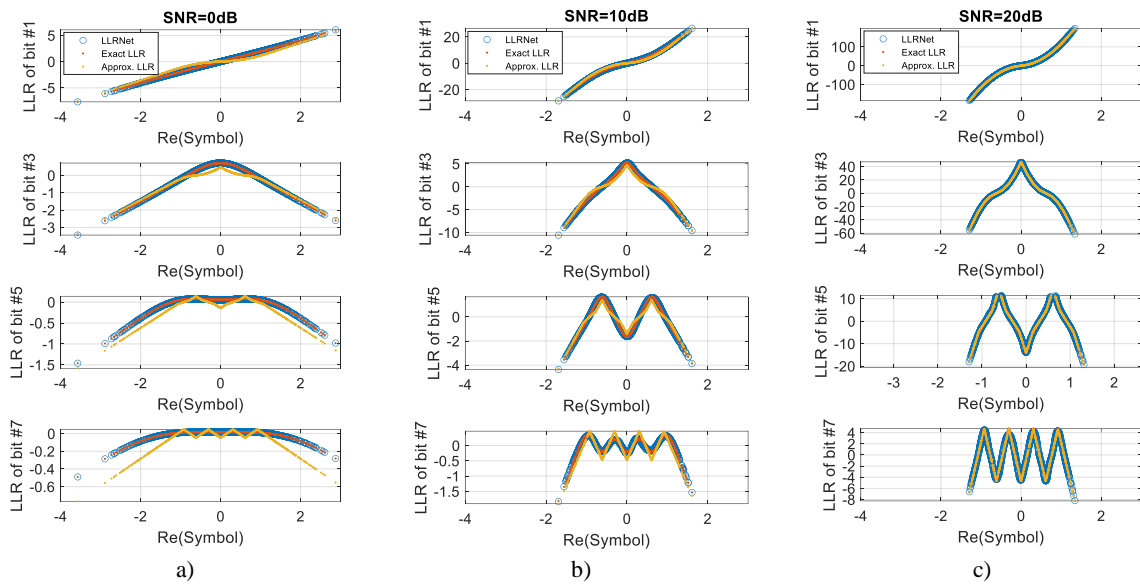


Figure 6. LLR comparison for 128-QAM (a for 0 dB SNR, b for 10dB SNR, c for 20dB SNR).

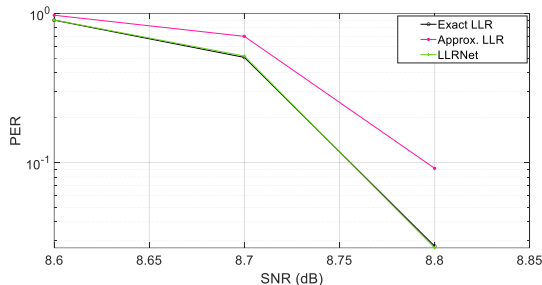


Figure 7. PER to Es/N₀ for exact LLR, approximation LLR and LLRNet.

This paper presents an application of exact LLR, approximation LLR and LLRNet neural network methods that are applicable and work well fairly to apply QAM modulation for different orders. Considering Figure 4, Figure 5 and Figure 6, in the higher SNR values (c), the exact LLR shows a fine prediction of the optimal approximation LLR rule for the analyzed three different orders of QAM modulations. However, (b) the exact LLR only works as a rough for low SNR, and fair for mid SNR to the full demapper in the low and mid SNR values. As the last, the smooth bits obtained by the LLRnet practically trace the optimum bits for all three QAM modulation cases in all SNR values [10]. In Figure 7, PER to Es/N₀ for exact LLR, approximation LLR and LLRNet are obtained for 100 number of frames. Exact LLR and LLRNet shows similar behavior but approximation LLR shows different behavior considering PER-SNR.

5 Conclusion

This paper presents a machine learning approximation which an easy neural network structure. This structure is trained to smooth demodulated symbols productively to bit LLRs. So, an AI (Artificial Intelligence) algorithm converts into the most general construction units of the operation of the physical case. LLRnet, which suggested opinion of this work, can be both expanded to deep learning structures with multi layers and be combined with a trainable receiver model. In addition, the comparison of exact LLR, approximation

LLR and LLRNet is presented about LLR bits correspond to real symbols and PER to Es/N₀. This application is illustrated effective performance of LLRNet cases in all SNR values.

Declaration

Ethics committee approval document is not required for this study.

References

- [1] Erfanian, J., Pasupathy, S., & Gulak, G. (1994). Reduced complexity symbol detectors with parallel structure for ISI channels. *IEEE Transactions on Communications*, 42(234) 1661–1671.
- [2] Robertson, P., Villebrun, E., & Hoeher, P. (1995, June). A comparison of optimal and sub-optimal MAP decoding algorithms operating in the log domain. *Proceedings IEEE International Conference on Communications ICC 95*, (pp. 1009–1013).
- [3] Tosato, F., & Bisaglia, P. (2002, April). Simplified soft-output demapper for binary interleaved COFDM with application to HIPERLAN/2. *IEEE International Conference on Communications. Conference Proceedings. ICC 2002 (Cat. No.02CH37333)*, (vol. 2, pp. 664–668).
- [4] Wang, Q., Xie, Q., Wang, Z., Chen, S., & Hanzo, L. (2014). A universal low-complexity symbol-to-bit soft demapper. *IEEE Transactions on Vehicular Technology*, 63(1), 119–130.
- [5] Cybenko, G. (1989). Approximation by superpositions of a sigmoidal function. *Mathematics of control, signals and systems*, 2 (4), 303–314.
- [6] Yao, Y., Su, Y., Shi, J., & Lin, J. (2015, August). A low-complexity soft QAM demapper based on first-order linear approximation. *2015 IEEE 26th Annual International Symposium on Personal, Indoor, and Mobile Radio Communications (PIMRC)*, (pp. 446–450).
- [7] Luong, T.V., Ko, Y., Vien, N. A., Nguyen D. H. N., & Matthaiou, M. (2019). Deep Learning-Based Detector for OFDM-IM. *IEEE Wireless Communications Letters*, 8(4).
- [8] Xie, Y., The, K.C., & Kot, A. C. (2021). Deep Learning-Based Joint Detection for OFDM-NOMA Scheme. *IEEE Communications Letters*, 25(8).

- [9] Yi, X., & Zhong, C. (2020). Deep Learning for Joint Channel Estimation and Signal Detection in OFDM Systems. *IEEE Communications Letters*, 24(12).
- [10] Hagan, M. T., & Menhaj, M. B. (1994). Training feedforward networks with the Marquardt algorithm. *IEEE Transactions on Neural Networks*, 5(6), 989–993.
- [11] Shental, O., & Hoydis, J. (2019, December). Machine LLRning": Learning to Softly Demodulate. *2019 IEEE Globecom Workshops (GC Wkshps)*.
- [12] Hu, Z., Chen, F., Wen, M., Ji, F., & Yu H. (2018). Low-Complexity LLR Calculation for OFDM with Index Modulation. *IEEE Wireless Communications Letters*, Vol. 7, No. 4.
- [13] Sabud, S., & Kumar, P. (2022). A Low Complexity Two-Stage LLR Detector for Downlink OFDM-IM NOMA. *IEEE Communications Letters*, Vol. 26, No. 10.
- [14] Espluga, L. O., Aubault-Roudier, M., Poulliat, C. Boucheret, M. L., Al-Bitar, H., & Closas, P. (2020). LLR Approximation for Fading Channels Using a Bayesian Approach. *IEEE Communications Letters*, Vol. 24, No. 6.
- [15] Pang, P., Chang, H., Zhang, Q., Xin, X., Gao, R., Tian, F., Tian, Q., Wang, Y., & Guo, D. (2021). The research of probabilistic shaping signal transmission scheme based on neural network LLR calculation. *2021 19th International Conference on Optical Communications and Networks (ICOON)*.



GENETIC ALGORITHM BASED APPROACH FOR ALGORITHMIC TRADING IN FINANCIAL MARKETS

Yunus Santur^{*1}, Mustafa Ulas², Murat Karabatak¹

¹Firat University, Faculty of Technology, Department of Software Engineering, Elazig, Turkey

²Firat University, Faculty of Engineering, Department of Software Engineering, Elazig, Turkey

Abstract

Original scientific paper

Software that enables realtime buy and sell transactions in financial markets according to predetermined conditions is called algorithmic trading. When developing algorithmic trading robots, indicators used in technical analysis are generally used. For the strategy selection of the robot, a process called Backtest is performed on the historical time series. The purpose of the Backtest process is the process of obtaining and interpreting values such as the number of successful/unsuccessful trades, the portfolio cash value after the commission to be paid to the intermediary institution, the profit factor and the sharpe ratio. The biggest disadvantage in this process is the selection of the appropriate stock, period, indicator and their parameters. Linear programming approaches are mostly used in the selection of these parameters that optimize the Backtest process optimally. However, according to the strategy to be used, the coding of these algorithms can have a linear, quadratic or polynomial complexity. This requires more long testing times for investors and algorithmic robot developers. Genetic algorithm-based approaches inspired by nature, on the other hand, converge to the optimal solution with much less iteration and require less processing power and time. In this study, a genetic programming-based approach is proposed for the selection of optimal conditions in algorithmic trading. In the experimental studies section, it has been seen that the use of traditional and genetic algorithm-based approaches in algorithmic trading operations has advantages when comparing complexity.

Keywords: Algorithmic trading, genetic algorithm, optimization.

FİNANSAL PİYASALARDA ALGORİTMİK TİCARET İÇİN GENETİK ALGORİTMA TEMELİ YAKLAŞIM

Özet

Orijinal bilimsel makale

Finansal piyasalarda önceden belirlenmiş koşullara göre anlık al sat işlemlerinin yapılmasını sağlayan yazılımlara algoritmik ticaret denilmektedir. Algoritmik işlem robotları geliştirilirken genellikle teknik analizde kullanılan göstergeler kullanılmaktadır. Robotun strateji seçimi için geçmiş veriler üzerinde Backtest adı verilen işlem gerçekleştirilmektedir. Backtest işleminin amacı gerçekleştirilen başarılı/başarısız ticaret sayısı, aracı kuruma ödenecek komisyon sonrası portföy kasa değeri, kar faktörü ve sharpe oranı gibi değerlerin elde edilerek yorumlanması işlemidir. Bu süreçte en büyük dezavantaj uygun stok, periyot, indikatör ve bunlara ait parametrelerin seçimidir. Backtest işlemini optimal olarak en iyileyen bu parametrelerin seçiminde çoğunlukla doğrusal programlama yaklaşımları kullanılmaktadır. Ancak kullanılacak stratejiye göre bu algoritmaların kodlanması lineer bir karmaşıklıktan, quadratic veya polynomial karmaşıklığa sahip olabilmektedir. Bu durum yatırımcılar ve algoritmik robot geliştiriciler için uzun test süreleri gerektirmektedir. Doğadan esinlenerek geliştirilen genetik algoritma tabanlı yaklaşımlar ise çok daha az iterasyon ile optimal çözüme yakınsayarak, daha az işlem gücü ve zaman gerektirmektedir. Bu çalışmada algoritmik ticarete optimal koşulların seçimi için genetik programlama tabanlı bir yaklaşım önerilmiştir. Deneysel çalışmalar bölümünde, geleneksel ve genetik algoritma tabanlı yaklaşımların karmaşıklık, benchmark ve Backtest sonuçları karşılaştırıldığında algoritmik ticaret işlemlerinde kullanılmasının avantajlara sahip olduğu görülmüştür.

Keywords: Algoritmik ticaret, genetik programlama, optimizasyon.

1 Introduction

Transactions in stocks, crypto-assets and futures markets are handled in two classes as manual and robotic. Manual transactions include dividend investing, long-term

investment, short and long-term investments in line with company/sector expectations. It is known that mostly manual operations are performed around the world. However, it is known that the number of investors making algorithmic transactions has increased in recent years. A

*Corresponding author.

E-mail address: ysantur@firat.edu.tr (Y. Santur)

Received 18 September 2022; Received in revised form 14 May 2023; Accepted 28 August 2023

2587-1943 | © 2023 IJIEA. All rights reserved.

Doi: <https://doi.org/10.46460/ijiea.1176888>

significant size of the transaction volume in financial markets is performed by algorithmic robots. Unlike manual operations, algorithmic operations are performed automatically by software that reads news/text and/or uses technical analysis indicators on temporal series [1-5].



Figure 1. Financial time series data a) OHLC notation in financial time series b) Financial time series and volume.

$$candle = \begin{cases} \text{Bullish, if } Close > Open \\ \text{Bearish, otherwise} \end{cases} \quad (1)$$

It is known that there are hundreds of indicators that have entered the literature in technical analysis and have been developed as open or close sourced.

These indicators are obtained by using the open, close, low, high and transaction volume information of the financial asset within the relevant period. In the Figure 1, the time series of the financial asset is shown by using the Volume amount as a bar chart in the lower part of the price chart, and the candle charts consolidating the O:Open, C:Close, L:Low and H:High price values in a single visual at the top. While creating candlestick charts, a single image can be obtained from the OHLC data, which are the four values mentioned [6].

Eq.(1) is used when naming candlestick charts. Although they express Bullish or Bearish in the simplest terms, pattern recognition and the development of pattern-based approaches in the literature is a separate study. Because it is known that there are more than 100 candle patterns. Dozens of different patterns are formed by the ratio of body and shadows, and the combination of these patterns in pairs and triples [7].

In Figure 2, the most known and widely used indicators obtained from time series are given. The formulas for these and the Buy/Sell strategies that can be created are given in Table 1. The indicators in Table 1 are expressed as : Simple moving average (SMA), Exponential Moving Average (EMA), Moving Average Convergence/Divergence (MACD), Relative Strength Index (RSI) and Momentum (Mom), respectively [8] .

The SMA given in Eq.(2) represents the moving average of the selected n periods. It is assumed, above the selected period trend is bullish, below the selected period trend is bearish. In the equation, C represents the closing values, but any of the OHLC can be chosen according to the strategy.

Table 1. Commonly used indicators and trading strategies.

Indicator	formula	Strategy	Eq.
SMA	$SMA = \sum C_i/n$	<ul style="list-style-type: none"> The price cuts the average up The shorter of the averages of two different periods cuts the longer one up. 	(2)
EMA	$EMA_t = \begin{cases} C_0, & \text{if } t = 0 \\ \alpha + (1 - \alpha)EMA_{t-1}, & \text{if } t > 0 \end{cases}$		(3)
MACD	$MACD_{line} = EMA(12) - EMA(26)$ $Signal_{line} = EMA(MACD_{line}, 9)$	<ul style="list-style-type: none"> MACD value cuts up Signal value 	(4)
RSI	$RSI = 100 - \frac{100}{1 + \mu_{Gain}/\mu_{Loss}}$	<ul style="list-style-type: none"> Intersection of RSI value with 30/70 threshold values RSI value cutting its average up 	(5)
mom	$MOM = 100 * \frac{C_i}{C_{i-n}}$	<ul style="list-style-type: none"> The intersection of the MOM value with the threshold value 	(6)

The EMA given in Eq. (3), unlike the SMA, does not weight the bars equally, it is calculated recursively according to the values of the previous bars. Thus, it is more sensitive to recent price movements. The MACD given in Eq. (4) was used for the Japanese markets in the early years. It takes the difference of the EMA value in two different periods, which is also used in the SMA and EMA

strategy, while Signal provides the smoothing value in the default 9 periods. Since the Japanese markets are open six days a week, the strategy is formed by calculating the difference of the 2-week buying momentum (12) to the one-month buying momentum (26) and its intersection with its 9-day softened value. Although the default period

is calculated based on daily values, different periods can be selected.

The RSI given in Eq.(5) is a common indicator used for excess, normalized to the 0-100 range. Below 30 means oversold and over 70 means overbought. As a general acceptance, a position is taken assuming that if it goes above 30 again, it is bullish, and if it goes below 70 when it is above 70, it will be a bearish trend.

Another strategy is to use the intersection of the RSI value with its average according to the n periods to be selected, as a common option. The Mom given in Eq. (6) represents the percentage change according to the selected n periods. The main motivation of the strategy used in the Mom indicator is to avoid horizontal market noise.

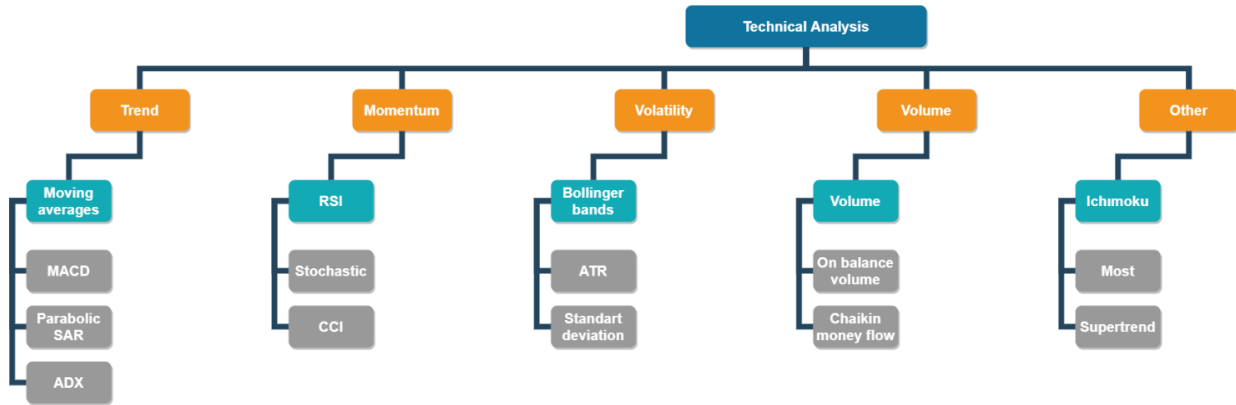


Figure 2. Technical analysis indicators.

2 Materials and Methods

In this study, a genetic algorithm-based approach is proposed for the parameter selection of indicators, periods and indicators in the algorithmic robot development process. The data terminals used in this area handle the parameter selection optimization process with linear programming by using time series data in the backtest process. For example, the MACD indicator takes 3 parameter data as input. Considering the selection of periods such as day, 4-hour, hourly, combining with other indicators and stock selection, optimizing with nested loops has quadratic or polynomial complexity. This situation causes a disadvantage in the selection of hundreds of stocks, the period to be selected, the indicator to be used and the periods of the indicators. Genetic algorithms inspired by nature offer a much more effective solution to the optimization problem. In the continuation of the article, information about the data set and the proposed approach, data and experimental studies are presented.

2.1 Dataset

In the study, data sets of financial assets given in Table.2 were obtained from Yahoo finance platform and used [9].

Table 2. Commonly used indicators and trading strategies.

Data set	Explanation	Date range
Bist100	Borsa Istanbul national 100 index	27.08.2020 22.08.2022

Yahoo finance platform provides OHLCV (OHLC + V:Volume) data for almost all financial assets in the desired period and date range free of charge in .csv format. The screenshot obtained from the raw data set in the application environment is shown in Figure 3.

Date	Open	High	Low	Close	Volume
2022-03-25	2171.5073	2187.1497	2165.6291	2175.5000	2.113966e+09
2022-04-15	2513.7488	2536.2945	2510.1943	2494.3999	3.444524e+09
2022-04-20	2525.8999	2536.5000	2502.3999	2525.8999	4.118388e+09
2020-12-04	1330.2004	1336.4939	1324.8061	1330.0000	5.295296e+09
2022-06-29	2314.6930	2316.2716	2230.5594	2402.0000	2.696174e+09

Figure 3. Dataset screenshot.

2.2 Backtest Optimization.

Stock, period and the code structure of the traditional approach used in data terminals for parameter selection of indicators is given in Figure 4. In this approach, nested iterations are performed for the selected range as much as the total number of parameters.

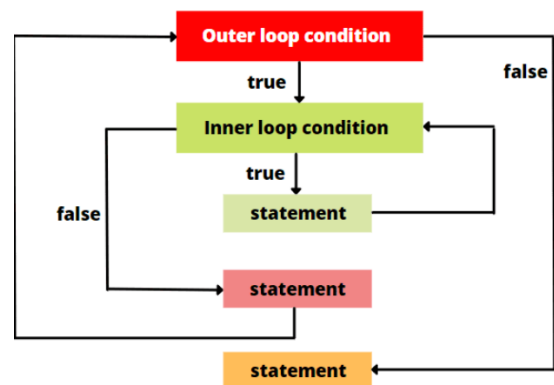


Figure 4. Optimizing with nested loops.

This approach increases the Big-O complexity exponentially according to the number of parameters to be selected [10]. Although this complexity increases, since almost all of the transactions performed are simple conventional (statistical) calculations, the processing computations required is mostly simple. However, the main problem here is the occurrence of overfitting as a result of optimization. Financial time series are chaotic and cannot be expected to fluctuate in the same way in the future. Therefore, it cannot be guaranteed that the values that provide the best optimization will yield good returns

in the future. For this reason, the optimization phase is also supported by Walk Forward Analysis (WFA) or Monte Carlo simulation (MCS). All these are the main disadvantages of traditional Backtest optimization [11, 12].

2.3 Genetic Algorithm Based Backtest Parameter Selector

Genetic algorithms are approaches that are developed by observing nature and realize the optimization with an evolutionary mechanism [13-15]. Genetic algorithms are suitable for Backtest optimization by their nature. It is an effective method that can provide convergence to the most

optimal parameters without the need for process complexity and later approaches such as WFA, MCS and without overfitting.

The proposed approach in this study is given in Figure 5. The approach, which takes the time series as input, makes the parameter selections that optimize the loss function of the network for the selected indicators adaptive. The proposed method can be considered recursively, as well as selecting the most appropriate parameter, combining the most appropriate input value (Open, Close, Low, High) values, the most appropriate period (daily, hourly, weekly) and the most compatible indicators.

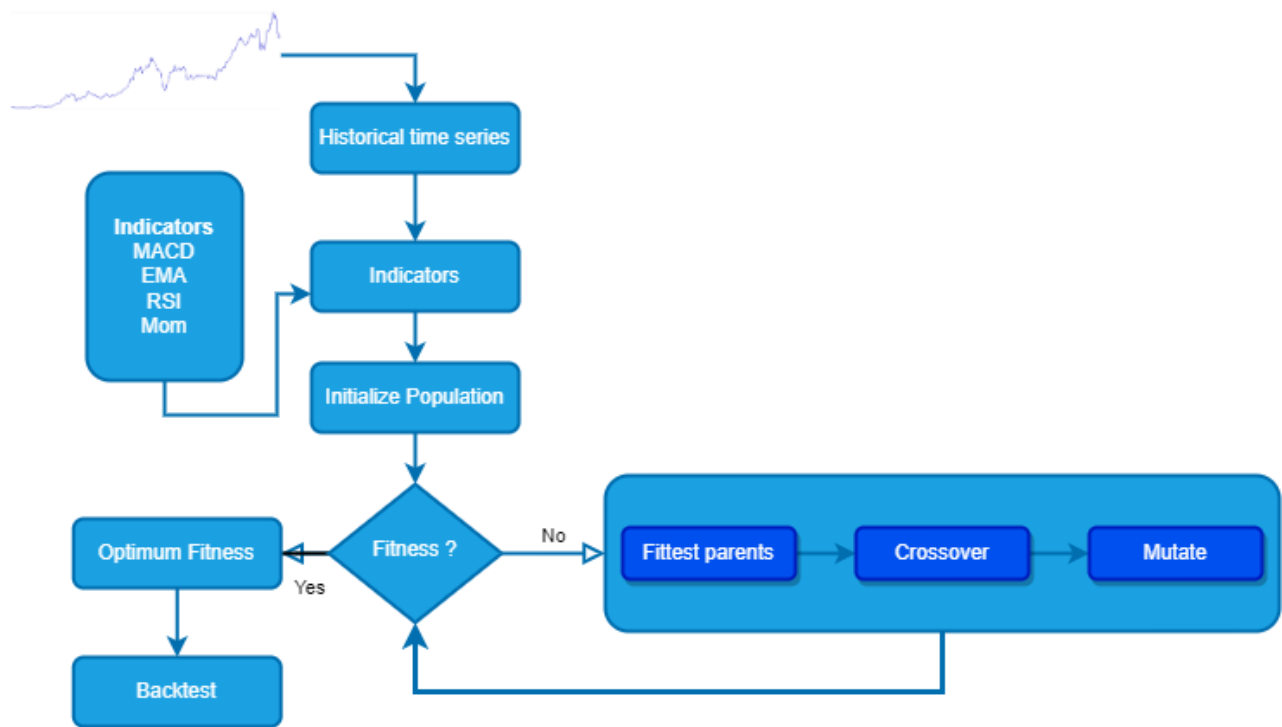


Figure 5. Proposed method.

3 Experiments and Results

Experimental studies consist of 500 pieces of data consisting of daily closing values of approximately 2 years in the Bist100 index. Backtest procedure was used to compare the results [16, 17]. Experimental studies were carried out using Python programming language and pandas, backtrader libraries [18-20]. In the backtest process, slippage and commission are taken into account as (1/10000). In all studies, the initial safe value was assumed to be 10,000. Buy/sell signals obtained at bar closings are shown in Figure 6.



Figure 6. Buy/sell signals.

In the aggregated results given in Table 2, better results were obtained with genetic algorithms for all

indicators. With the proposed approach, it was observed that the portfolio value increased by 28%. Another finding is that the MACD, EMA and RSI indicators work better. When the proposed approach and conventional-based approaches are compared, the portfolio returns increased between 2% and 30% thanks to the proposed approach.

All strategies are designed in two ways. In other words, when the Long signal occurs, if there is a Short position, it buys by taking profit or by closing it with a stop loss, and on the contrary, it closes the Long positions and takes a Short position. For this purpose, positions are opened twice as much as the previous one each time. In the executed Backtest strategy, it can be assumed that 1 lot is purchased at a time or that a cumulative purchase is made at the ratio of the portfolio. In this study, the second one, the cumulative portfolio, was preferred. Better results are shown as bold in Table 2.

In Figure 7 below, the trades and portfolio gains obtained with the conventional and proposed approach for MACD, EMA and RSI in conventional Table 3 from the backtester library are shown collectively.

Table 3. Experimental studies.

Indicator	Conventional Approach		Recommended approach		Strategy
	Default parameters	Portfolio return (%)	Obtained parameters	Portfolio return (%)	
MACD	12 - 26 - 9	-1.9%	3-41-2	28%	Long trade when MACD crosses above signal line up
C - EMA	1 - 8	16%	3-34	18%	Long trade when close cross above 8-ema
EMA	5 - 22	6%	3-34	18%	Long trade when the fastest EMA crosses above slowest EMA
RSI	5 - 14	13%	7 - 14	19%	Long trade when RSI recursively cross above its moving average up
Mom	1.0	15%	.94	17%	Long trade when Mom exceeds percentile

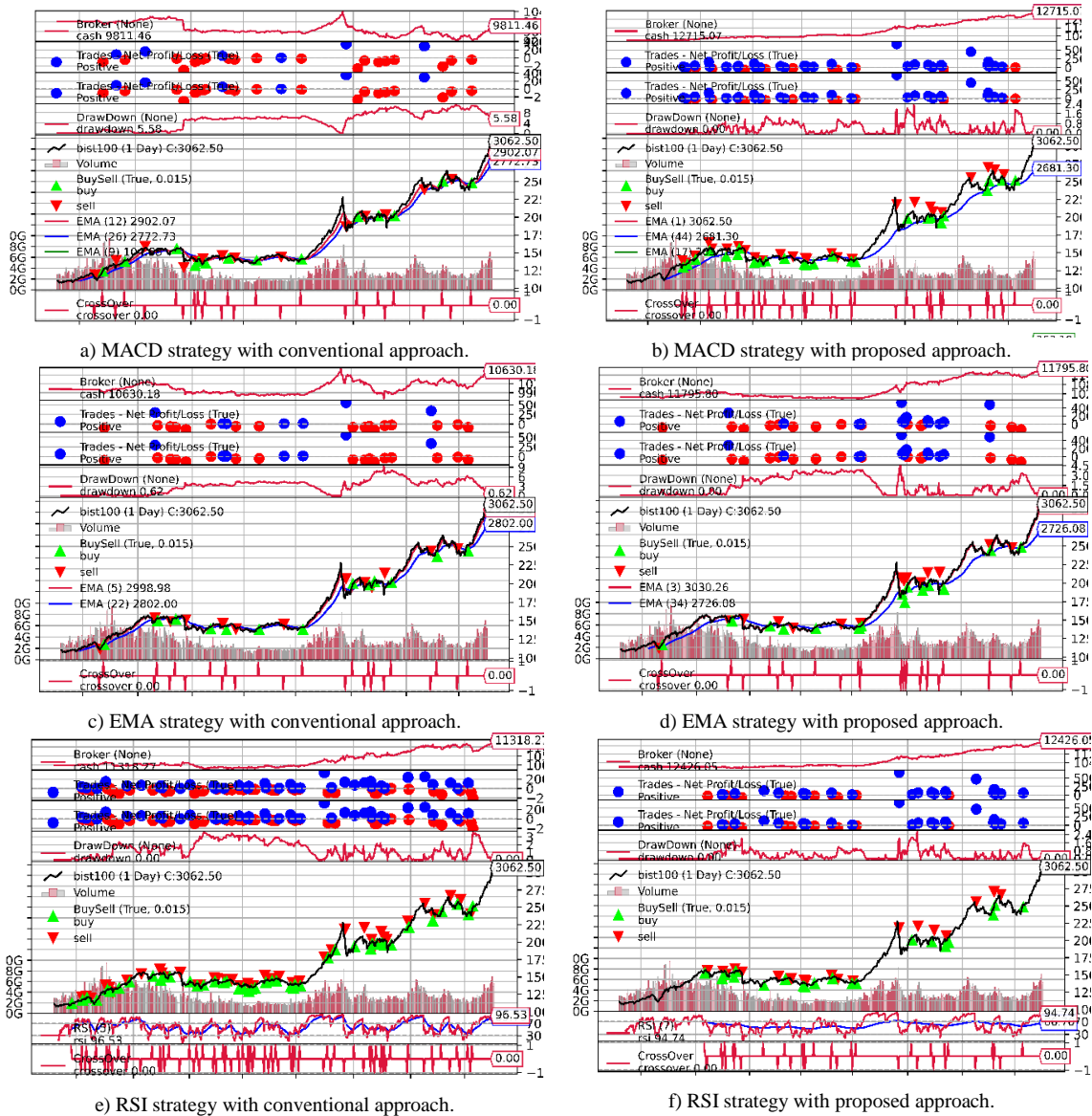


Figure 7. Backtest results

In Figure 8, the average and optimum suitability values typically obtained in experimental studies are shown graphically. When nested loops are used in the optimization process based on the backtest process, much more iterations work. Genetic algorithms, on the other hand, are very suitable for this problem by their nature, they can converge to the optimum solution by exploring the problem space with much less iteration.

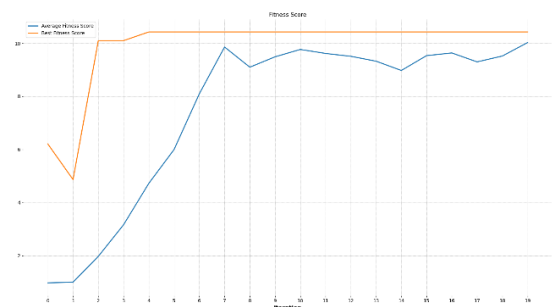


Figure 8. Average and best fitness functions.

4 Conclusions

In this study, an approach is proposed to perform optimization of backtest that based on indicators commonly used in technical analysis, on genetic algorithm. The parameters of the indicators used in technical analysis are chosen empirically or according to a certain rule. For example, since the parameters 12, 26 of the MACD indicator are applied in the Japanese markets, which are traded 6 days a week, they correspond to the number of 2-week and monthly bars. For algorithmic or manual transactions, these parameters vary for each market, financial asset and the monitored period. Traditionally, choosing the one that gives the best results on the historical data with the conventional approach can cause overfitting problems. In order to prevent this, verification with WFA and/or MCS after Backtest optimization creates a disadvantage. In this article, a genetic algorithm-based approach that converges to the best result is proposed, and in experimental studies, the proposed approach in all 5 different strategies outweighs conventional approaches.

Acknowledgments

This work was supported by the Scientific and Technological Research Council of Turkey (TUBITAK, Grant No. 121E733).

Declaration

The authors declare that the ethics committee approval is not required for this study.

References

- [1] Christodoulaki, E., Kampouridis, M., & Kanellopoulos, P. (2022, May). Technical and sentiment analysis in financial forecasting with genetic programming. In *2022 IEEE Symposium on Computational Intelligence for Financial Engineering and Economics (CIFER)* (pp. 1-8). IEEE.
- [2] Cheng, WK, Bea, KT, Leow, SMH, Chan, JYL, Hong, ZW, & Chen, YL (2022). A Review of Sentiment, Semantic and Event-Extraction-Based Approaches in Stock Forecasting. *Mathematics*, 10(14), 2437.
- [3] Cheng, D., Yang, F., Xiang, S., & Liu, J. (2022). Financial time series forecasting with multi-modality graph neural network. *Pattern Recognition*, 121, 108218.
- [4] Dai, C. (2022). A method of forecasting trade export volume based on back-propagation neural network. *Neural Computing and Applications*, 1-10.
- [5] Mehtab, S., & Sen, J. (2022). Analysis and forecasting of financial time series using CNN and LSTM-based deep learning models. In *Advances in Distributed Computing and Machine Learning* (pp. 405-423). Springer, Singapore.
- [6] Santur, Y. (2020). Deep learning based regression approach for algorithmic stock trading: A case study of the Bist30. *Gumushane University Journal of Science*, 10(4), 1195-1211.
- [7] Klein, T. (2022). A note on GameStop, short squeezes, and autodidactic herding: An evolution in financial literacy? *Finance Research Letters*, 46, 102229.
- [8] Sianturi, MS, & Kim, SS (2022). Technical Analysis and Value Investment in the Indonesia Stock Market. *Budapest International Research and Critics Institute (BIRCI-Journal): Humanities and Social Sciences*, 5(2).
- [9] Achyutha, PN, Chaudhury, S., Bose, SC, Kler, R., Surve, J., & Kaliyaperumal, K. (2022). User Classification and Stock Market-Based Recommendation Engine Based on Machine Learning and Twitter Analysis. *Mathematical Problems in Engineering*, 2022.
- [10] Shindler, M., Goodrich, MT, Gila, O., & Dillencourt, M. (2022). Beyond big O: teaching experimental algorithms. *Journal of Computing Sciences in Colleges*, 37(10), 23-36.
- [11] Gao, R., Du, L., Yuen, KF, & Suganthan, PN (2021). Walk-forward empirical wavelet random vector functional link for time series forecasting. *Applied Soft Computing*, 108, 107450.
- [12] Mukherjee, A., Singh, AK, Mallick, PK, & Samanta, SR (2022). Portfolio Optimization for US-Based Equity Instruments Using Monte-Carlo Simulation. In *Cognitive Informatics and Soft Computing* (pp. 691-701). Springer, Singapore.
- [13] Sang, B. (2021). Application of genetic algorithm and BP neural network in supply chain finance under information sharing. *Journal of Computational and Applied Mathematics*, 384, 113170.
- [14] Chen, T. (2021). Evaluation method of development level of Science and technology finance in Heilongjiang Province based on genetic projection Pursuit model. In *2021 International Conference on Intelligent Transportation, Big Data & Smart City (ICITBS)* (pp. 805-809). IEEE.
- [15] Wen, C., Yang, J., Gan, L., & Pan, Y. (2021). Big data driven Internet of Things for credit evaluation and early warning in finance. *Future Generation Computer Systems*, 124, 295-307.
- [16] Wang, Q., Wang, R., & Ziegel, J. (2022). E-backtesting. *arXiv preprint arXiv:2209.00991*.
- [17] Bailey, DH, & de Prado, ML (2021). How “backtest overfitting” in finance leads to false discoveries. *Significance*, 18(6), 22-25.
- [18] Öntürk, A., Ulaş, M., Karabatak, M., & Santur, Y. (2022). Python for Finance: Open Source Tools and Development of an Algorithmic Robot. *3rd International Conference on Applied Engineering and Natural Sciences*
- [19] Rodrigues, M. J. (2022). *Data Science for finance: automated investment recommendation with python* (Doctoral dissertation, Universidade Nova de Lisboa).
- [20] Olivares, KG, Garza, F., Luo, D., Challú, C., Mergenthaler, M., & Dubrawski, A. (2022). HierarchicalForecast: A Reference Framework for Hierarchical Forecasting in Python. *arXiv preprint arXiv:2207.03517*.



THE GEOMETRIES OF STABLE ISOTOPES IN TOOTH ENAMEL AND THEIR RADIATION CYCLES AND ARCHAEOLOGICAL SIGNIFICANCE

Atiye Bahar Mergen¹ , Mücahit Yılmaz^{*2} , Ezman Karabulut³ , Fatih Ahmet Çelik⁴ 

¹Bitlis Eren University, Faculty of Arts&Sciences, Art History Department, 13000, Bitlis, Turkey

²Firat University, Faculty of Science, Physics Department, 23100, Elazığ, Turkey

³Bitlis Eren University, Vocational School of Health Services, 13000 Bitlis, Turkey

⁴Bitlis Eren University, Faculty of Arts&Sciences, Physics Department, 13000 Bitlis, Turkey

Abstract

Original scientific paper

Archaeologically, the elements in the tooth enamel and their isotopes provide a lot of information about the related period, such as the way of life and nutrition culture. In this study, it was determined how the durability or brittleness of tooth enamel varies with the presence of H, C, N and S elements, which are mostly detected in tooth enamel, and their most stable isotopes, D (deuterium), ¹³C, ¹⁵N, ³⁴S elements. These elements were moved inside and on the surface of the hydroxyapatite (HAp) crystal, which is the most abundant in tooth enamel and the cornerstone of enamel. At the end of the study, it was revealed that Nitrogen (N) and Sulphur (S) elements, especially Ca atoms that ensure the durability of the HAp crystal, and Oxygen atoms make bonds that prevent electronic charge sharing. In addition, this type of bonding (in geometries holding many Ca atoms) increase the fragility as the number of Ca-O bonds decrease. At the same time, such bindings create difficulties in determining the isotopes of the relevant elements. C bonding, on the other hand, provides a strong stretching action as it provides a double bond with the Oxygen atom, so the isotopic state of the carbon atom easily shows itself. The same situation was observed for element H and its isotope D. These findings better explain the brittleness of the teeth of ancient people, especially those who were fed marine life.

Keywords: Carbon, sulphur, nitrogen, hydrogen, hydroxyapatite.

DIŞ MİNESİNDEKİ KARARLI İZOTOPLARIN GEOMETRİLERİ VE RADYASYON DÖNGÜLERİ VE ARKEOLOJİK ÖNEMİ

Özet

Orijinal bilimsel makale

Arkeolojik olarak diş minesinde bulunan elementler ve bunların izotopları, ilgili döneme ait yaşam biçimi ve beslenme kültürü gibi birçok bilgi sağlamaktadır. Bu çalışmada diş minesinde en çok tespit edilen H, C, N ve S elementleri ile bunların en kararlı izotopları olan D (döteryum), ¹³C, ¹⁵N, ³⁴S elementlerinin varlığı ile diş minesinin dayanıklılığının veya kırılabilirliğinin nasıl değiştiği tespit edilmiştir. Bu elementler diş minesinde en bol bulunan ve minenin temel taşı olan hidroksiapatit (HAp) kristalinin içine ve yüzeyine taşındı. Çalışma sonunda HAp kristalinin dayanıklılığını sağlayan Ca atomları başta olmak üzere Azot (N) ve Sülfür (S) elementleri ile Oksijen atomlarının elektronik yük paylaşımını engelleyen bağlar yaptığı ortaya çıktı. Ayrıca bu tip bağlar (çok sayıda Ca atomu içeren geometrielerde) Ca-O bağlarının sayısı azaldıkça kırılabilirliği artırmaktadır. Aynı zamanda bu tür bağlanmalar ilgili elementlerin izotoplarının belirlenmesinde de zorluklar yaratır. C bağı ise Oksijen atomu ile çift bağ sağladığı için güçlü bir germe etkisi sağlar, bu nedenle karbon atomunun izotopik durumu kendini kolayca gösterir. Aynı durum H elementi ve onunun D izotopu için de gözlemlenmiştir. Bu bulgular, özellikle deniz yaşamıyla beslenen eski insanların dişlerinin kırılabilirliğini daha iyi açıklamaktadır.

Anahtar Kelimeler: Azot, hidrojen, hidroksiapatit, karbon, sülfür.

1 Introduction

The utility of stable carbon, nitrogen, and sulphur isotope analysis derives from the expression that means that you are what you eat. Since its primitive applications in anthropology in the 1970s [1, 2], stable isotope analysis

is now widely used to study past human diet through time and across space. The analysis of stable isotopes is also important in the tool kit of bioarchaeologists, who are curious about human past diet or human provenience [3, 4]. An examination of the component parts of stable isotopic paleodietary provided a revolutionary suite of

*Corresponding author.

E-mail address: bmergen@beu.edu.tr (A. Bahar Mergen)

Received 15 May 2023; Received in revised form 17 July 2023; Accepted 04 August 2023

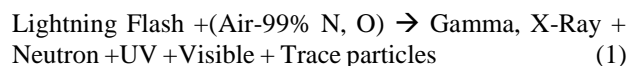
2587-1943 | © 2023 IJIEA. All rights reserved.

Doi: <https://doi.org/10.46460/ijiea.1297247>

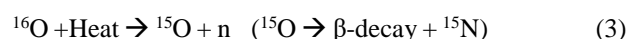
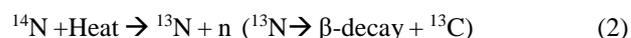
tools for bioarchaeologists interested in reconstructing past dietary behaviour also related to population adaptation. Stable isotopes do not change over time, although their concentrations change with physico-chemical processes such as evaporation and condensation [5]. Such stable isotopes in relative abundance can be found experimentally by isotope analysis and a found isotope ratio can be used as a test tool. It can be said who in nature is affected by the abundance of isotope fractionation relative to each other. The differences do not alter to any great extent the chemical properties of the atom, but of course, do change the physical properties. Fry [6] stated that lighter isotopes such as hydrogen (H), carbon (C), nitrogen (N), Oxygen (O), Sulphur (S) constitute between 95%–99.6% of their natural abundance whereas heavier isotopes only constitute between 1%–5%. Stable isotope ratio described as the ratio of the heavy isotope to the light isotope such as $^{13}\text{C}/^{12}\text{C}$, $^{15}\text{N}/^{14}\text{N}$ in connection with a known standard. The methods investigate the chemical composition of bones or teeth for the reconstruction of paleodiet provide the most relevant information about the original contents of the diet. The stable isotope analyses have been found an established method for reconstructing infant feeding and weaning practices, paleodiet, geographic origin, migration routes from the human skeletal and dental remains [7]. The various tissues of the human body are principally composed of atoms of elements such as carbon, hydrogen, nitrogen, sulphur, oxygen, and phosphorus which have significant variations in all of the isotope ratios. If a human has been eating a uniform diet for a period of time that is long compared with the rate of turnover of a given tissue, then the isotope ratio of each tissue and organic molecule in the body will achieve a steady state value. That value will generally differ from that of the dietary intake (fractionation between the tissue and the diet). The overall isotopic composition means weighted mean of all components itself represents a steady state between intake and outputs such as urine, feces, expired CO, and H, O in normal conditions [8]. Considering that rain water accumulates in the seas and fresh water resources, it can be mentioned that the accumulation percentages of carbon and nitrogen isotopes in tooth enamel are higher in the diets in these geographies and brittleness increases in these geographies. [9]. Variation in trophic level, photosynthetic pathway, and environmental conditions with other biogeochemical processes can also have a strong influence over patterning of the natural abundances of ^{13}C and ^{15}N in aquatic, and especially freshwater, environments. Because these biogeochemical processes often play an important role in structuring the isotopic composition of aquatic food webs at a range of spatial and temporal scales, it is important that they are adequately considered in isotopic studies of past human and animal populations [10]. In the examination of adult teeth, the data obtained from the enamel of deciduous or permanent teeth showed that the development was completed in childhood and isotopic developments were more important at that time. [11]. Tooth enamel develops together with the dentin part of the tooth. However, since it does not have a self-repetitive feature, it is shaped in the developmental processes of childhood. [12]. It has been seen that it is possible in today's scientific age to take

weekly or even daily records of historical processes from some scales rather than months and years. However, meanings can be deduced from tooth enamel in different periods (depending on age, in childhood and adulthood). [13]. It differs from bone collagen and dentin in that the enamel is resistant to deformation and deterioration. [14].

Stable isotopes in nature occur in high temperature plasma environments. these environments are often known as lightning flashes. Nuclear-based radiations such as neutrons and gamma rays, which are produced by lightning strikes, are emitted:



According to Eq. (1), neutrons are released from N and O atoms in the air, which are referred to as trace particles. These enter the stable isotope cycle as follows:



As can be seen from Eq. (2) and Eq. (3) above, the effect of lightning flashes on isotopes is very effective when both the stable isotopes formed by the unstable trace elements when they become stable and the stable isotopes that the free neutron can form by interacting with the N and O atoms in the air under collision statistical. It is a fact that the isotope population will be effective in places where precipitation or lightning flashes are effective. As these isotope gas molecules interact with water and enter living life with groundwater, they become partners in the life cycle.

2 Materials and Methods

2.1 Computational Method

With the chewing of the foods containing the isotope, the related elements take their place in the tooth enamel in a child in the developmental age. Tooth enamel is composed of HAp crystal structure. The unit cell ($a=b=9.424$ and $c=6.879$) of this structure was designed as described in the literature [15]. In the system, the bulk structure and the fermi electronic temperature were set at room temperature. The simulation was carried out under the AMS (Amsterdam Modelling Suit) infrastructure by using DFTB3 (third degree density function tight-binding) approach and D4 electronic dispersion as a model [16]. In determination of stable structures by both optimization and PES-Exploration, the 3ob-3-1 function suitable for HAp and isotopic additives was determined as a parameter.

Known as the base substance for tooth enamel and dentin, HAp crystal is the cornerstone of tooth strength. In tooth decay or fracture, the durability of the tooth varies with the breaking of Ca-O bonds or entering into chemical reactions. This reaction starts to react with CaOH, which supports to pH change [17, 18]. Therefore, the decrease in Ca-O bonds reduces the durability of the tooth.

3 Results and Discussions

HAp crystal was used for simulation as the basic lattice form, $\text{Ca}_{10}(\text{PO}_4)_6(\text{OH})_2$. ^1H , ^{12}C , ^{14}N and ^{34}S atoms and their most stable isotopes (^2D , ^{13}C , ^{15}N , ^{34}S) were moved in the system to determine the most stable structure on and inside the Crystal surface. Differences in IR vibrations and isotope effects on the most stable structures were tried to be determined. It was also discussed whether these isotopes affect the strength of the HAp crystal. The fundamental vectors of the crystal structure in three dimensions are as follows:

VEC1	9.39685455	0.00000000	0.00000000
VEC2	-4.69842728	8.13791476	0.00000000
VEC3	0.00000000	0.00000000	6.86402560

First, the most stable states were determined by moving the H atom on and inside the HAp crystal surface. As in Fig. 1, “process search” was used to detect transition and minimum points with PES-Exploration. Fig. 1 shows the diagram of these transitions. The most stable configuration is shown in Fig. 2.

In Fig. 1, the most stable energy level is achieved when the H atom is bonded to the phosphorus (P) atom, referenced to "0" Hartree. A total of 8 transition and minimum energy points were detected, depending on the movement of the H atom on and inside the crystal surface via Pes-Exploration. In other high-energy states, the "H" atom is bonded to the "O" atom. Fig. 2 gives a detailed view of the binding of the most stable level. These energy levels in Fig. 1 were detected in best electronic dispersion. It shows the "H" atom that wants to bind to the (OH) endpoint of the $\text{Ca}_{10}(\text{PO}_4)_6(\text{OH})_2$ (HAp) crystal in higher energy states. In this case, the system becomes unstable. These points will make the unstable system react. It is estimated as the first step in the formation of hydrolysed environments in cases such as the mechanism of decay. However, this end region is the region where there is no effect on the brittleness of the crystal under any external pressure. Another binding site of the H atom is the bonding to the "O" atoms to which the "Ca" atom bonds.

Binding to this region occurs at unstable high energy levels. This unstable state increases the fragility of tooth enamel. Because the bonding of Ca atoms with "O" atoms is the indicator of this hardness. The resistance of atoms to a certain stress under any external pressure is at the forefront with their Ca-O bonding. The higher the number of Ca-O bonds, the stronger the crystal. The change in the degree of bonding in the CaO bond group occurs under high pressure. Or it happens with the help of a different external influence.

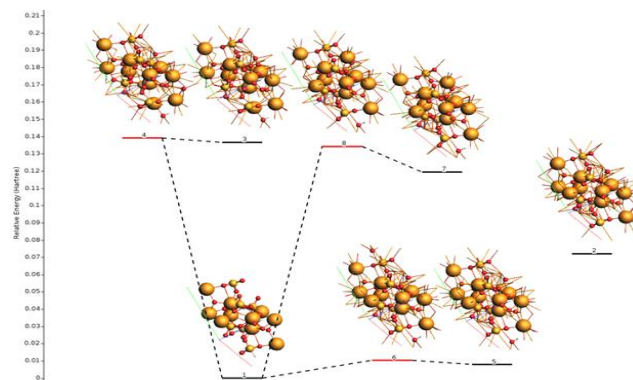


Figure 1. The energy levels obtained by using Pes-Exploration with “Process Search” task.

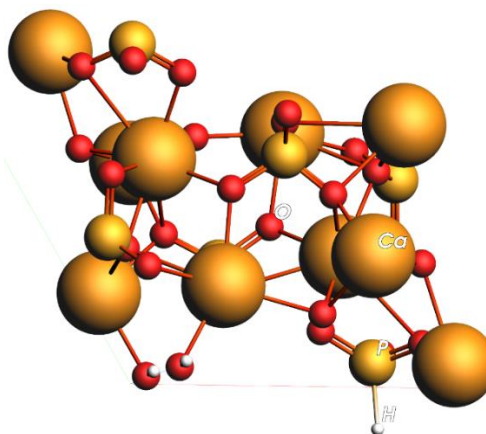


Figure 2. Representation of the most stable binding of the H atom in the HAp crystal. (Symbols of the elements are indicated on the Figure. Atoms of the same kind are shown in the same colour and size.)

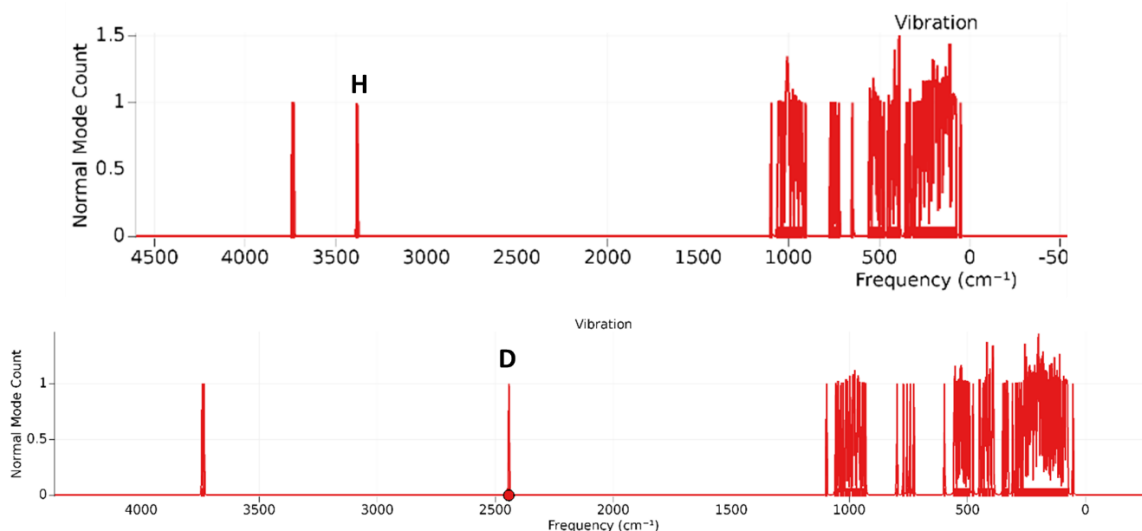


Figure 3. Vibration frequency energy values in the HAp crystal of H (upper part) and D (bottom part) atoms.

The upper part of Fig. 3 shows the frequency at which the Hydrogen atom is in the HAp crystal, while the lower part of the figure shows the vibrational frequency at which the deuterium atom is located. The only different point in both frequency ranges is the oscillation frequency, which indicates the difference between H and its isotope D. In this figure, the vibrational frequency of the phosphorus - bound H-atom in the spectrum is shown at a frequency of 3384 cm^{-1} . It is well known that the H atom is a light mass atom capable of strong stretching action. Thanks to this feature, it is very easy to detect this element and its isotopes in a tooth enamel. With twice the mass difference, the oscillation frequency difference is seen in detail. Although the attachment of the H atom to the oxygen structures in the crystal structure is not shown here, the isotope difference will be evident there as well. The bonds of the H atom with the oxygen atoms in the crystal cause IR oscillations at $3624, 3736, 3762, 3749, 3730, 3742\text{ cm}^{-1}$ frequencies in more unstable structures. In this study, the most stable region where the H-atom can bond was determined and isotope determination was made only on this structure. The deuterium emission frequency is around 2400 cm^{-1} . The highest oscillation frequency in Fig. 3 belongs to the tip region of the HAp crystal (OH). It does not belong to the externally doped H atom. 1000 cm^{-1} and lower oscillations are buckling and bending

oscillations in the crystal. The isotopic study of the H atom adsorbed to the HAp crystal can be easily detected.

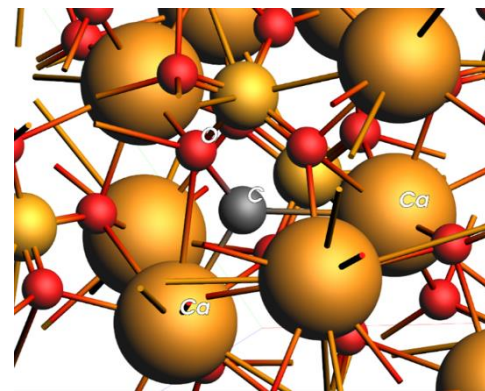


Figure 4. Stable geometric structure of C element in HAp crystal.

Another doped element is "C" carbon. As seen in Fig. 4, the element carbon is bonded to 2 Ca atoms and 1 oxygen atom. In such a bonding, the vibrational frequency difference of the isotopes will show the C-O junction. It is very difficult to determine the isotope difference in the crystal in C-Ca binding. Fig. 5 shows the difference in vibrational oscillations of carbon isotopes. The isotope values of C-O stretching movement are ^{13}C at 1121 cm^{-1} and ^{12}C at 1130 cm^{-1} .

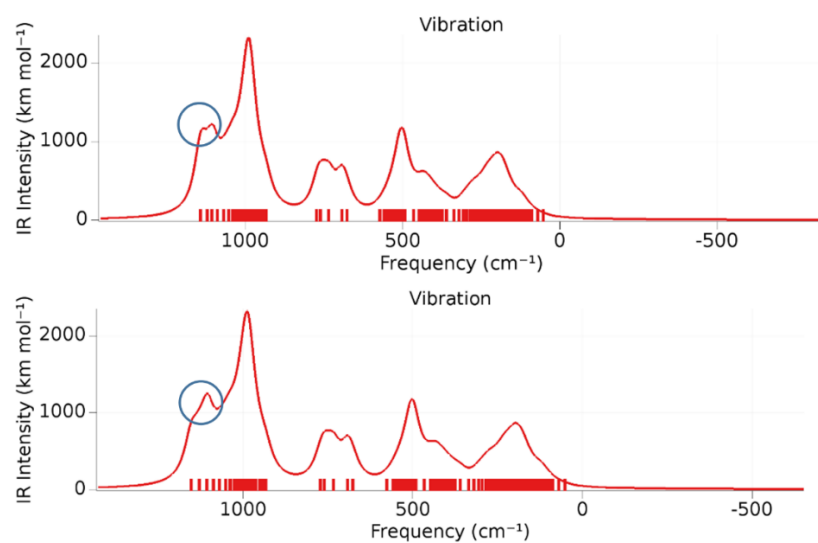


Figure 5. The top side of the figure is ^{12}C and the bottom side is the oscillation frequencies of the ^{13}C element. The difference between the two distributions is the frequency range indicated by the blue ring on the graph of the C-O stretching motion.

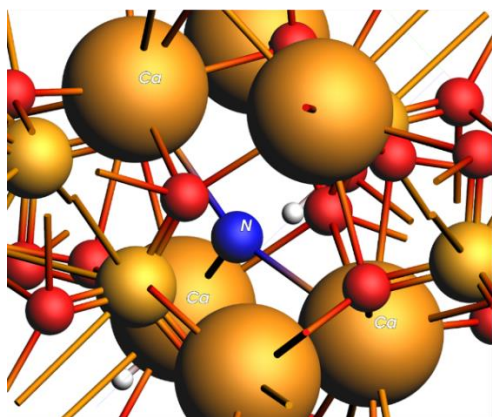


Figure 6. Geometric position of the element Nitrogen in the HAP Crystal.

Another doped element is the nitrogen atom. The most stable structure of the nitrogen atom in the HAP crystal occurs when three Ca atoms form a single bond (see Fig. 6). In such a case, it is very difficult to determine the ^{15}N isotope. The vibration spectra are similar to each other due to the heavy structure of the Ca atom and the triple bond. However, if the N atom is positioned somewhere between Ca and Oxygen, oscillations can be seen at ^{14}N (1682 cm^{-1}) and ^{15}N (1653 cm^{-1}) frequencies. These oscillations are in the N=O double bond state.

Another doped element is sulphur element. This element also bonds to 3 Ca atoms in the HAP crystal (see Fig. 7). Like nitrogen, isotopic oscillation differences in binding to Ca crystal are difficult to determine with IR frequencies.

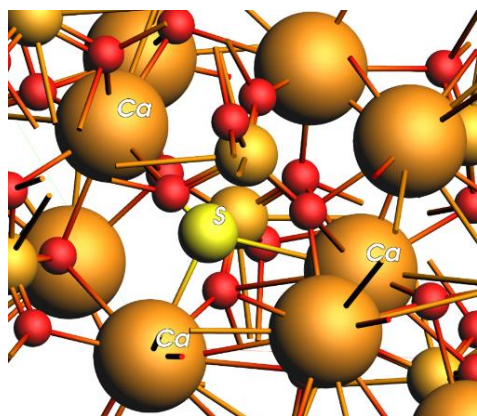


Figure 7. Geometric position of the element Sulphur in the HAP Crystal.

4 Conclusion

The H, C, N and S elements and the HAP crystal in which their isotopes are doped were examined in this study. H and C elements, due to their binding to the oxygen atom, show the situations where IR analysis is sufficient in isotopic differences with their stretching action. However, N and S elements, on the other hand, are very difficult to determine their isotopic differences with the IR spectrum due to their binding to the Ca element. The strength of tooth enamel is also directly dependent on the positions of these doped elements. Under any external pressure, the degree of Ca-O binding is directly affected. When these elements, which are doped from the outside and placed in the crystal, affect the Ca-O bonding, they will affect the strength of the $\text{Ca}_{10}(\text{PO}_4)_6(\text{OH})_2$ crystal, which is known as the calcium salt. Archaeologically, it enters the life cycle when isotopic elements, which occur with nuclear reactions in the atmosphere under high temperature, in regions with abundant precipitation and lightning flashes, pass into the earth's waters with rain water. Isotopic densities can explain the strength or fragility of teeth, while providing some information from the past. In particular, the contribution of carbon and nitrogen atoms to tooth enamel fracture is explained by the bonds they make with oxygen atoms.

Declaration

The authors declare that the ethics committee approval is not required for this study.

References

- [1] Vogel, J. C., & Van Der Merwe, N. J. (1977). Isotopic evidence for Early Maize cultivation in New York State. *American Antiquity*, 74, 298-301.
- [2] Van der Merwe, N. J., & Vogel, J. C. (1978). ^{13}C content of human collagen as a measure of prehistoric diet in woodland North America. *Nature*, 276, 815-816.
- [3] Lagia, A. (2015). Diet and the polis: An isotopic study of diet in Athens and Laurion during the classical, Hellenistic, and imperial Roman periods. *Archaeodiet in the Greek world: Dietary reconstruction from stable isotope analysis*, 119-45.
- [4] Federico L., Cipriani, A.; Capecchi, G., Ricci, S., Boschin, F., Boscato, P., Iacumin, P., Badino, F., Marcello A. Mannino, S.T., Richards, M. P., Benazzi, S., & Ronchitelli, A. (2019). Strontium and stable isotope evidence of human mobility strategies across the Last Glacial maximum in southern Italy. *Nature Ecology & Evolution* 3, 905–911.
- [5] Faure, G., & Mensing, T. M. (2005). *Principles and applications*. John Wiley & Sons, Inc.
- [6] Fry, B. (2006). *Stable isotope ecology* (Vol. 521, p. 318). New York: Springer.
- [7] Fuller, B. T., Fuller, J. L., Harris, D. A., & Hedges, R. E. M. (2006). Detection of breastfeeding and weaning in modern human infants with carbon and nitrogen stable isotope ratios. *American Journal of Physical Anthropology*. 129, 279-293.
- [8] Schwarcz, H. P., & Schoeninger, M. J. (1991). Stable isotope analyses in human nutritional ecology. *Yearbook of Physical Anthropology*, 34, 283-321.
- [9] Passey, B. H., Robinson, T. F., Ayliffe, L. K., Cerling, T. E., Sponheimer, M., Dearing, M. D., Roeder, B. L., & Ehleringer, J. R. (2005). Carbon isotope fractionation between diet, breath CO_2 , and bioapatite in different mammals. *Journal of Archaeological Science*, 32, 1459-1470.
- [10] Guiry, E. (2019). Complexities of stable carbon and nitrogen isotope biogeochemistry in ancient freshwater ecosystems: Implications for the study of past subsistence and environmental change. *Frontiers in Ecology and Evolution* 7, Article 313.
- [11] Liversidge, H., & Molleson, T. (2004). Variation in crown and root formation and eruption of human deciduous teeth. *American Journal of Physical Anthropology*, 123(2), 172-180.
- [12] Hillson, S. (2005). *Teeth*. Cambridge, Cambridge University Press, (2nd Edition), England.
- [13] Reid, D. J., & Dean, M. C. (2006). Variation in modern human enamel formation time. *Journal of Human Evolution*, 50(3), 329-346.
- [14] Lee-Thorp, J. A. (2008). On isotopes and old bone. *Archaeometry*, 50(6), 925–950.
- [15] Knupp, W.G., Ribeiro, M. S., Mir, M., Camps, I. (2019). Dynamics of Hydroxyapatite and Carbon Nanotubes Interaction. *Applied Surface Science*, 495, 143493.
- [16] Software for Chemistry & Materials (2022). Retrieved September 20, 2022 from <http://www.scm.com>.
- [17] Collins, M. J., Nielsen-Marsh, C. M., Hiller, J., Smith, C. I., Roberts, J. P., Prigodich, R. V., & Turner-Walker, G. (2002). The survival of organic matter in bone: a review. *Archaeometry*, 44(3), 383-394.
- [18] Götherström, A., Collins, M. J., Angerbjörn, A., & Lidén, K. (2002). Bone preservation and DNA amplification. *Archaeometry*, 44(3), 395-404.



ENERGY CONSUMPTION FORECAST FOR THE BUILDING SECTOR IN TURKEY UNTIL 2030

Nazile Yılkırkan^{*1}, Esra Nur İçme²

¹Sivas Cumhuriyet University, Faculty of Technology, Department of Mechatronics Engineering, Sivas, Türkiye

²Memorial Kayseri Hospital, Kayseri, Türkiye

Abstract

Original scientific paper

As in the rest of the world, energy consumption is increasing in Turkey as a result of population growth and technological developments. Energy efficiency studies are becoming more and more important for Turkey, which meets more than half of its energy needs from imported sources. When the sectors where energy is consumed intensively are analyzed, it is seen that the share of building sector energy consumption in total energy consumption is approximately 20%. This high rate shows that energy efficiency studies in the building sector will reduce the amount of energy imports and the current account deficit, as well as help to ensure the security of supply.

In this study, Turkey's population, Gross Domestic Product (GDP), number of buildings and the total amount of energy consumed in buildings in the past 20 years are used to estimate how much energy will be consumed in the building sector for the future. Within the scope of the study, how much energy will be consumed in the building sector in Turkey until 2030 is estimated by using the Artificial Neural Networks (ANN) method in Matlab program. It is calculated that Turkey will consume 37.868 thousand Tons of Oil Equivalent (TOE) of energy in the building sector in 2030. In addition, the importance of energy efficiency studies in the building sector is emphasized.

Keywords: Energy, energy efficiency, energy consumption in buildings, artificial neural networks.

TÜRKİYE'DE 2030 YILINA KADAR BİNA SEKTÖRÜNDEKİ ENERJİ TÜKETİM TAHMİNİ

Özet

Orijinal bilimsel makale

Dünya genelinde olduğu gibi Türkiye'de de nüfus artışı ve teknolojik gelişmelerin sonucu olarak enerji tüketimi artmaktadır. Enerji ihtiyacının yarısından fazlasını ithal kaynaklardan karşılayan Türkiye için enerji verimliliği çalışmaları her geçen gün daha önemli hale gelmektedir. Enerjinin yoğun olarak tüketildiği sektörler incelendiğinde bina sektörü enerji tüketiminin, toplam enerji tüketimi içerisinde payının yaklaşık olarak 20% gibi bir orana sahip olduğu görülmektedir. Bu yüksek oran bina sektörde enerji verimliliği çalışmaları sayesinde enerji ithalat miktarını ve cari açığı azaltacağını aynı zamanda arz güvenliğini sağlamaya yardımcı olacağını göstermektedir.

Bu çalışmada Türkiye'nin geçmiş 20 yıldaki nüfus, Gayri Safi Yurtiçi Hâsıla (GSYH), bina sayısı ve binalarda tüketilen toplam enerji miktarı verilerinden yararlanılarak geleceğe yönelik bina sektöründe ne kadar enerji tüketileceği tahmin edilmeye çalışılmıştır. Çalışma kapsamında, Türkiye'nin 2030 yılına kadar bina sektöründe ne kadar enerji tüketileceği Matlab programında Yapay Sinir Ağları (YSA) metoduyla tahmin edilmiştir. Yapılan tahminde Türkiye'nin 2030 yılında bina sektöründe 37.868 Bin Ton Eşdeğeri Petrol (TEP) enerji tüketileceği hesaplanmıştır. Ayrıca, bina sektöründe enerji verimliliği çalışmalarının önemi vurgulanmıştır.

Anahtar Kelimeler: Enerji, enerji verimliliği, binalarda enerji tüketimi, yapay sinir ağları.

1 Introduction

Energy consumption is increasing along with population growth worldwide. When energy consumption is analyzed from past to present, it is seen that fossil fuels are consumed predominantly. As an alternative to fossil fuels, there has been a significant increase in the consumption of renewable energy sources in recent years. The increase in the share of renewable energy sources in total energy consumption is very important both for the

economies of countries and for slowing down global warming. To slow down global warming, the importance of energy efficiency as well as the spread of renewable energy sources has been realized and energy efficiency studies have started to gain importance worldwide.

When the energy-consuming sectors are analyzed, the building sector has approximately one-fourth of the total energy consumption. This situation increases the importance of energy saving and energy efficiency studies in the building sector. Turkey meets a significant portion

*Corresponding author.

E-mail address: nyilkirkan@cumhuriyet.edu.tr (N. Yılkırkan)

Received 31 August 2023; Received in revised form 08 November 2023; Accepted 22 December 2023

2587-1943 | © 2023 IJIEA. All rights reserved.

Doi: <https://doi.org/10.46460/ijiea.1352958>

of its energy needs from imported sources and the economic cost of this situation is quite high. For this reason, energy efficiency is of critical importance in reducing energy demand and foreign dependency. Looking at energy efficiency on a sectoral basis, there is a great potential for energy savings in buildings.

Energy efficiency can be defined as reducing energy consumption without damaging the quality and quantity of production in industry and without reducing the standard of living and service quality in buildings. [1].

The increase in population, improvement in living standards, development of technology and the increase in energy demand lead to an increase in energy consumption and thus environmental pollution [2]. Buildings account for 30-40% of the world's primary energy consumption and 40% of greenhouse gas emissions [3]. Energy efficiency studies in the building sector, which causes such high rates of energy consumption and greenhouse gas emissions, have started to be prioritized by decision-makers. With the enactment of the National Energy Efficiency Action Plan (NEEAP) by the Ministry of Energy and Natural Resources of the Republic of Turkey within the scope of efficiency studies, it is aimed to reduce Turkey's primary energy consumption by 14% in 2023 with 55 actions defined in 6 categories: energy, buildings and services, industry and technology, transportation, agriculture and horizontal agriculture. With this plan, investments were made for energy efficiency in 2017-2021 and as a result, 4.473 kTEP energy savings were achieved [4].

Heating/cooling, hot water and ventilation systems account for 75% of energy consumption in residential buildings, while lighting systems account for 50% of total consumption in public and service buildings [5]. It is seen that a 5% reduction in electricity consumption can be achieved by switching to compact fluorescent instead of incandescent lamps used in residential buildings in Turkey, and at the same time, the savings realized will contribute to the target of 20% reduction in energy intensity in 2023 by looking at the 2011 rate [6].

With the artificial neural network based modeling method, the energy required for heating/cooling in buildings can be determined by simulation. In the artificial neural network (ANN) model, it is envisaged that heating and cooling loads can be calculated while the building is in the design process by selecting buildings in different design models as input and heating load as output [7].

Multi-output and single output regression methods can be used with machine learning to estimate the energy consumed for heating/cooling in buildings. With the multi-output regression method, these can be compared and it is seen that the energy load in buildings can be greatly reduced [8]. Building energy consumption can be predicted by teaching many data such as area-volume, heating type, and building typological characteristics as input to the ANN model [9].

Successful results are obtained in energy consumption forecasting studies conducted with ANN. In the study where Turkey's net energy consumption was estimated with the help of ANN and Adaptive Network Based Fuzzy Inference System (ANFIS) models using import, export, GDP and population data, both models were found to be successful in energy consumption forecasting [10].

Another study showed that ANFIS and ANN forecasting models can be used as energy supply forecasting tools and it was concluded that ANN can be used in studies with less data since it allows working with less data. [11]. In another study conducted for electric energy demand forecasting, ANN was found to give successful results among forecasting models [12].

Turkey's population, GDP and primary energy supply data were used to determine the future energy needs of Turkey by using ANN and it was observed that ANN gave successful prediction results [13]. In a study on the statistical estimation of residential energy consumption in Turkey in 2030, it was determined that residential energy consumption in that year will be 48 million TOE and the 95% confidence interval is 37-59 million TOE. In other words, a minimum of 37 and a maximum of 59 million TOE is expected. It is also stated in the study that the effect of the GDP index on energy consumption was found to be high [14].

In this study, the building energy consumption forecast for 2030 was found to be approximately 38 million TOE. In the data set applied to the model, it was observed that the decline and slowdown in GDP and the resulting decline in energy consumption in some years caused a slow increase in the forecast data in the model result. In case of a steady increase in GDP, energy consumption is expected to be higher.

This study aims to calculate how much energy will be needed in 2030 in the building sector, which has a significant share in sectoral energy consumption in Turkey. By estimating the amount of energy to be consumed, it is aimed to draw attention to the importance of energy efficiency studies in this sector.

This study is considered to be a reference source as it is one of the few studies that estimate how much energy will be consumed in buildings in Turkey in 2030. It is aimed to guide institutions and researchers on the factors affecting energy consumption in buildings, the negative effects of building energy consumption on the environment and the importance of energy efficiency in buildings.

2 Building Sector Energy Consumption and CO₂ Emissions

According to the most recent reports published by the Ministry of Energy and Natural Resources (the latest data published for 2021), 34% of sector-based energy consumption in Turkey is in industry, 25% in transportation, 21% in buildings, 10% in commercial enterprises and 10% in other areas. [15]. Efficiency studies are of great importance in these sectors where energy consumption is high. When the data are analyzed, it is seen that the share of building sector energy consumption in total energy consumption is high.

When the data for 2021 in Turkey are analyzed, the number of buildings increased by 131,8% and the number of apartments by 105,6% compared to the previous year. For the same year, 58,6% of the total surface area in Turkey was determined as residential area [16]. As a result of this, energy consumption in the building sector also increases at the same rate.

Figure 1 shows the energy consumption in the buildings and services sector in Turkey between 2000 and

2021. Energy consumption in this sector was 19,556 thousand TOE in 2000 and 38,121 thousand TOE in 2021.

Energy consumption in buildings refers to the amount of energy used in residential, commercial and institutional

buildings. Buildings consume energy for various purposes, including heating, cooling, lighting, appliances and other electrical devices.

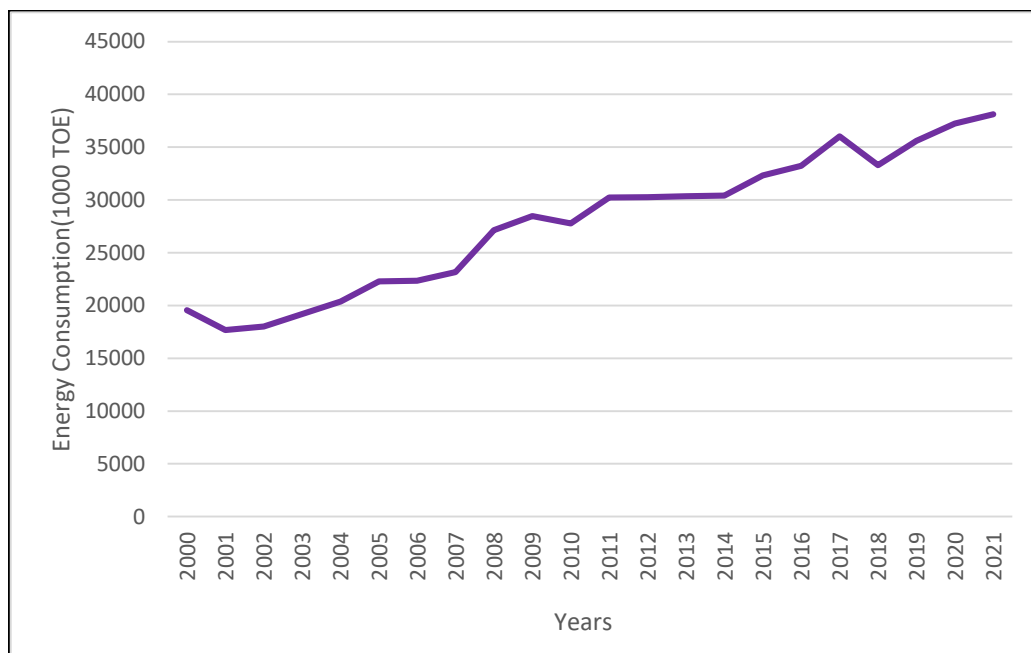


Figure 1. Energy consumption in buildings and services sector in Turkey (2000-2021) [15].

The distribution of energy consumption by sources in the building sector in Turkey in 2021 was realized as Natural Gas 13,760, Electricity 5,289, Renewable resources 2,940, Hard coal 1,963 and Other resources 2,196 thousand TOE. [15]. It is seen that the share of Natural Gas, which is an imported source, in total consumption is significantly higher and this situation increases both the current account deficit due to the fact that natural gas is an imported source and CO₂ emissions due to the fact that it is a fossil fuel.

It is observed that energy consumption in the building and services sector has almost doubled in the last 20 years. The increase in energy consumption causes a significant increase in CO₂ emissions in this sector. Turkey's sectoral CO₂ emission rates were realized as 37% Transportation sector, 34% Industry sector and 29% Building and services sectors as of 2021 [17].

Buildings cause 48% of CO₂ emissions in the world and 29% of CO₂ emissions in Turkey [17,18]. CO₂ emissions caused by the building sector threaten sustainable future plans. Energy efficiency studies in buildings gain great value at this point.

3 Materials and Methods

Within the scope of this study, an ANN model was created using MATLAB program. The ANN model was trained and tested on the dataset including population, GDP, number of buildings and final energy consumption values between 2000-2021 in Turkey. As a result of the tests, the final energy consumption in the residential and services sectors in Turkey between 2022-2030 was estimated by using the model with high regression value.

3.1 Analysis Data

In this study, data on population, GDP and number of buildings in Turkey between 2002 and 2021 were entered as input to the ANN model created in this study. Final energy consumption data in the building and services sectors were determined as output data. Table 1 shows the dataset on which the ANN model will be evaluated.

In this study, multilayer perceptrons, which are the most appropriate ANN models, are used to predict energy consumption data in the building and services sector from population, GDP and number of buildings data. Multilayer perceptron consists of input, output and hidden layers. These layers are feed-forward and supervised networks with connections between them. Population, GDP and number of buildings, which are determined as independent variables, are given as inputs to the ANN model, while the amount of energy consumption in the housing and services sector, which is determined as the dependent variable, is obtained as the output of the ANN. The simple ANN for energy consumption forecasting has one hidden layer.

3.2 Artificial Neural Network

ANN is a computational method that models the biological structure of the human brain and consists of layers. ANNs are also mathematical models consisting of interconnected nodes that can be defined as artificial nerve cells, or neurons. The input signals to the nodes are multiplied by certain weights and summed, and the bias value is added to this total value. The resulting signal is then passed through the activation function to generate the output signal. Figure 2 shows the structure of an artificial neural cell.

Table 1. ANN analysis dataset (2000-2021) [15,16,19].

Years	Population (thousand)	GDP (Million USD)	Number of Buildings (Number)	Final Energy Consumption (thousand TOE)
2002	66.402	240.191	7.926.331	18.000
2003	67.187	314.752	8.014.767	19.178
2004	68.010	409.127	8.096.901	20.391
2005	68.861	506.186	8.201.819	22.284
2006	69.730	555.126	8.339.328	22.355
2007	70.586	680.489	8.480.767	23.172
2008	71.517	770.820	8.624.892	27.145
2009	72.561	648.797	8.795.733	28.470
2010	73.723	776.558	8.972.636	27.762
2011	74.724	838.508	9.153.106	30.230
2012	75.627	880.141	9.347.208	30.259
2013	76.668	957.504	9.563.904	30.348
2014	77.696	938.512	9.809.347	34.186
2015	78.741	864.071	10.044.061	32.329
2016	79.815	869.280	10.265.648	33.221
2017	80.811	858.932	10.495.833	36.015
2018	82.004	779.694	10.741.752	33.298
2019	83.155	760.516	10.962.749	35.609
2020	83.614	719.919	11.134.476	37.234
2021	84.680	806.804	11.304.492	38.121

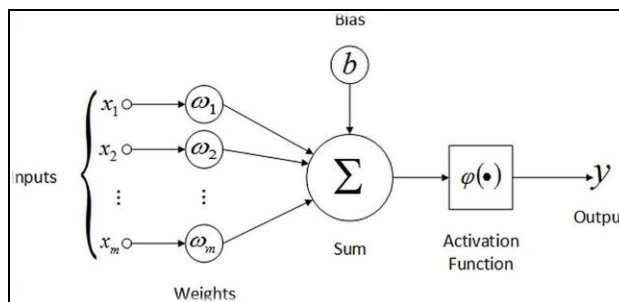


Figure 2. Artificial Neural Cell [20].

There are basically 3 layers in an ANN: Input layer, intermediate (hidden) layer and output layer. There can be more than one hidden layer between the input and output layers. Hidden layers enable the model to learn by using the information in the input. In the input layer, numerical data or images are received and an output value is generated using the weights of the network. In the output layer, possible predictions and classifications are made using the output values obtained.

In the training of the ANN, the input data is initially multiplied by randomly determined weights, then the bias value is added and an output is obtained. This output value is then passed through an activation function to make it nonlinear. The final output value is compared with the actual output value and the mean square error (MSE) is calculated. Using the calculated error value, the weights in the ANN are updated. Updating the weights is done by a technique called back propagation. This back propagation performs gradient calculations according to the weights of the network errors and updates them to minimize the error. With these calculations, the network learns and improves its performance over time.

4 Finding and Discussion

While training the ANN, weights are generated according to a specific algorithm. Although the number of neurons in the hidden layers is determined without being dependent on any rule, it is generally seen in the literature that ANN analysis is performed with 10, 11 and 12 neurons in the input layer [21]. While determining the number of neurons in the hidden layer, networks with different numbers of neurons have been tested and in this study, the most appropriate number of neurons was determined to be 10. Figure 3 shows the ANN model used in this study.

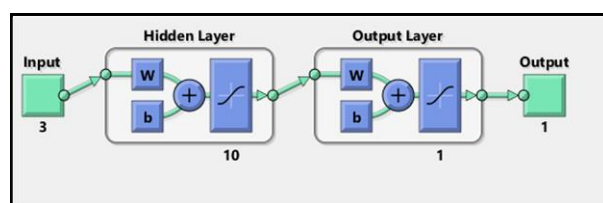


Figure 3. Artificial Neural Network Layers

While creating the model in ANN, 15% of the data was used for validation, 15% for test and 70% for training. The training process of the network was completed in 9 iterations. The lowest MSE value was reached at the 6th iteration. Figure 4 shows the performance graph of the model depending on iteration and the MSE value was found to be 6.2566e-10. A small MSE value means that the accuracy of the prediction is high.

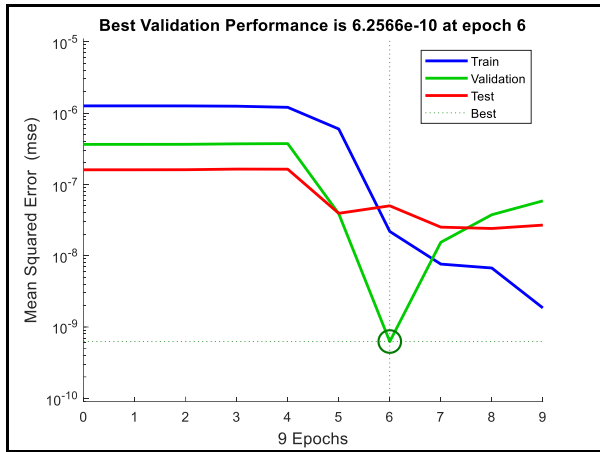


Figure 4. Error performances

Figure 5 shows the correlation coefficient (R) plots showing the performance of the model. Looking at the correlation coefficient values in Figure 5, R = 0.9823 for training data, R = 0.99045 for validation data, R = 0.9886 for test data and R = 0.97671 for all data. The fact that the values are close to 1 for all data indicates that there is agreement between the data obtained with the ANN model and the real data.

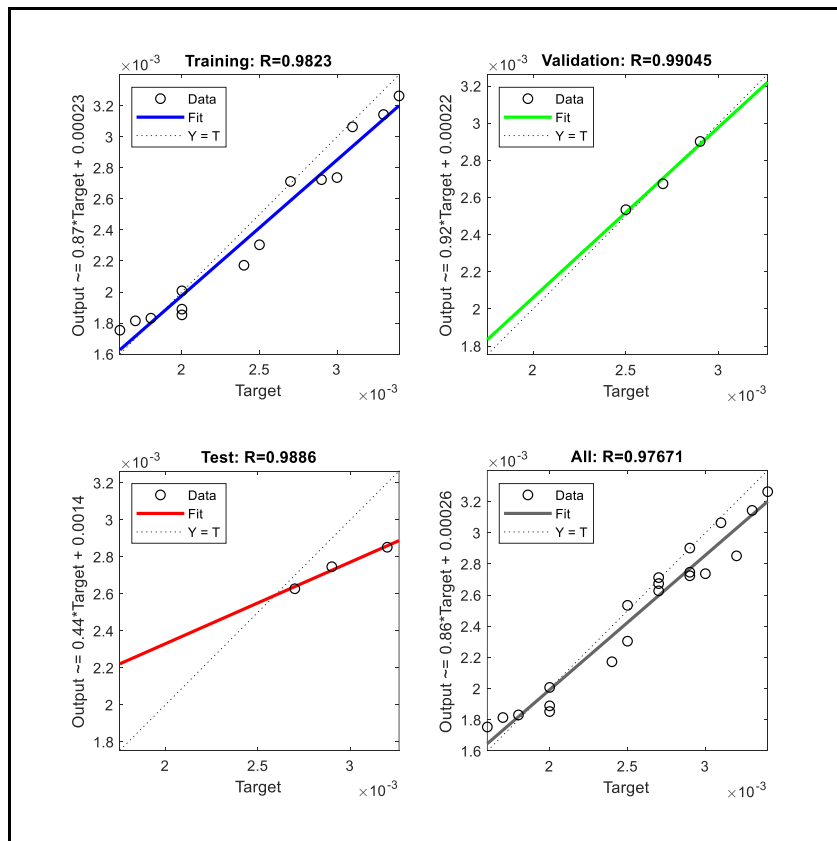


Figure 5. Regression values.

Population data, which is one of the data determined as input neurons to this network between 2022 and 2030, is taken directly from the future population scenarios of the Turkish Statistical Institute (TSI), while the scenarios for the other independent variables, GDP and number of buildings, are calculated by simple regression method. In regression calculation, the relationship between two independent and dependent variables is analyzed.

In this study, the population values between 2022 and 2030, which are used as independent variables in regression analysis, are the data taken from TSI population scenarios. GDP and number of buildings, which are dependent on population, are calculated with the regression equation given below.

In the Equation (1), y is the dependent variable, x is the independent variable, β_0 is the intercept term, β_1 is the slope coefficient and ϵ is the error term [22].

$$Y = \beta_0 + \beta_1 \cdot x + \epsilon \tag{1}$$

The x value given in this equation expresses the independent variable population, while the y value expresses independent variables such as GDP and number of buildings.

In Table 2, the population values between 2022-2030 are taken from the population scenarios of the TSI [23]. Using this population data, GDP and number of buildings data were found by regression calculation and then final energy consumption was estimated by ANN modeling using population, GDP and number of buildings values. Final energy consumption estimation values are given in Table 2.

Table 2. ANN analysis for prediction data (2022-2030).

Years	Population (thousand)	GDP (Million USD)	Number of Buildings (Number)	Final Energy Consumption (thousand TOE)
2022	85.286	961.849	11.315.039	37.322,91
2023	86.154	983.856	11.480.379	37.655,26
2024	87.003	1.005.377	11.642.073	37.786,39
2025	87.832	1.026.397	11.800.002	37.824,83
2026	88.641	1.046.896	11.954.018	37.916,40
2027	89.428	1.066.854	12.103.966	37.862,14
2028	90.193	1.086.250	12.249.697	37.862,14
2029	90.935	1.105.067	12.391.075	37.918,66
2030	91.654	1.123.291	12.527.994	37.868,92

As a result of ANN analysis, the amount of energy consumption in the building sector in 2030 was found to be 37.869 thousand TOE. As a result of the ANN analysis, it is seen that the amount of energy consumption in the building sector is gradually increasing.

5 Conclusion

Energy efficiency is a very important concept in terms of reducing environmental impacts, ensuring energy supply security, protecting existing resources and ensuring economic development, especially in energy-dependent countries such as Turkey.

In this study, the amount of energy consumption in the residential and services sectors between 2022 and 2030 was estimated with the ANN model built on MATLAB. Population, GDP and number of buildings between the years 2002-2021 and the final energy consumption in the residential and services sectors between these years were found by reviewing the necessary literatures and taught to the network.

In this modeled and tested network, population, GDP and number of buildings values generated by literature and calculations between 2022 and 2030 were processed and the final energy consumption amount in the housing and services sector between 2022 and 2030 was estimated. As a result of the estimations, the energy consumption estimate for the building sector in 2030 was found to be 37.869 thousand TOE. When these data are evaluated, it is determined that there is a regular and linear increase in the amount of consumption.

In this study, where ANN is used to forecast residential energy consumption for the year 2030, it is seen that declines and slowdowns in GDP in the dataset applied to the model directly affect net energy consumption. In 2008, the global and Turkish economic recession caused a decline in the GDP value in 2009, and by 2010, this value was only as high as the 2008 value. This decline in GDP also caused a decline in final energy consumption in 2010 compared to the year before.

Since 2015, the significant decline in GDP has also manifested itself as a decline in energy consumption amounts. It was observed that the declines in 2020 and beyond due to the Covid-19 pandemic disrupted the regular upward trend in GDP. When the data is analyzed, it is seen that there is a regular increase in population and the number of buildings, but the increase in GDP and

energy consumption is not regular, and GDP directly affects energy consumption. In case of a regular increase in GDP, energy consumption in the building sector is projected to be more than 37,868 thousand TOE in 2030.

As can be seen in the analysis, increasing population, economic indicators and the number of buildings increasing with the acceleration of transition to urban life directly affect the demand for energy. This unstoppable energy demand can be reduced to a great extent with the efficient use of energy.

Acknowledgements

This study is derived from Esra Nur İÇME's Master's Thesis titled "Analyzing Building Energy Performance Requirements in terms of Energy Efficiency".

Declaration

The authors declare that the ethics committee approval is not required for this study. There is no conflict of interest between the authors.

References

- [1] Yaşar, N. (2011). *The Perception of Energy Efficiency in Housing in the Context of Urban Energy Policies: Isparta Case*. (Master's Dissertation, Süleyman Demirel University).
- [2] İçme E.N., & Yılankırkan N. (2022, June). The Importance of Energy Efficiency in Buildings in Turkey", *International Korkut Ata Scientific Research Conference/Osmaniye*, (pp.560-561).
- [3] Önal, S. (2014). Evaluations on Energy Performance Certificates of Buildings. *European Journal of Science and Technology*, 1(3),(pp.100-105)
- [4] National Energy Efficiency Action Plan 2017-2023. (2018). *Official Gazette, Issue, 30289*, (pp.1-3).
- [5] Kurt, M. (2012). *Comparison of Turkey and Germany Building Energy Performance Regulations in terms of Reference Building and Boundary Conditions*. (Master's Dissertation, Istanbul Technical University)
- [6] Yigit, K. (2013). Energy Identity Certificate Application in Houses with Bep-Tr Software and Determination of Saving Potential of Energy Consumed for Lighting. (*Yıldız Technical University*).

- [7] Ertosun Yıldız, M., Beyhan F., & Uçar, M. K. (2021, October). Prediction of Heating- Cooling Load By Artificial Neural Networks for Energy Efficient Building Design. *9th International Symposium on Innovative Technologies in Engineering and Science/Sakarya*, (pp. 91-100).
- [8] Canbay, P., & Taş, H. (2022). Prediction of Heating and Cooling Loads of Buildings by Artificial Intelligence. *International Journal of Pure and Applied Sciences*, 8(2), (pp. 478-489).
- [9] Turhan, C., Gökçen, G., & Kazanasmaz, T. (2013), "Estimation of Total Energy Consumption of Multi-storey Buildings in Izmir with Artificial Neural Networks. *Tesisat Engineering*, Issue 134, (pp.61-68).
- [10] Şencan D., & Şencan Şahin A. (2022) Estimation of Net Energy Consumption for Turkey Based on Economic Factors. *Al-Jazari Journal of Science and Engineering*, 9(3), (pp.1101-1111).
- [11] Ekinci F., (2019). Comparison of Energy Consumption Forecasting Methods Based on ANN and ANFIS Techniques. *Düzce University Journal of Science and Technology* 7, (pp.1029-1044).
- [12] Ülkü H., & Yalpir Ş., (2021). Developing a methodology for energy demand forecasting: The case of Turkey in 2030. *Niğde Ömer Halisdemir University Journal of Engineering Sciences* 10(1),(pp.188-201).
- [13] Yılankırkan N., & Doğan H., (2020). Turkey's Energy Outlook and Primary Energy Supply Projection for 2023", *Batman University Journal of Life Sciences*, 10(2), (pp.77-92).
- [14] Aktaş C. B., (2019). Ulusal Enerji Tüketiminin Değerlendirmesi ve İstatistiksel Tahmini. *Bitlis Eren Üniversitesi Fen Bilimleri Dergisi*, 8 (4), (pp.1422-1431).
- [15] National energy balance tables (2000-2021). Retrieved 15 March, 2023, from <https://enerji.gov.tr/eigm-raporlari>
- [16] Turkish Statistical Institute, Building Permit Statistics, Retrieved 14 April, 2023, from <https://data.tuik.gov.tr/Bulten/Index?p=Building-Permits-Quarter-I-January-March,-2023-49528#:~:text=Toplam%20y%C3%BCz%C3%B6l%C3%A7%C3%BCm%C3%BCn%20%53%2C0',ortak%20kullan%C4%B1m%20alan%C4%B1%20olarak%20ger%C3%A7ekle%C5%9Fi>
- [17] International Energy Agency, Retrieved 14 May, 2023, from <https://www.iea.org/countries/turkiye>
- [18] Çakmanus, İ. (2021). Energy Efficiency and Sustainability in Buildings, Retrieved 13 April, 2023, from <https://www.mmo.org.tr/sites/default/files/users/zeynep/1.%20BIBALARDA%20SURDURULEBİLİRLİK-mmo%20sunum%2013%2002%202021.pdf>
- [19] International Monetary Fund, Retrieved 29 May, 2023, from <https://www.imf.org/en/Publications/WEO/weo-database/2022/April/weo-report?c=186,&s=NGDPD,LP,&sy=1990&ey=2027&ssm=0&scsm=1&sc=0&ssd=1&ssc=0&sic=0&sort=country&ds=.&br=1>
- [20] Uğur, A., & Kınacı, A. C. (2006, December). Classification of Web Pages Using Artificial Intelligence Techniques and Artificial Neural Networks", *inet-tr'06 - XI. "Internet in Turkey" Conference/Ankara* (pp.345-349)
- [21] Ataseven B., (2013), "Forecasting Modeling with Artificial Neural Networks", *Journal of Suggestion*, 10(39), (pp.101-115).
- [22] Data Science School, Retrieved 30 October, 2023, from <https://www.veribilimiokulu.com/basit-dogrusal-regresyon/>
- [23] Turkish Statistical Institute, Population by Scenarios, (2018-2080), Retrieved 12 May, 2023, from <https://data.tuik.gov.tr/Bulten/Index?p=Nufus-Projeksiyonlari-2018-2080-30567#:~:text=N%C3%BCfusumuz%202069%20y%C4%B1n%C4%B1na%20kadar%20artarak,100%20bin%20904%20ki%C5%9Fi%20olacakt%C4%B1r>



A REGRESSION MODEL FOR FINDING OPTIMAL SOLAR PANEL INCLINATION ANGLES

Mehmet Ali Kallioğlu* 

¹Besiri OSB Vocational School, Batman University, 72060, Batman, Turkey

Abstract

Original scientific paper

Energy efficiency is at the top of the measures created against the ever-increasing energy need for supply. Moreover, the global climate crisis, the protection of the environment, and the improvement of the economy are only possible by optimizing active energy systems. For this purpose, it is a requirement that the solar panels have the appropriate tilt angles and correct positions in order to maximize the efficiency of solar energy systems. In this study, for the province of Van (43°38' N-38°50' E), whose solar energy potential is higher than the average of Turkey, the optimum solar panel angle according to the months of the year was determined for the south-facing solar panels. It has been determined that the annual panel inclination angle is 30.54° and in the case of monthly change of panel angles, the annual yield increases up to 14% compared to the horizontal plane, reaching an average annual radiation value of 5090 Wh/m²-day. 8 different mathematical models have been developed from 4 different variables for estimating the optimum angle value specific to the latitude of the region. The statistical coefficient of certainty (R²) range of these models varies between 0.9068 and 0.9964. As a result of these findings, the regression model, whose applicability and reliability have been proven, can serve as examples of locations at different coordinates in the same latitude. Furthermore, the results set an example for academics and industrialists in terms of the proposed model's engineering design, eco-energy analysis, and use in optimal design processes.

Keywords: Optimization, solar energy, PV panels, tilt angle, energy.

OPTİMAL GÜNEŞ PANELİ EĞİM AÇILARINI BULMAK İÇİN BİR REGRESYON MODELİ

Özet

Orijinal bilimsel makale

Artan enerji ihtiyacı arzına karşı oluşturulan önlemlerin en başında enerji verimliliği gelmektedir. Dahası küresel iklim krizi, çevrenin korunması ve ekonomik kazancın iyileştirilmesi de ancak aktif enerjili sistemlerin optimize edilmesiyle mümkün olmaktadır. Bu amaçla, güneş enerjili sistemlerin verimini en üst düzeye çıkarılmasında güneş panellerinin uygun eğim açlarına ve doğru konumlara sahip olması bir gerekliliktir. Bu çalışmada güneş enerjisi potansiyeli Türkiye ortalamasının üstündeki Van ili (43°38' E-38°50' N) için aylara göre optimum panel açısı güney konumuna bakan yöne göre belirlenmiştir. Yıllık panel eğim açısı 30.540 olduğu tespit edilmiş ve panel açılarının aylık değişimi durumunda yıllık verim yatay düzleme göre %14 'e kadar artarak yıllık ortalama 5090 Wh/m²-day ışınım değerine ulaşmaktadır. Bölgenin sahip olduğu enleme özgü optimum açı değerinin tahmine yönelik 4 farklı değişkenden 8 farklı matematiksel model geliştirilmiştir. Bu modellerin istatistiksel olarak belirlilik katsayısı (R²) aralığı 0.9068 ile 0.9964 aralığında değişkenlik göstermektedir. Bu bulgular neticesinde uygulanabilirliğini ve güvenilirliğini kanıtlanan regresyon modeli aynı enlemdeki farklı koordinatlardaki konumlara örnek teşkil edebilir. Ayrıca sonuçlar, önerilen modelin mühendislik tasarımı, eko-enerji analizi ve optimum tasarım süreçlerinde kullanım açısından akademik ve sanayicilere örnek teşkil etmektedir.

Anahtar Kelimeler: Optimizasyon, güneş enerjisi, PV paneller, eğim açısı, enerji.

1 Introduction

Throughout the year, due to the Earth's movement within the solar system and its rotation around its axis, the angle at which the sun's rays fall at any point constantly changes. Data used in solar applications are typically calculated based on radiation data hitting a perfectly flat plane. To make the most effective use of solar energy, the tilt angles of the solar panels must be accurately

determined. This is especially important in areas with varied weather patterns, as the position of the panels must be adjusted to best capture the available light. Calculations of the tilt angles must be precise in order to ensure maximum energy absorption. In regions where local weather conditions differ greatly, sophisticated software is used to calculate the optimal tilt angles for the solar panels. Accurate information is critical for achieving a higher return on investment in solar energy technology.

*Corresponding author.

E-mail address: mehmetalikallioğlu@batman.edu.tr (M. A. Kallioğlu)

Received 01 October 2023; Received in revised form 30 November 2023; Accepted 11 December 2023

2587-1943 | © 2023 IJIEA. All rights reserved.

Doi: <https://doi.org/10.46460/ijiea.1369492>

The solar panel tilt angle value refers to the angle at which solar panels could be positioned in a way that maximizes their exposure to sunlight and optimizes their energy generation. The optimum tilt angle is an important factor in maximizing the efficiency of solar panels and optimizing their energy generation. Based on various factors such as solar radiation, latitude, and historical data, various studies have been carried out to develop algorithms and models for calculating the optimum angle of inclination [1–4].

One of these studies, Calabrò (2013), proposed an algorithm for determining the optimum angle of inclination of a solar panel, based on data on solar radiation in the horizontal plane. With this algorithm, by the inclination and orientation of the panel, the theoretical maximum energy generation value is determined. In the study, a linear regression correlation was found between the optimum angle of inclination and latitude. However, he noted that the standard error of mean values increased significantly with latitude, but was unreliable at high latitudes [5]. Soulayman et. al. (2016) presented a set of algorithms for determining the optimum angle of inclination and azimuth angle [(43.45°S, 66.45°S) & (43.45°N, 66.45°N)] over the mid-latitude regions at the North and South poles. Thus, he developed a mathematical model to estimate solar radiation on an oblique surface and to determine the optimum angle of inclination and orientation for the solar collector at any latitude [6]. Kallioğlu et. al. (2020) examined the empirical calculation of the optimal tilt angle for solar collectors in the northern hemisphere. In this study, primarily for three sample provinces (Antalya, Kayseri, and Trabzon) and then for the Northern Hemisphere, the optimum solar panel angle value was determined according to the months [7]. Sharma et. al., 2021, calculated the optimum tilt angles for different months to maximize solar radiation in the solar collector in the Western Himalayan (L 31° 42' N) region. In addition, correlation models for the optimal tilt angle specific to the region have been derived [8]. Nassar et. al. (2023) re-analyzed the optimum tilt angle values for 24 different locations in Libya, according to variable albedo values. He states that the correlations created with the data obtained in the study can be used throughout the whole country of Libya [9].

As can be seen from the literature summary, by measuring the radiation coming to the inclined surfaces, the maximum radiation value can be reached by determining the optimum angle.

As a result, monthly, seasonal, and annual optimum panel tilt angles for solar energy applications have been determined or correlative connections have been developed according to regions. This study was conducted with the selection of Van Province (Turkey) as the target area, given that it has a solar energy potential that surpasses the average of Turkey [10]. The purpose of this study was to ensure that the investments in solar energy made in the region were as effective and profitable as possible. By researching the current state of the solar energy sector in the region, the study aimed to identify the most suitable and efficient ways to take advantage of the benefits this renewable energy source can provide. With the right implementation strategy, investments in solar energy can prove to be highly beneficial for all stakeholders involved. The findings of the study can be used to maximize the efficiency of investments in the solar energy sector and to ensure maximum profitability in the long run. In addition, we aimed to create a sustainable model by applying the results calculated with the mathematical equations developed specifically to the region and statistical error tests. In addition, the results are intended to be an exemplary roadmap for the proposed model to be used in engineering design, eco-energy analysis, and optimal design processes.

2 Material and Method

The solar radiation values falling on the PV panels vary according to the tilt angle of the panel compared to full flat (horizontal). In practice, analyses are often carried out with data received from the horizontal plane ($\beta=00$) at a given position, while light components falling on an inclined surface are not measured. Getting maximum efficiency from solar panels is possible by positioning them at optimum angles in monthly, annual, and even seasonal intervals. This optimum value varies according to the latitude, the terrain conditions surrounding the panel, the geometry of the solar rays, the movements of the earth on its axis and its orbit around the sun, and the clearness index [11]. In this study, the province of Van (Turkey), located in the temperate zone at coordinates 38°50' N-43°38' E and with an altitude of 1661 m, was analyzed. The average annual temperature of the province is 9.5 (°C), the annual sunshine time is 7.9 hours and the average annual solar radiation value coming to the horizontal plane is 4482 Wh / m²-day [12]. According to the international climate classification Koppen, the Van region is characterized as "Dsa" Mediterranean-influenced, hot-summer, humid continental climate.

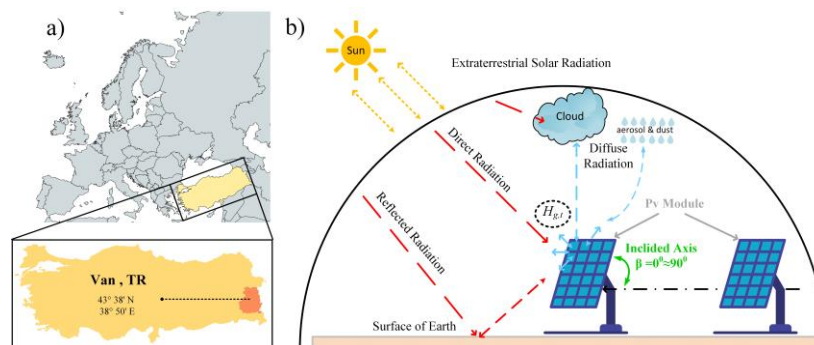


Figure 1. a) The location of the studied area b) Calculation of the optimal angle of inclination.

The monthly, mean daily global irradiance value (H_T) falling on an inclined plane can be calculated using Equation 1. This equation takes into account the latitude, declination, hour angle, sky clearness factor, and tilt angle of the inclined plane, allowing for a precise determination of the irradiance value. The sky clearness factor is especially important, as it accounts for any attenuation of solar radiation due to clouds, haze, dust, or other factors, which can vary significantly depending on the geographic region. With this equation, engineers and scientists can accurately measure the amount of solar radiation energy exposure on any given inclined plane, providing an important tool for understanding and harnessing the power of the sun. This equation consists of the sum of the values of direct solar radiation (H_{Beam}), reflected radiation ($H_{Reflected}$), and scattered radiation ($H_{Scatter}$). In addition, at variable panel tilt angles, it receives different radiant values [13].

$$H_{Total} = H_{Beam} + H_{Reflected} + H_{Scatter} \quad (1)$$

In order to estimate the solar radiation falling on the panel, various mathematical models were used and in this study, the isentropic open scattering model, which is one of the widely used and easily applied models in the literature, was used [14]. Setting off from equation 1, Equation (2), (3), (4), (5), (6), (7), (8), (9), (10), (11), (12), [15].

$$H_B = (H - H_d)R_b \quad (2)$$

$$R_b = \frac{\cos(\theta - \beta) \cos(\delta) \sin(\omega'_s) + \omega'_s \left(\frac{\pi}{180}\right) \sin(\theta - \beta) \sin(\delta)}{\cos(\theta) \cos(\delta) \sin(\omega_s) + \omega_s \left(\frac{\pi}{180}\right) \sin(\theta) \sin(\delta)} \quad (3)$$

$$H_R = \frac{H \rho (1 - \cos \beta)}{2} \quad (4)$$

$$H_S = H_d R_d \quad (5)$$

$$H_d = H \left(1 - 1,13 \frac{H}{H_o}\right) \quad (6)$$

$$H_o = \left(\frac{24}{\pi}\right) G_{sc} k \left[\cos \theta \cos \delta \sin \omega_s + \left(\frac{\pi}{180}\right) \sin \theta \sin \delta \omega_s \right] \quad (7)$$

$$k = 1 + 0,033 \cos \left(360 \frac{n}{360}\right) \quad (8)$$

$$\delta = 23,45^\circ \sin \left(360 \frac{n + 284}{365}\right) \quad (9)$$

$$\omega_s = \cos^{-1}(-\tan \theta \cdot \tan \delta) \quad (10)$$

$$\omega'_s = \min \left[\omega = \cos^{-1}(-\tan \theta \tan \delta), \cos^{-1}(-\tan(\theta - \beta) \tan \delta) \right] \quad (11)$$

$$R_d = \left(1 + \frac{\cos \beta}{2}\right) \quad (12)$$

The general solar angle calculation equations used in calculating the incoming solar radiation on the inclined

surface are shown. The Diffuse radiation calculation used in Equation 2 and Equation 5 is the amount of diffuse radiation in the horizontal plane in Equation 6. In this equation, the amount of radiation emitted from the sky is assumed to be uniform and is an isotropic model [13,16,17]. The albedo value in Equation 4 is taken as 0.2 (soil).

3 Result

3.1 Calculation of the Optimal Panel Tilt Angle

In this study, the measured meteorological data of the Electrical Works Survey Administration (EIE 1991-2020) of the General Directorate of State Meteorological Affairs were used [18]. In the calculations, the optimum point was determined from the total solar radiation values at different angles (0^0-90^0) of the solar panel, utilizing Equation 1-12.

Table 1. Calculation results of Van Province.

Months	H ₀	H	H _d	K _T	β _{OPT} (⁰)	H _T
Jan.	5113	1910	1104	0.37	56	2852
Feb.	6459	2840	1429	0.44	48	3727
Mar.	8162	4140	1767	0.51	37	4863
Apr.	9904	5130	2127	0.52	20	5351
May	11116	6630	2162	0.60	6	6652
Jun.	11603	6990	2232	0.60	0	6990
Jul.	11338	7160	2051	0.63	1	7160
Aug.	10346	6050	2052	0.58	16	6213
Sep.	8767	5250	1697	0.60	33	5978
Oct.	6941	3640	1483	0.52	50	5118
Nov.	5419	2310	1197	0.43	56	3487
Dec.	4735	1730	1016	0.37	59	2698

Table 1. shows the values belonging to the province of Van. In this chart, H is the average monthly irradiance amount falling on the horizontal plane (Wh/m²-day), H₀ is the average non-atmospheric monthly irradiance (Wh/m²-day), H_d is the monthly average diffuse radiation falling on the horizontal plane (Wh/m²-day). The optimum panel tilt angle values are β_{OPT}(⁰) and the amount of radiation falling on the corresponding panel at this angle value is H_T (Wh/m²-day). These values are shown monthly.

When Chart 1 is analyzed, the optimum angle values and the maximum and minimum points of radiation falling on the panel are 0⁰ and 6680 (Wh/m²-day) in June and 59⁰ and 2698 (Wh/m²-day) in December, respectively.

Upon examination of the region as a whole, it has been determined that the optimal angle values range from 0⁰ to 59⁰. It has been observed that the highest angle values occur in December and January, whereas the lowest angle values are observed in June and July. Furthermore, it has been noted that the angle values decrease from December to June and increase from June to December. This phenomenon can be attributed to the fact that on June 21st, the sun's rays hit the Northern Hemisphere perpendicularly, and on December 21st, they hit the Northern Hemisphere at the greatest angle. This can be further clarified by the counter graph presented in Figure 2.

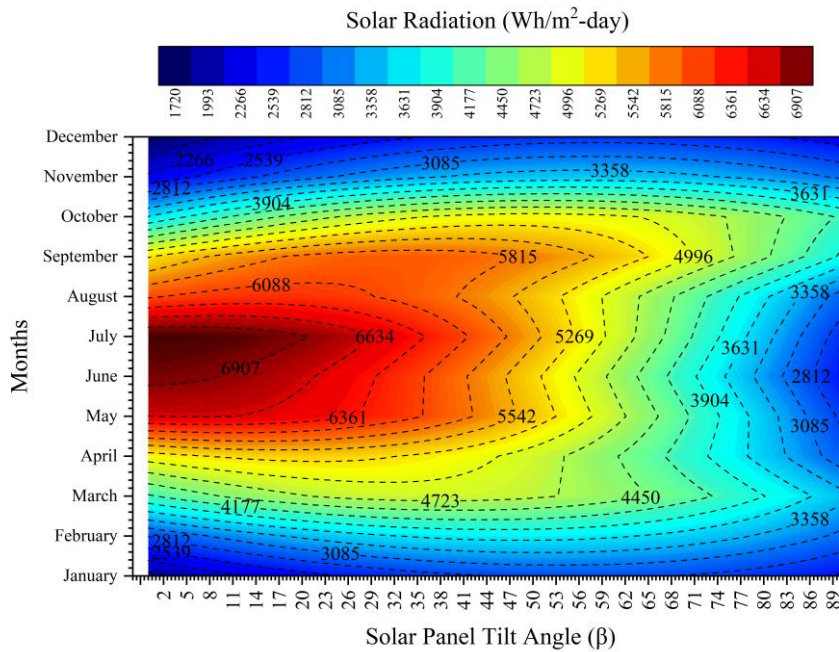


Figure 2. The change of tilt angle-radiation correlation according to months.

3.2 Optimum Angle Prediction Modelling

The developed models specific to the regions where the calculation was performed are shown in Figure 3. In these models, 8 different equations have been developed for finding the optimal tilt angle. In the developed correlational expressions, correlation models were formed with the variables of declination angle (δ), extraterrestrial radiation (H_0), solar radiation coming from the horizontal

plane (H), and diffuse radiation (H_d). The models developed specifically for Van (TR) province are given in the form of 13-20. To evaluate the performance of the developed forecasting models, there are many statistical test methods. The most common among these are; determinacy coefficient (R^2), mean deviation error (MBE), square root error (RMSE), and t-test method (t-stat) [7].

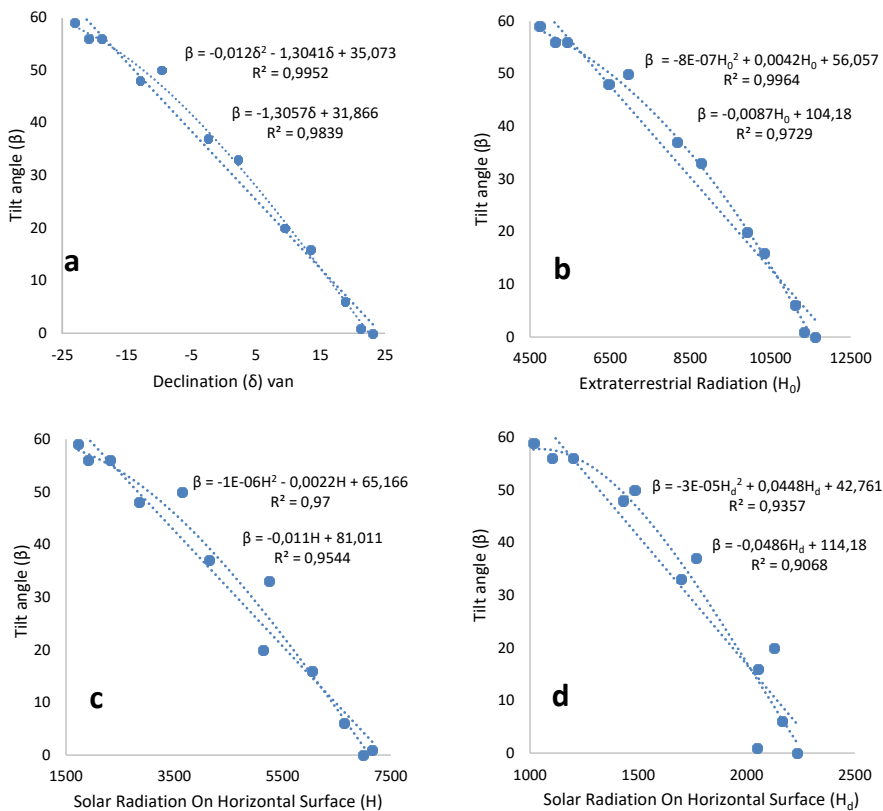


Figure 3. Models specifically designed for Van have been developed. a) δ b) H_0 c) H d) H_d

An in-depth analysis of the correlation between the estimated results of the models developed specifically for the Van region and the calculated values was conducted using various statistical methods. The results of this analysis revealed a strong correlation between the two sets of values, indicating that the models developed were accurate in predicting the outcomes of the region. Furthermore, the models were able to explain any discrepancies between the estimated values and the calculated values, thereby providing further evidence that the models were effective in their predictions. Ultimately, these findings conclusively demonstrate the effectiveness of the models developed for the Van region. A total of 12 models were developed consisting of linear and 2nd-order polynomial correlations. The panel angle of these correlations was the 2nd-degree polynomial, with the best equality in the estimate being 16.

$$\beta = -1.3057(\delta) + 31.866 \tag{13}$$

$$\beta = -0.012(\delta)^2 - 1.3041(\delta) + 35.073 \tag{14}$$

$$\beta = -0.0087(H_0) + 104.18 \tag{15}$$

$$\beta = -0.0000008(H_0)^2 + 0.0042(H_0) + 56.057 \tag{16}$$

$$\beta = -0.011(H) + 81.011 \tag{17}$$

$$\beta = -0.000001(H)^2 - 0.0022(H) + 65.166 \tag{18}$$

$$\beta = -0.0486(Hd) + 114.18 \tag{19}$$

$$\beta = -0.00003(Hd)^2 + 0.0448(Hd) + 42.761 \tag{20}$$

Table 2. Monthly inclination angle values are estimated with the developed equations.

	Equations							
	13	14	15	16	17	18	19	20
Jan.	59	57	60	57	60	57	61	56
Feb.	49	50	48	50	50	51	45	46
Mar.	35	38	33	37	35	39	28	28
Apr.	20	22	18	19	25	28	11	2
May	7	6	7	4	8	7	9	-1
Jun.	2	-1	3	-3	4	1	6	-7
Jul.	4	2	6	1	2	-2	15	8
Aug.	14	15	14	14	14	15	14	8
Sep.	29	32	28	31	23	26	32	32
Oct.	44	46	44	47	41	44	42	43
Nov.	57	55	57	55	56	55	56	53
Dec.	62	59	63	58	62	58	65	57

The coefficient of determination with which the statistical analyses were examined, the best (R²) values, the declination angle (δ) solar radiation from outside the atmosphere (H₀), solar radiation from the horizontal plane (H), and diffuse radiation from the horizontal plane, were respectively, 0.9952, 0.9964, 0.9700 and 0.9356, which are reasonably close to the number "1". In addition to being simple and usable, the location-specific models developed are also powerful in providing statistics. Thus, it is possible to determine the optimum panel angle thanks to meteorological data in cases where it is needed.

Table 3. Statistical analysis of the developed mathematical equations.

Equations	MBE	RMSE	t-statistic	R ²
13	-0.0002	2.7293	0.0003	0.9839
14	-0.0056	1.4872	0.0124	0.9952
15	0.0826	3.5379	0.0774	0.9729
16	1.0220	1.7546	2.3765	0.9964
17	0.1207	4.5928	0.0872	0.9544
18	0.2767	3.7418	0.2459	0.9700
19	-0.0652	6.5647	0.0329	0.9068
20	4.5315	7.3837	2.5781	0.9356

4 Conclusion

The best inclination angle of PV solar modules and solar collectors has been determined to maximize the efficiency of solar energy systems. In this study, Van province, which has a high solar energy investment potential in the eastern Anatolia region of Turkey, was preferred. Thus, reducing energy generation costs will increase the chances of competitiveness with other energy alternatives. However, the forms used to determine the optimal tilt angle in the current literature are either not accurate or require complex calculations. Therefore, this study proposed a new formula to determine the appropriate tilt angle of solar panels for Van province of Turkey and the optimal angle has been determined.

- When the regions were examined in general, the angles of inclination varied according to the months, with the lowest being 0° and the highest being around 59° degrees.
- The optimum fixed panel angle was measured at 31.83° per year, 54.33° in Winter, 21.00° in Spring, 5.66° in Summer, and 46.33° in Autumn.
- The yield that can be obtained with the optimum monthly panel angle change varies between 0% and 55.95%. At constant annual value, a yield increase of 13.59% was achieved.
- The highest performance of the developed models was obtained from Equation 16 and its prediction capacity is significantly high.
- All proposed correlations have shown that it can efficiently calculate the optimal tilt angle with high accuracy and therefore can be used safely.
- The data collected from calculations done in a region at latitude (38 N° ± 3°) can be extended to other locations with similar latitudes. Considering the same geographical characteristics, the data can be extrapolated and applied in other areas in the same latitude range. As a result, the region in question can serve as a model for predicting results in similar locations, thus providing valuable insight into the environment of the region.
- Specifically, these regions are comprised of Tabriz in Iranian, Lisboa in Portugal, Napoli in Italy, Athens in Greece, Algiers in Algeria, Los Angeles in the USA, Tashkent in Uzbekistan, Baku in Azerbaijan, Tunis in Tunisia, and Tianjin in China.

Upon analyzing the results, it is evident that by adjusting the panel tilt angles to the value of each month, it is possible to maximize the benefits of solar radiation. This method of optimization takes into account the seasonal fluctuations of the sun's position in the sky and ensures that the solar panels are positioned in the most effective way to absorb as much energy as possible. With this strategy in place, solar energy can be utilized more efficiently and effectively. By maximizing the efficiency of solar energy usage, the cost of production and consumption can be reduced, while also helping to protect the environment. Therefore, it is clear that adjusting panel tilt angles to the value of each month is a beneficial strategy for those looking to make the most of solar energy. In situations where monthly angle adjustment is not an option, it is beneficial to rearrange the system annually or seasonally, at a fixed angle, depending on the purpose of the system. This will allow for the best possible use of the available solar radiation. This adjustment should be done carefully, taking into consideration the local weather patterns and the desired output of the system. By doing this, the solar energy system can be optimized for the most efficient use of energy. For example, if a system is to be installed for a seasonal business that needs to operate with maximum efficiency in the spring or autumn seasons, it is expected that calculating the slope angle accordingly will provide serious economic benefit and efficiency for the particular business in question.

Declaration

The authors declare that the ethics committee approval is not required for this study.

References

- [1] Awasthi, A., Kallioğlu, M. A., Sharma, A., Mohan, A., Chauhan, R., & Singh, T. (2022). Solar collector tilt angle optimization for solar power plant setup-able sites at Western Himalaya and correlation formulation. *Journal of Thermal Analysis and Calorimetry*, 147(20), 11417-11431.
- [2] Modarresi, J., & Hosseinnia, H. (2023). Worldwide daily optimum tilt angle model to obtain maximum solar energy. *IETE Journal of Research*, 69(1), 549-557.
- [3] Abdelaal, A. K., & El-Fergany, A. (2023). Estimation of optimal tilt angles for photovoltaic panels in Egypt with experimental verifications. *Scientific Reports*, 13(1), 3268.
- [4] Gunerhan, H., & Hepbasli, A. (2007). Determination of the optimum tilt angle of solar collectors for building applications. *Building and Environment*, 42(2), 779-783.
- [5] Calabrò, E. (2013). An algorithm to determine the optimum tilt angle of a solar panel from global horizontal solar radiation. *Journal of Renewable Energy*, 2013.
- [6] Soulayman, S. (2016). Optimum Tilt Angle and Maximum Possible Solar Energy Gain at High Latitude Zone. *Journal of Solar Energy Research*, 1(2), 25-35.
- [7] Kallioğlu, M. A., Durmuş, A., Karakaya, H., & Yılmaz, A. (2020). Empirical calculation of the optimal tilt angle for solar collectors in northern hemisphere. *Energy Sources, Part A: Recovery, Utilization, and Environmental Effects*, 42(11), 1335-1358.
- [8] Sharma, A., Kallioğlu, M. A., Awasthi, A., Chauhan, R., Fekete, G., & Singh, T. (2021). Correlation formulation for optimum tilt angle for maximizing the solar radiation on solar collector in the Western Himalayan region. *Case Studies in Thermal Engineering*, 26, 101185.
- [9] Nassar, Y. F., El-Khozondar, H. J., Abouhmod, N. M., Abubaker, A. A., Ahmed, A. A., Alsharif, A., ... & El-Khozondar, R. J. (2023, May). Regression model for optimum solar collectors' tilt angles in Libya. In *2023 8th International Engineering Conference on Renewable Energy & Sustainability (ieCRES)* (pp. 1-6). IEEE.
- [10] Uçkan, İ. (2018). Analysis of solar radiation data in van, turkey. *Celal Bayar University Journal of Science*, 14(4), 421-427.
- [11] Yadav, A. K., & Chandel, S. S. (2013). Tilt angle optimization to maximize incident solar radiation: A review. *Renewable and Sustainable Energy Reviews*, 23, 503-513.
- [12] Kottek, M., Grieser, J., Beck, C., Rudolf, B., & Rubel, F. (2006). World map of the Köppen-Geiger climate classification updated.
- [13] Muneer, T., & Saluja, G. S. (1985). A brief review of models for computing solar radiation on inclined surfaces. *Energy conversion and management*, 25(4), 443-458.
- [14] Liu, B. Y., & Jordan, R. C. (1960). The interrelationship and characteristic distribution of direct, diffuse and total solar radiation. *Solar energy*, 4(3), 1-19.
- [15] Duffie, J. A., Beckman, W. A., & Blair, N. (2020). *Solar engineering of thermal processes, photovoltaics and wind*. John Wiley & Sons.
- [16] Muneer, T. (2007). *Solar radiation and daylight models*. Routledge.
- [17] Cooper, P. I. (1969). The absorption of radiation in solar stills. *Solar energy*, 12(3), 333-346.
- [18] Turkish State Meteorological Service Official Web Sites (n.d.). Retrieved August 08,22 from <https://www.mgm.gov.tr/eng/forecast-cities.aspx>



RESEARCHING THE PRODUCTION FEATURES OF SURGICAL INSTRUMENT MANUFACTURING WITH 3D PRINTING

Fatma Nazlı Özsolak*¹ 

¹Erciyes University, Industrial Design Engineering department, Kayseri, Turkey

Abstract

Original scientific paper

The process of 3D printing begins with creating a digital 3D model of the object to be printed using CAD software. This model is then sliced into thin cross-sectional layers, which are used as a guide for the 3D printer to deposit material layer by layer. The printer follows the instructions from the digital model and adds material, typically plastic, metal, or composite, to build up the final 3D object. One of the key advantages of 3D printing is its ability to produce complex geometries that are difficult or impossible to achieve with traditional manufacturing methods. This allows for the creation of lightweight and optimized designs, reducing material waste and improving the overall performance of the finished product.

This study investigates the feasibility of SLA technology (Stereolithography) as a production method as a practical alternative for surgical instrument manufacturing. Although there are many studies on obtaining accurate prints with SLA 3D device, research on the production of surgical instruments is insufficient. For this purpose, an experimental study was conducted using an SLA type 3D printer, examining the hardware and software components in terms of print quality. First, the same size prints were taken of the tools whose geometries were scanned with a 3D scanner.

The purpose of this article is to conduct detailed research on the feasibility of lower-cost, 3D printing technology in surgical instrument manufacturing. An application was made and shared regarding the use of printed tools in artificial leather working sets.

Keywords: 3D Printers, surgical instrument, stereolithographic printing (SLA), 3D scanner, additive manufacturing.

CERRAHİ ALET İMALATININ 3 BOYUTLU YAZICI İLE ÜRETİM ÖZELLİKLERİNİN ARAŞTIRILMASI

Özet

Orijinal bilimsel makale

Eklenebilir imalat olarak da bilinen üç boyutlu (3D) baskı, malzemelerin katman katman üst üste bindirildiği katmanlı üretim prensibine dayanmaktadır. Bu teknoloji, bilgisayar destekli tasarım (CAD) modeline göre katı modelleme kullanarak malzemeyi doğru bir şekilde biriktirerek herhangi bir karmaşık şekle sahip bileşenleri hızlı bir şekilde üretmek için kullanılabilir.

Bu çalışmada cerrahi alet imalatı için, pratik bir alternatif 3 boyutlu olarak SLA (Sterolitografi) ile teknolojisinin uygulanabilirliğini üretim yöntemi olarak araştırmaktadır. SLA 3D cihazlarıyla doğru baskıların elde edilmesi üzerine birçok çalışma olmasına rağmen, cerrahi aletlerin üretimi hakkında yapılan araştırmalar yetersizdir. Bu amaçla SLA tipi 3D yazıcı kullanarak baskı kalitesi açısından donanım ve yazılım bileşenleri incelenen deneysel bir çalışma yapılmıştır. Öncelikle 3 boyutlu tarayıcı ile geometrileri taranan aletlerin aynı boyutta baskıları alınmıştır.

Bu makalenin amacı, daha düşük maliyetli, 3 boyutlu baskı teknolojisinin cerrahi alet imalatında kullanılabilirliği hakkında ayrıntılı araştırma yapmaktır. Yapay deri çalışma setlerinde baskısı alınan aletlerin kullanımına ilişkin uygulama yapılarak paylaşılmıştır.

Anahtar Kelimeler: 3 Boyutlu yazıcılar, cerrahi alet, sterolitografi (SLA), 3 boyutlu tarayıcı, eklemeli imalat.

1 Introduction

In the developing world, the supply of special-purpose treatment or medical supplies to hospitals and clinics is in some cases very affected by global supply chain fluctuations. While the COVID-19 pandemic has exposed weaknesses in medical supply chains around the

world, underdeveloped regions have been disproportionately affected for a variety of reasons [1–3]. The possibility of producing medical equipment locally and reliably sterilizing it can reduce this risk. 3D printing of surgical instruments and medical devices is a possible solution to this problem [4]. In their research, Francis et al printed surgical instruments from various materials. As a

*Corresponding author.

E-mail address: fnsari@erciyes.edu.tr (F. N. Özsolak)

Received 31 October 2023; Received in revised form 12 December 2023; Accepted 21 December 2023

2587-1943 | © 2023 IJIEA. All rights reserved.

Doi: <https://doi.org/10.46460/ijiea.1384227>

result of their study they remarked 3D printed surgical tools to develop a reliable and rapid high-level disinfection process using inexpensive and widely available methods appropriate for the austere environment [4].

The higher resolution of SLA-style 3D printing allows users to do more with 3D printing. A common application of SLA printing is prototyping medical devices that require small line pieces. Fused Deposition Modelling (FDM) type 3D printers do not have high enough resolution to print such objects at the appropriate scale. There are many other applications that will be useful from small, accurate prototypes; but until a cheap and reliable SLA printer becomes available.

This technology developed will probably only be used by well-funded projects [5].

Cingoz et al made surgical dissector modelling with the measurements taken from the patient. Polylactic acid (PLA) filament was used in the devices during the printing process. They also used it in the operation of patients diagnosed with lumbar stenosis, where surgical dissectors were sterilized and measurements were checked before surgery. They stated that there were no intraoperative complications observed during the use of 3D printed surgical dissector. [6].

Keßler et al have researched surgical implant guides. Their purpose of this in vitro study was to delineate the quality of the implant position transfer with 5-axis milled and DLP and SLA 3D-printed surgical guides. They stated that this in vitro study three-dimensional printing of resin material is appropriate for the manufacturing of surgical implant guides [7].

The study by Uddin et al. demonstrates the potential of 3D printed microneedles for enhanced delivery of anticancer drugs to skin tumors. The use of stereolithography (SLA) for fabrication and ink jetting for coating the microneedles with cisplatin formulations shows promise for in vivo transdermal delivery. The optimized printability and excellent penetration capacity of the 3D printed microneedles suggest that this approach could be a valuable tool for improving cancer treatment. Further research and development in this area could lead to more effective and targeted delivery of anticancer drugs for skin tumors [8].

The study conducted by Xu et al demonstrates the potential of SLA 3D printing technology in the development of implantable bladder drug delivery systems. By using this technology, the researchers were able to design and manufacture devices that could provide sustained release of lidocaine directly at the site of the bladder, avoiding the systemic side effects associated with traditional drug delivery methods.

The use of SLA 3D printing allowed for the precise control of drug release rates, ensuring that the lidocaine was released at a predetermined rate over a specific period of time. This could significantly improve patient compliance and treatment outcomes for bladder disorders such as overactive bladder disorder and bladder cancers.

The researchers also noted that the devices could be easily adapted for the treatment of other bladder disorders by changing the selected drug. This highlights the potential of SLA 3D printing technology in the development of personalized medical devices and

treatments, tailored to the specific needs of individual patients.

Overall, the study by Xu et al demonstrates the significant potential of SLA 3D printing in the field of medicine, particularly in the development of implantable drug delivery systems. The technology has the potential to revolutionize treatment outcomes for a range of medical conditions, providing patients with more effective and personalized treatment options [9].

In this study, 3D solid models of some currently used surgical instruments, whose geometries are known, were scanned and printed with the SLA (Stereolithography) method, one of the three-dimensional production methods. The SLA method is a preferred method in the manufacturing of detailed parts.

SLA (Stereolithography) printing is an additive manufacturing process that belongs to the category of resin-based 3D printing technologies. It was one of the first 3D printing technologies developed and is still widely used for creating highly detailed and accurate 3D objects. Figure 1 shows the 3D printing technologies.

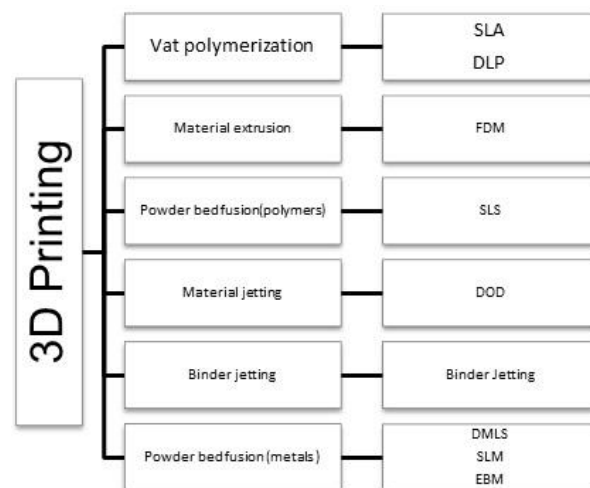


Figure 1. 3D printing Technologies [10].

In the following section, general information will be given about the manufacturing and scanning technologies used in the study process.

1.1 What is Stereolithography (SLA)?

SLA is considered one of the additive manufacturing methods. This method is a technology that uses computer-aided design (CAD) data to produce objects layer by layer using liquid polymer.

The first additive manufacturing technology developed is the SL (Stereolithography) technique, which is based on the solidification of the light-sensitive liquid resin layer with UV (Ultraviolet)-laser. In the following years, many new technologies such as FDM, SLS (Selective Laser Sintering), LOM (Laminated Object Manufacturing), Inkjet Printing (3DP) and LAM (Laser Additive Manufacturing) have emerged [11-12]. After SL technology became widespread, studies on DLP (Digital Light Processing), DPP (Daylight Polymer Printing) and Continuous Light Interphase Printing (CLIP) technologies have been concentrated based on the same production technique [13].

Pool photo polymerization (HFP), which is the general name of SL, DLP and CLIP technologies, has started to be used in the manufacturing of small quantities of plastic parts in recent years, apart from rapid prototyping and product development areas. It is preferred in prototype product manufacturing in order to shorten product development times and receive user feedback, especially in applications such as automotive, aviation, industrial design [14].

How the 3D SLA printing process works is listed as ;

- 1.Design: First, a 3D model of the object to be printed is created using computer-aided design (CAD) software.
2. Slicing: The 3D model is then sliced into thin horizontal layers using slicing software, which generates a set of 2D cross-sectional images.
3. Printing: A vat of liquid photopolymer resin is used as the printing material. A build platform is lowered into the vat just below the surface of the resin. A UV laser is then used to selectively solidify the resin by tracing each layer's cross-section based on the sliced image data. The laser moves according to the design specifications, solidifying one layer at a time. Once a layer is complete, the build platform is lowered slightly, and the process continues for the next layer. This continues until the entire object is printed, layer by layer.
4. Curing: After the object is fully printed, it is typically removed from the printer. However, the object is not yet fully cured; it remains somewhat tacky. To complete the curing process and harden the object, it is often placed under a UV light source or in a UV curing chamber.

The photopolymerization process is irreversible and there is no way to convert SLA component back to liquid form. Heating these SLA pieces will cause them to burn rather than melt. This is because materials produced by SLA are made of thermosetting polymers, unlike the thermoplastics used by fused deposition modeling (FDM) [15-17].

1.2 Advantages of 3D SLA Printing

High Precision: SLA printing can produce highly detailed and intricate objects with smooth surfaces.

Accuracy: It's known for its accuracy in replicating the design from the 3D model.

Wide Material Selection: There is a variety of resin materials available, including standard, flexible, and specialty resins for different applications.

Minimal Support Structures: SLA printers often require fewer or more easily removable support structures compared to other 3D printing methods [15-17].

1.3 Disadvantages of 3D SLA Printing

Limited Build Size: SLA printers typically have smaller build volumes compared to Fused Deposition Modeling (FDM) or other technologies.

Resin Handling: Resin-based printing can be messy, and the resin itself can be toxic, so it requires careful handling and proper ventilation.

Post-Processing: Some SLA prints may require additional curing and post-processing steps to achieve the desired final result.

Cost: SLA printers and the resins can be more expensive than some other 3D printing technologies [15-17].

1.4 Stereolithography Materials

Epoxy resins are indeed commonly used in SLA and other 3D printing processes due to their ability to produce strong and durable models with high accuracy. They are particularly suitable for fit, form, and function testing purposes.

The mention of a low heat tolerance with typical heat deflection temperatures around 110-120°F suggests that these materials may not be suitable for applications that involve exposure to high temperatures [18]. Heat deflection temperature (HDT) is a measure of a material's ability to withstand deformation under load at elevated temperatures.

2 Material and Method

2.1 CMM (Coordinate Measuring Machine)

The printed surgical instruments were scanned with an optical 3D scanner (CMM) using structured light technology.

3D scanning devices create 3D models of the surfaces of objects using laser or optical systems. These scans are transferred to a computer and converted into 3D models using software. As a result, a point cloud consisting of millions of points is created for each surface of an object [19-20].

With the developing technology, 3D data in the digital environment has gained importance as all processes such as design, product development, prototyping, simulation and quality control are now computer-aided. The data obtained by 3D scanning provides important data to designers and manufacturers in different areas such as reverse engineering and quality control.

3D scanning technology allows for the creation of highly accurate digital models of physical objects, which can then be used for a variety of purposes. In reverse engineering, 3D scanning can be used to create digital models of existing parts or products, allowing for the recreation of those items or the development of new designs based on the scanned data.

Indeed, 3D scanning has revolutionized the way we capture and replicate physical objects. The use of high-tech optical and laser scanners has significantly expedited the process, providing precise and detailed results within a short timeframe. This technology has proven to be versatile, capable of capturing objects of various colors, sizes, and complexities with exceptional clarity. As a result, 3D scanning has become an invaluable tool across numerous industries, from manufacturing and design to archaeology and healthcare.

The advancements in 3D scanning technology have indeed revolutionized the speed and precision of data acquisition. High-tech optical and laser scanners have significantly reduced the time required to capture detailed 3D data, enabling quick and accurate results regardless of

the object's color, size, visual details, or geometric complexity. This level of flexibility and efficiency has made 3D scanning an invaluable tool across various industries, from manufacturing and design to cultural preservation and medical applications. As technology continues to evolve, we can expect even greater advancements in 3D scanning, further enhancing its capabilities and applications.

While traditional engineering is the concrete manifestation of a product idea through the design and manufacturing process, reverse engineering works the exact opposite. In figure 2 scanning process is shown as below.



Figure 2.3D Scanning process.

2.2 Printing by Stereolithography (SLA)

Figure 3 shows the three-dimensional solid models obtained after scanning.

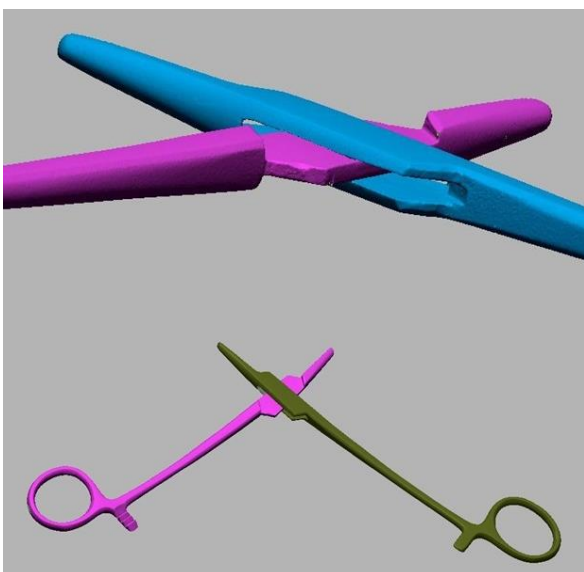


Figure 3. Solid models obtained after scanning.

CAD model created geometries were sliced with Anycubic Photon Workshop Slicer for printing.

Anycubic Photon Workshop slicer software slices the STL mesh file of the target part. This software creates an image file (like Xray imaging) for each layer. The SLA printer cures the liquid polymer in a selective area by reflecting (illuminating) the image mask. Figure 4 shows sliced images of the forceps and needle holder.

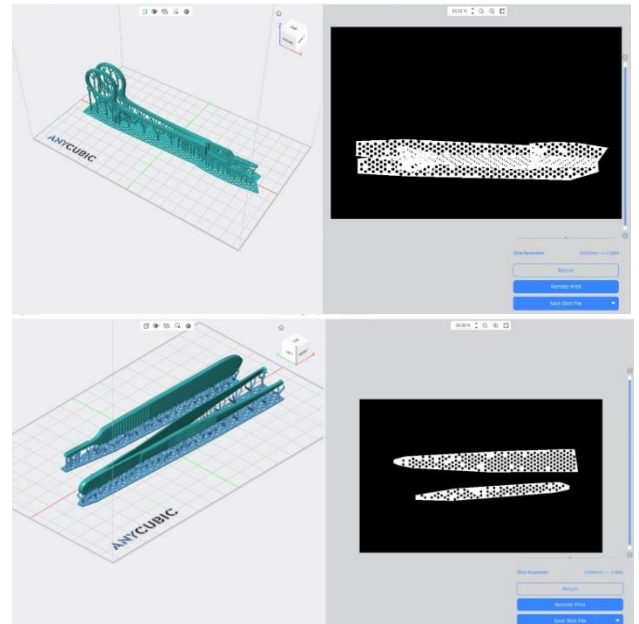


Figure 4. Sliced images of forceps and needle holder.

Figure 5 shows how solid models will be placed on the printing plate. This means the printer printed the objects in this order as shown in Figure 5.

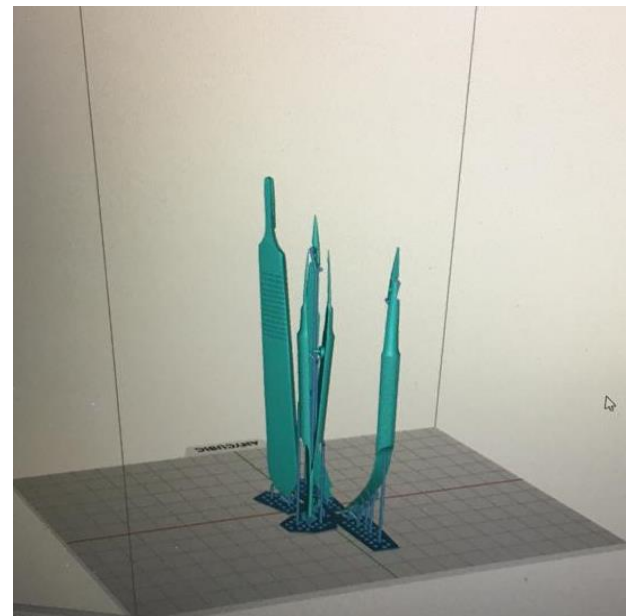


Figure 5. Planned view of solid models on the printing plate.

Printing was done with Anycubic Photon Mono X 4K Resin 3D Printer, which works with LCD-based SLA printing technology. Figure 6 shows the 3D device. Printing time was determined as 2 hours 56 minutes. Printing parameters are shown in Table 1.

Table 1. Printing Parameters

Printing Parameters	
Print volume:	192x120x245 mm
Source of light :	405 nm
XY Resolution:	0,050 mm 3840 * 2400
Z Axis Resolution:	0.01mm
Layer Resolution:	0,01 - 0,15 mm
Print Speed:	MAKS. 60 mm / hour
Strength	120W
Lighting:	Matrix
Layer curing time:	1-2 second



Figure 6. 3D printing equipment.

The printed materials were washed with alcohol and cured for 15 minutes. The curing process is shown in Figure 7.



Figure 7. Curing process.

The printed surgical instruments are shown in Figure 8. These are needle holder, forceps and scalpel handle respectively.



Figure 8. Printed surgical dressing set.

At the end of printing procedure for testing printed surgical dressing set a training suture set is used as shown in Figure 9.



Figure 9. The training suture set.

4 Results & Discussion

In this study, surgical instruments were manufactured using 3D technology, which is a method other than the traditional method. The scanning process, which is the first stage of manufacturing, was done precisely with a CMM. This is how existing geometries created the solid model. STL files were sliced with a program compatible with 3D printers and made ready for printing. Successful prints were obtained on the first try. However, the needle holder broke during the cleaning of the support parts of the printed parts. The printed parts have smooth and high-quality surfaces. Sewing application was tried on the artificial skin set with the printed tools. KVS Dr. Gülден SARI's experiences were shared. First , a suture set was used while stitching. Then, the stitching was done with a free needle. Figure 10 shows the use of a suture set and a free needle. The stitching process was performed with both types of needles.

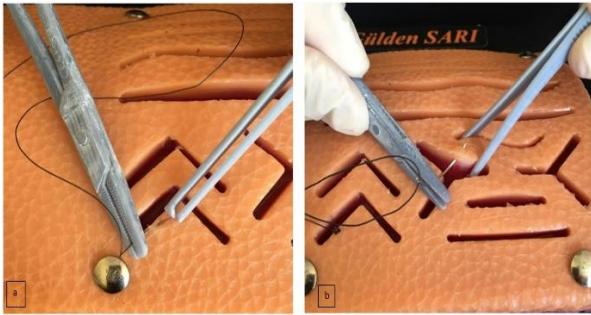


Figure 10. With the surgical dressing set printed with 3D
a) Use of the suture set b) Use of the free needle.

Figure 11 shows the stitches made with the suture set and free needle set.

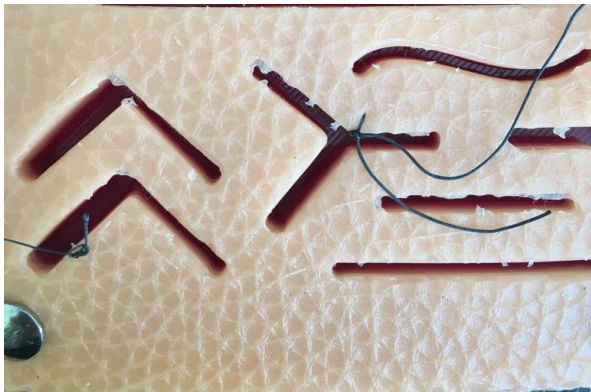


Figure 11. The stitches made with the surgical dressing set printed with 3D were made with a suture needle in the incision and a free needle in the incision.

In order to compare the stitches in terms of shape, stitches were applied with a dressing set manufactured with the traditional method. The mentioned stitches are shown in Figure 12. The stitches made with the traditionally manufactured surgical dressing set and the stitches made with the 3D printed set are shown in the figure. The stitches in the box were made with the 3D printed set.

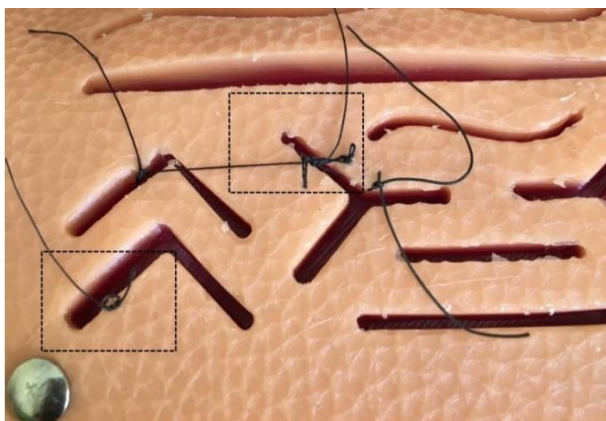


Figure 12. Stitches made with 3D and traditional set.

After the stitching process was completed, the threads were cut with a steel scalpel attached to the 3D printed scalpel handle. Figure 13 shows the thread cutting process.

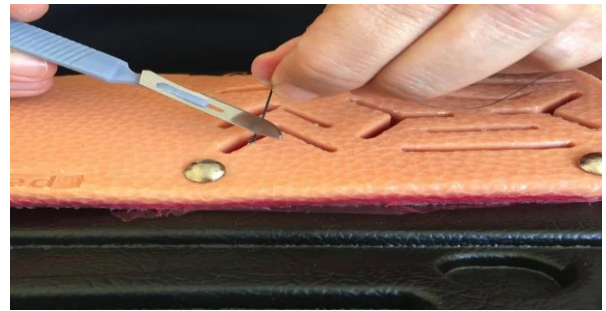


Figure 13. Cutting rope with a scalpel.

5 Conclusion

In this study, surgical instruments were manufactured using 3D technology, which is a method other than the traditional method. Stitches application was tried on the artificial leather set with the printed tools KVS Dr. Gülden SARI's experiences were shared on suturing and using instruments.

The doctor stated that 3D printed instruments are lighter than steel ones. However, she stated that it was relatively difficult to hold the thread with the needle holder. But for about forceps and scalpel handle she states that there is no difference in use depending on the steel type, but it is weaker in terms of strength.

Studies can be carried out with different methods in terms of developing three-dimensional printing technology and material diversity. There are few studies on the subject in the existing literature. Detailed studies need to be carried out to replace steel, which is the material of existing tools, and traditional manufacturing methods.

Acknowledgements

Ethics committee approval is not required. The author would like to thank Dr. Gülden Sari for her contributions. Dr. Gülden Sari works as an chief assistant in cardiovascular surgery department at Erciyes University.

Declaration

Ethics committee approval is not required.

References

- [1] U.S. Department of Health and Human Services (2021). Louissaint N. In: Review: Medical Supply Chain Responses to the COVID-19 Pandemic.; 2020. Retrieved January 2, 2022 from <https://files.asprtracie.hhs.gov/documents/2020-in-review-medical-supply-chain-responses-to-the-covid-19-pandemic.pdf>.
- [2] Bhaskar, S., Tan, J., Bogers, M. L., Minssen, T., Badaruddin, H., Israeli-Korn, S., & Chesbrough, H. (2020). At the epicenter of COVID-19—the tragic failure of the global supply chain for medical supplies. *Frontiers in public health*, 821.
- [3] New York Times (2021). Goodman PS. How the Supply Chain Upheaval Became a Life-Or-Death Threat. Retrieved 5 January, 2022. from <https://www.nytimes.com/2021/12/09/business/supply-chain-medical-device-shortages.html>.

- [4] Francis, A., Williams, J., Prey, B., Lammers, D., Vu, M., Jones, I., ... & Bingham, J. (2023). Rapid cold sterilization of 3D printed surgical instruments for the austere environment. *The American Journal of Surgery*, 225(5), 909-914.
- [5] Finnes, T. (2015). High definition 3d printing—comparing sla and fdm printing technologies. *The Journal of Undergraduate Research*, 13(1), 3.
- [6] Cingöz, İ. D., Özyörük, Ş., HÜSEMOĞLU, B., & ŞAHİN, M. C. (2019). Surgery Dissector: Surgical Device Production with 3d Print Technology. *Journal of Medical Innovation and Technology*, 1(1), 5-8.
- [7] Keßler, A., Dosch, M., Reymus, M., & Folwaczny, M. (2022). Influence of 3D-printing method, resin material, and sterilization on the accuracy of virtually designed surgical implant guides. *The Journal of Prosthetic Dentistry*, 128(2), 196-204.
- [8] Uddin, M. J., Scoutaris, N., Economidou, S. N., Giraud, C., Chowdhry, B. Z., Donnelly, R. F., & Douroumis, D. (2020). 3D printed microneedles for anticancer therapy of skin tumours. *Materials Science and Engineering: C*, 107, 110248.
- [9] Xu, X., Goyanes, A., Trenfield, S. J., Diaz-Gomez, L., Alvarez-Lorenzo, C., Gaisford, S., & Basit, A. W. (2021). Stereolithography (SLA) 3D printing of a bladder device for intravesical drug delivery. *Materials Science and Engineering: C*, 120, 111773.
- [10] Hubs 2022. Retrieved 5 January, 2022 from <https://www.hubs.com/knowledge-base/what-is-sla-3d-printing/>
- [11] T. Wohlers, & T. Gornet (2016). Wohlers Report. *Wohler Associates Inc.*, USA, 2016.
- [12] Sürmen, H. K. (2019). Eklmeli İmalat (3b Baskı): Teknolojiler ve Uygulamalar. *Uludağ Üniversitesi Mühendislik Fakültesi Dergisi*, 24(2), 373-392.
- [13] Piedra-Cascón, W., Krishnamurthy, V. R., Att, W., & Revilla-León, M. (2021). 3D printing parameters, supporting structures, slicing, and post-processing procedures of vat-polymerization additive manufacturing technologies: A narrative review. *Journal of Dentistry*, 109, 103630.
- [14] Başçı, Ü. G., & Ymanoğlu, R. (2022). Havuz Fotopolimerizasyonu (HFP) ile Eklmeli İmalat. *Düzce Üniversitesi Bilim ve Teknoloji Dergisi*, 10(2), 914-928.
- [15] Hubs (2022). Retrieved 5 January, 2022 from <https://www.hubs.com/knowledge-base/what-is-sla-3d-printing/>
- [16] Protolabs (2022). Retrieved 5 January, 2022 from <https://www.protolabs.com/engb/resources/blog/stereolithography-advantages-and-disadvantages/>
- [17] Hubs (2022). Retrieved 5 January, 2022 from <https://www.3dstereolithography.com/advantages-and-disadvantages/>
- [18] Zulfiqar Ali August (2015). Process Modeling For Projection Based Stereo Lithography, (Master's Dissertation, Bilkent University).
- [19] Robotistan (2022). Retrieved 5 February from <https://www.robotistan.com/3d-tarayici>
- [20] Infotron (2022). Retrieved 6 February, 2022 from <https://infotron.com.tr/3-boyutlu-teknolojiler/3d-tarayici>



NUMERICAL ANALYSIS OF DOUBLE GEOPOLYMER CONCRETE LAYER WITH DIFFERENT PROPERTIES

Berivan Yilmazer Polat*¹ 

¹Munzur University, Faculty of Fine Arts, Design and Architecture, Department of Architecture, Tunceli, Turkey

Abstract

Original scientific paper

Researchers have been working to find alternatives to conventionally produced concrete in recent years. Geopolymer concretes are also the focus of these studies. There are not enough studies on modelling geopolymer concretes, which are the subject of many experimental studies. In this study, the models of geopolymer concretes with different properties for two different loading and bearing conditions were solved by finite element method. In the analyses, the stress and strain conditions of the geopolymer concretes were analyzed by changing their locations. It was observed that when the geopolymer concrete with a lower modulus of elasticity and 100% slag content was on top, the stress values decreased, and the strain rates increased. The results obtained showed that the mechanical behavior of geopolymer concretes can be investigated much faster and easier with the finite element method as an alternative to experimental studies.

Keywords: Geopolymer concrete, slag, finite element method, stress, strain.

1 Introduction

Cement and the traditional concrete production process are polluting and leave much waste in the environment after use [1]. Geopolymer concretes, on the other hand, do not contain cement and, therefore, do not require the polluting cement production process. In addition, since waste products such as fly ash, blast furnace slag, silica, etc., are used in their construction, they help to dispose of these wastes. These concretes perform better than conventional concretes in terms of mechanical properties such as compressive strength, blast and impact strength [2] and are more reliable in terms of durability [3]. Geopolymer concretes are generally formed by initiating the hydration of a waste pozzolan or clay-derived matrix material with an activator such as sodium silicate or sodium hydroxide [4]. Although their Poisson ratios and densities are close, they may have different moduli of elasticity depending on their content [5]. Unlike conventional concrete, geopolymer concretes exhibit different behavioural characteristics under compressive and tensile stresses. Under compressive stress, while it initially exhibits linear elastic properties, its behaviour changes at a certain point.

Nguyen et al. [5] studied in detail the mechanical properties of heat-cured low-calcium fly ash geopolymer concrete and the behaviour of geopolymer concretes. They analysed the behaviour of the geopolymer layer using a bending test including four-point bending, elastic theory, and a finite element model. Their study observed that the measured tensile strength values of geopolymer concrete with fly ash admixture were higher than the

calculated tensile strength values of Portland cement concrete.

Ganesan et al. [6] examined the strength and behavior of steel fiber-reinforced geopolymer concrete columns using experimental and analytical methods. The test results showed that the addition of steel fibers increased the axial strength and considerably modified the stress-strain behavior and elasticity of the columns. To better understand the stress-strain behavior of the column, a finite element model of the geopolymer column was developed using Ansys software. The results obtained from the finite element method analysis were observed to be satisfactorily similar to the experimental results.

Antonyamaladhas et al. [7] compared the mechanical properties of geopolymer concrete and conventional concrete elements with layer and L-section using experimental and finite element methods. Durability properties such as acid and sulfate resistance were performed for both geopolymer concrete and conventional concrete, and the results were compared. The results of acid and sulfate resistance tests showed that the strength of geopolymer concrete was higher.

Annapurna et al. [8] conducted experimental and analytical studies on finite element analysis using Ansys software to simulate the flexural behaviour of reinforced geopolymer concrete layers. The results of the analytical investigations were in close agreement with those obtained from the experimental studies. Thus, the developed finite element model was found to be a good option for predicting the flexural behaviour of reinforced geopolymer concrete layers.

* Corresponding author.

E-mail address: bpolat@munzur.edu.tr (B. Yilmazer. Polat)

Received 28 October 2023; Received in revised form 12 December 2023; Accepted 21 December 2023

2587-1943 | © 2023 IJIEA. All rights reserved.

Doi: <https://doi.org/10.46460/ijiea.1382611>

Abdul Aleem and Arumairaj [9] compared manufactured and natural sand-reinforced geopolymer-reinforced concrete layers with Portland cement-reinforced concrete layers using analytical and finite element methods. The natural sand-reinforced geopolymer concrete layer behaved like an ordinary Portland cement-reinforced concrete layer under flexural loads. It was observed that the manufactured sandy geopolymer reinforced concrete layer gave better results than reinforced concrete layers under flexural loads.

Waryosh and Ali [10] investigated the effects on the behaviour and strength of five supported composite-cased geopolymer concrete layers under full and partial interaction (70%) static loads. They concluded that when the same specimens differed in partial and full interaction, full interaction loading resulted in higher strength capacity and less deflection.

Yilmazer Polat et al. [11] researched the basic conditions for self-healing cracks in geopolymer mortars and geopolymer mortar preparation techniques. For this purpose, the effect of cure media on geopolymer mortars, the most appropriate methods of bacterial addition to mortar without encapsulation and the effect on the compressive strength of mortar were investigated. The results of the experiments determined that the samples with bacteria added to the mortar with appropriate methods contained fewer voids than those produced without bacteria.

Aydın [12] experimentally tested the impact strength effect of composite layers formed with geopolymer concrete, which is increasingly being used and traditionally known as Portland cement concrete. As a result of the study, it was concluded that composite specimens produced with geopolymer concrete were more resistant to impact.

Venkatachalam et al. [13] analysed the flexural behaviour of geopolymer concrete layers using the three-dimensional finite element method. They reported that the compressive strength of geopolymer concrete increases as the curing time increases and that the finite element method is a good alternative to the experimental method.

Yilmazer Polat ve Uysal [14] evaluated the healing of metakaolin-based geopolymer mortar cracks without any chemical healing. Yilmazer Polat [4] also investigated the healing of early microcracks in geopolymer mortars using a carbonate-precipitating bacterial agent and expanded perlite aggregate as a carrier. In the study, he observed that bacterial cells were able to sporulate directly on the expanded perlite aggregate. Therefore, the crack healing rate of the specimens was greatly improved, visually up to 100%.

Although there are many similar in-depth and diverse studies on geopolymer concretes in the literature, the behaviour of multi-layered geopolymer concrete elements under load has yet to be investigated in detail experimentally and numerically. This study's load-unit strain and displacement relationships of concrete under compression are numerically investigated.

2 Objectives

This paper uses the finite element method to analyze the displacement and deformation behaviour of 2 different

geopolymer concrete blocks under 2 different support and loading conditions. In this way, it will be possible to compare the changes in the deformation and displacement behaviour of these geopolymer concretes with different moduli of elasticity under different types of supports and different loadings without performing experimental studies. This process, which is laborious and costly when done experimentally, is faster and less costly with the finite element method.

Geopolymer concretes are a new generation of concrete with high strength and superior physical and mechanical properties that do not require laborious and polluting cement production as they do not contain cement compared to traditional concretes. This concrete, which is also called green concrete due to its environmentally friendly properties, is a subject that has been intensively researched scientifically in recent years due to its advantages. The expected mechanical behaviour of concrete under loading is vital for achieving its intended use. Geopolymer concretes, like conventional concretes, may have many uses in the future, such as roads, barriers, dams, and foundations, and their stress and strain behaviours become important in these applications. In the literature, no study is investigating the shape and displacement behaviour of geopolymer concretes under different support and loading conditions by the finite element method. The aim of this research paper, which is a very original study in this respect, is to see the stress and displacement behaviour of two different content geopolymer concrete materials with different moduli of elasticity formed by pouring on each other.

3 Research Methodology

This study is based on the stress and strain analysis method of a system consisting of 2 different geopolymer concretes positioned on top of each other by considering 2 different support conditions and loading conditions using the ANSYS program. In the study, firstly, the geopolymer concretes under different loads were analyzed, and their behaviour in different axes were examined. Then, the geopolymer concretes were analyzed by changing their positions and the results were presented in tables and figures. The mechanical properties of geopolymer concrete 1 (GPC1) modelled in the study [7], and the mechanical properties of geopolymer concrete 2 (GPC2) [5] are the data taken from the studies in the literature. The material properties of the geopolymer concrete used in the functional stratified model are given in Table 1. Here, GPC1 concrete is composed of 60% fly ash and 40% slag and has a modulus of elasticity of 35000 MPa, while GPC2 with all fly ash matrix has a modulus of elasticity of 25000 MPa.

	Mixture		Modulus of Elasticity (MPa)	Poisson Rate
	Fly Ash	Slag		
GPC1	%60 (257.16 kg/m ³)	%40	35000	0.22
GPC2	%100 (387.10 kg/m ³)	-	25000	0.22

Geometric models for two different support conditions are given below.

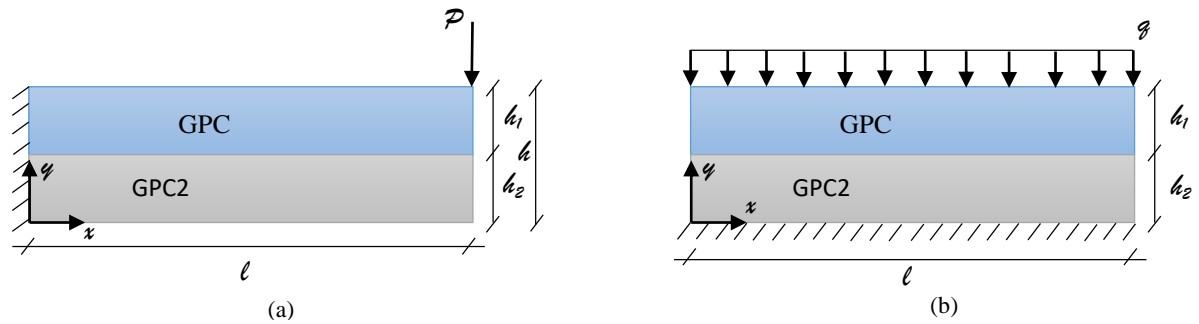


Figure 1. a) Cantilever layer model of geopolymer concretes.

b) Loading of geopolymer layers resting on fixed support.

Figure 1a shows the loading conditions for fixed-supported geopolymer concrete. Figure 1b shows two different geopolymer concrete layers under uniformly distributed loading. In both cases, GPC1 and GPC2 were relocated and analyzed, and their deformation and displacement conditions were investigated.

The mechanical behaviour of two different geopolymer layers with different material properties under different loading and bearing conditions were investigated using the finite element method (FEM). The analyses were performed with the ANSYS Mechanical Launcher 16 program.

The Finite Element Method (FEM) is a numerical analysis method widely used in engineering and science. It is especially used to model and analyze the behaviour of complex structures. FEM is an approach in which numerical methods are applied to obtain the solution of a structure by transforming it into a system of differential equations. This method divides a geometric model into a finite set of elements or nodes and models the relationships between these elements with mathematical expressions. Each element could have properties such as material properties and geometric characteristics. The equations associated with these modeled elements represent the equilibrium condition and behaviour of the system. It uses mathematical methods and algorithms for numerical analysis. First, the geometry and material properties of the problem are defined. Then, the geometry of the problem needs to be divided into elements, and

appropriate mathematical expressions need to be constructed for each element. These expressions could usually be in the form of differential or integral equations. Finally, these equations are combined as a system and solved by numerical methods to analyze the behaviour of the problem. The flowchart for the solution is given below:

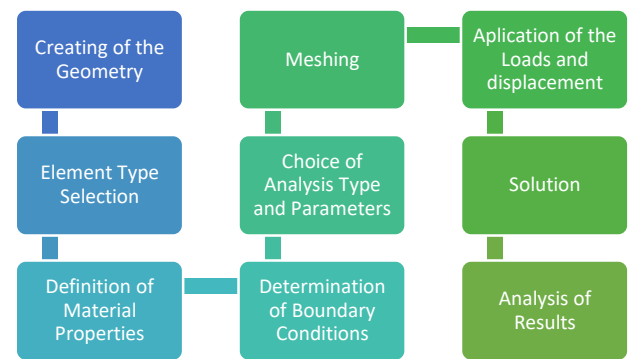


Figure 2. Flowchart of ANSYS solution.

4 Analytical Modeling Using Finite Element

Finite element models of the problem are given in Figure 3(a-b). In Figure 3(a), two geopolymer concretes were modeled, and a cantilever layer loaded a point on its end. In Figure 3(b), a model of geopolymer concrete loaded with uniformly distributed load from the top surface and resting on the fixed supports is given.

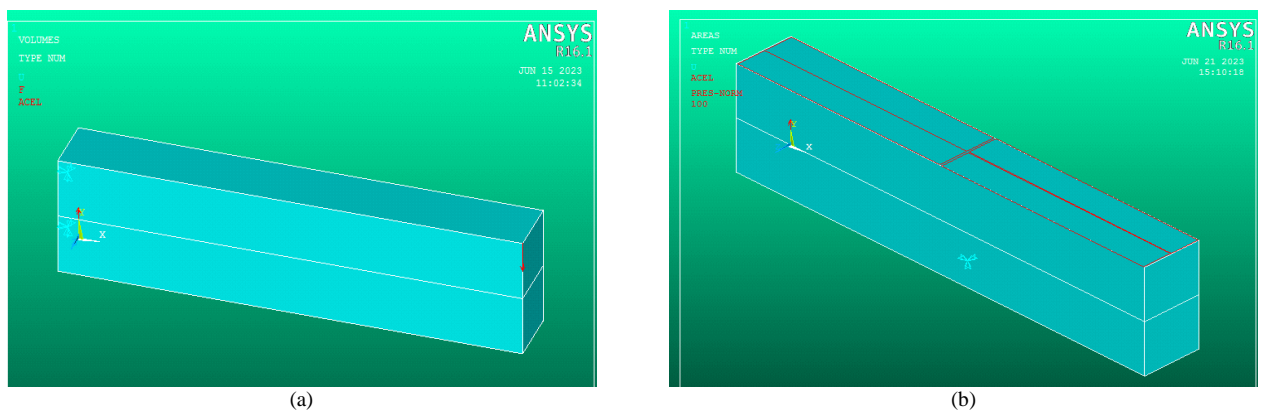


Figure 3. a) Cantilever geopolymer concrete b) Resting on fixed support geopolymer concrete.

SOLID65 was chosen as the element type. SOLID65 is a type of finite element used in ANSYS software for structural analysis. SOLID65 is a four-node tetrahedric element and provides high accuracy and precision in three-dimensional analysis. This element calculates stress,

deformation, temperature effects and other structural analysis parameters. Moreover, the material behaviour of the element is also suitable for plastic analysis using linear elastic or plastic deformation models. Figure 4 shows the operating principle of the element.

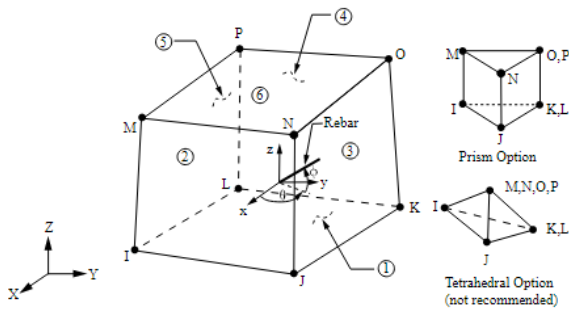


Figure 4. The operating principle of the SOLID65.

Once the material properties provided in Table 1 are introduced to the program and assigned to the geometries, a meshing process is carried out. The volumes have been divided into finite elements with 9333 nodes. A visual representation of the meshing process is provided in Figure 5.

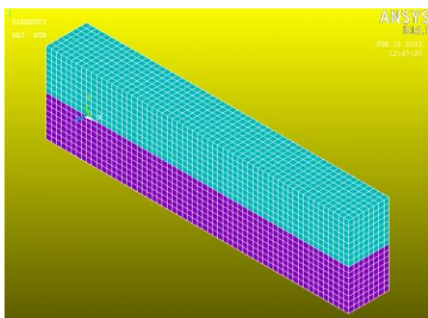


Figure 5. The geometric model is divided into meshes.

After defining the boundary conditions and loads in the problem to be analyzed statically, the solution phase started.

5 Results and Discussion

Figure 6 provides the displacement status of the console under loading conditions. Figure 7 illustrates the analysis of displacement values along the x, y, and z axes under varying P loads, with GPC1 positioned above and GPC2 below. The resultant findings are quantitatively detailed in Table 2.

In Table 2, the deformation behavior of geopolymer composite cantilever concrete loaded from the end has been numerically analyzed in the x, y, and z directions under different loads. In the first scenario, where the elasticity modulus is lower for the geopolymer concrete above and higher below, the deformation at the end of the layer was studied. In the x direction, it was observed that there was an elongation on the upper surface of the layer's endpoint and a contraction on the lower surface. It was determined that these elongation amounts increased when the positions of the geopolymer concretes were changed. The displacement in the y direction decreased when the concrete's positions were changed, while in the z direction, it increased. As the load increased, these elongation and contraction patterns also increased proportionally.

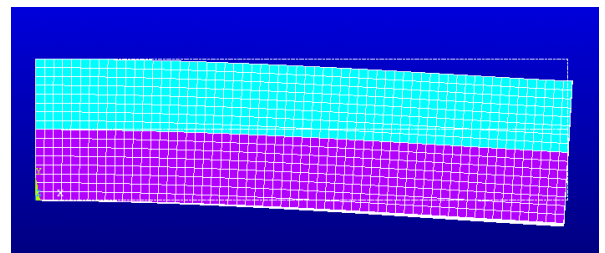


Figure 6. The state of geopolymer concrete consoles after loading.

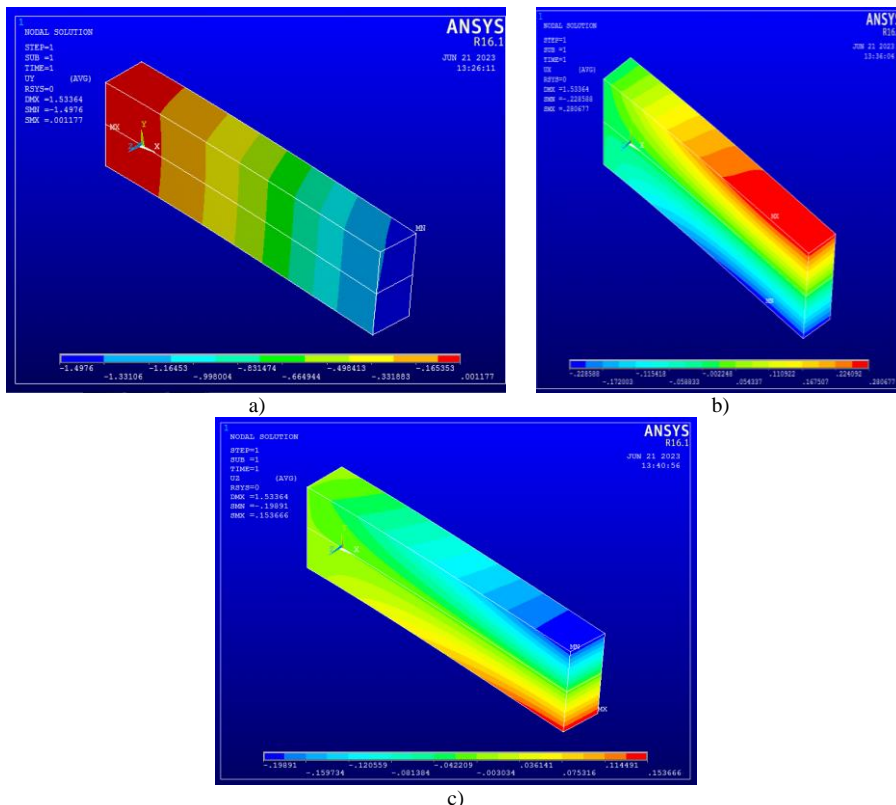


Figure 8. The alterations of geopolymer console concrete under loading between GPC1 and GPC2 δ_x , δ_y , δ_z (P=100, l=3).

Table 2. The shape deformation analysis of geopolymers concrete loaded from the cantilever’s end is presented.

Load	GPC1-GPC2						GPC2-GPC1					
	y=0			y=h			y=0			y=h		
	δ_x	δ_y	δ_z	δ_x	δ_y	δ_z	δ_x	δ_y	δ_z	δ_x	δ_y	δ_z
P=100	-0,229	-1,50	0,15	0,28	-1,50	-0,20	-0,28	-1,48	0,20	0,23	-1,48	-0,17
P=200	-0,46	-2,99	0,31	0,56	-2,99	-0,39	-0,55	-2,97	0,40	0,45	-2,97	-0,34
P=300	-0,69	-4,49	0,46	0,84	-4,49	-0,60	-0,83	-4,47	0,60	0,67	-4,47	-0,51

In Table 2, the deformation behavior of geopolymer composite cantilever concrete loaded from the end has been numerically analyzed in the x, y, and z directions under different loads. In the first scenario, where the elasticity modulus is lower for the geopolymer concrete above and higher below, the deformation at the end of the layer was studied. In the x direction, it was observed that there was an elongation on the upper surface of the layer's

endpoint and a contraction on the lower surface. It was determined that these elongation amounts increased when the positions of the geopolymer concretes were changed. The displacement in the y direction decreased when the concrete's positions were changed, while in the z direction, it increased. As the load increased, these elongation and contraction patterns also increased proportionally.

Table 3. Stress analysis of geopolymer cantilever concrete loaded with uniformly distributed load.

Yük	GPC1-GPC2						GPC2-GPC1					
	min			max			min			max		
	σ_x	σ_y	σ_z	σ_x	σ_y	σ_z	σ_x	σ_y	σ_z	σ_x	σ_y	σ_z
P=100	-48.72	-199.45	-51.11	6.09	-90.31	6.29	-44.75	-182.78	-46.81	5.68	-90.01	6.58
P=200	-97.43	-398.89	-102.22	12.18	-180.62	12.59	-89.50	-365.55	-93.62	11.28	-180.02	13.15
P=300	-146.15	-598.34	-153.33	18.27	-270.92	18.69	-134.25	-548.33	-134.25	16.91	-270.06	19.74

In Table 3, stress conditions of geopolymer composite concrete, which is fixed from below and loaded with a uniformly distributed load on its upper surface, under different loads have been examined. It was observed that when the concrete with a higher elasticity modulus is

positioned at the top, stresses decreased in all directions. As the loads increased, proportional increases in stresses were observed. The stress conditions of geopolymer cantilever concrete layers under different loadings after analysis are presented in Figure 8.

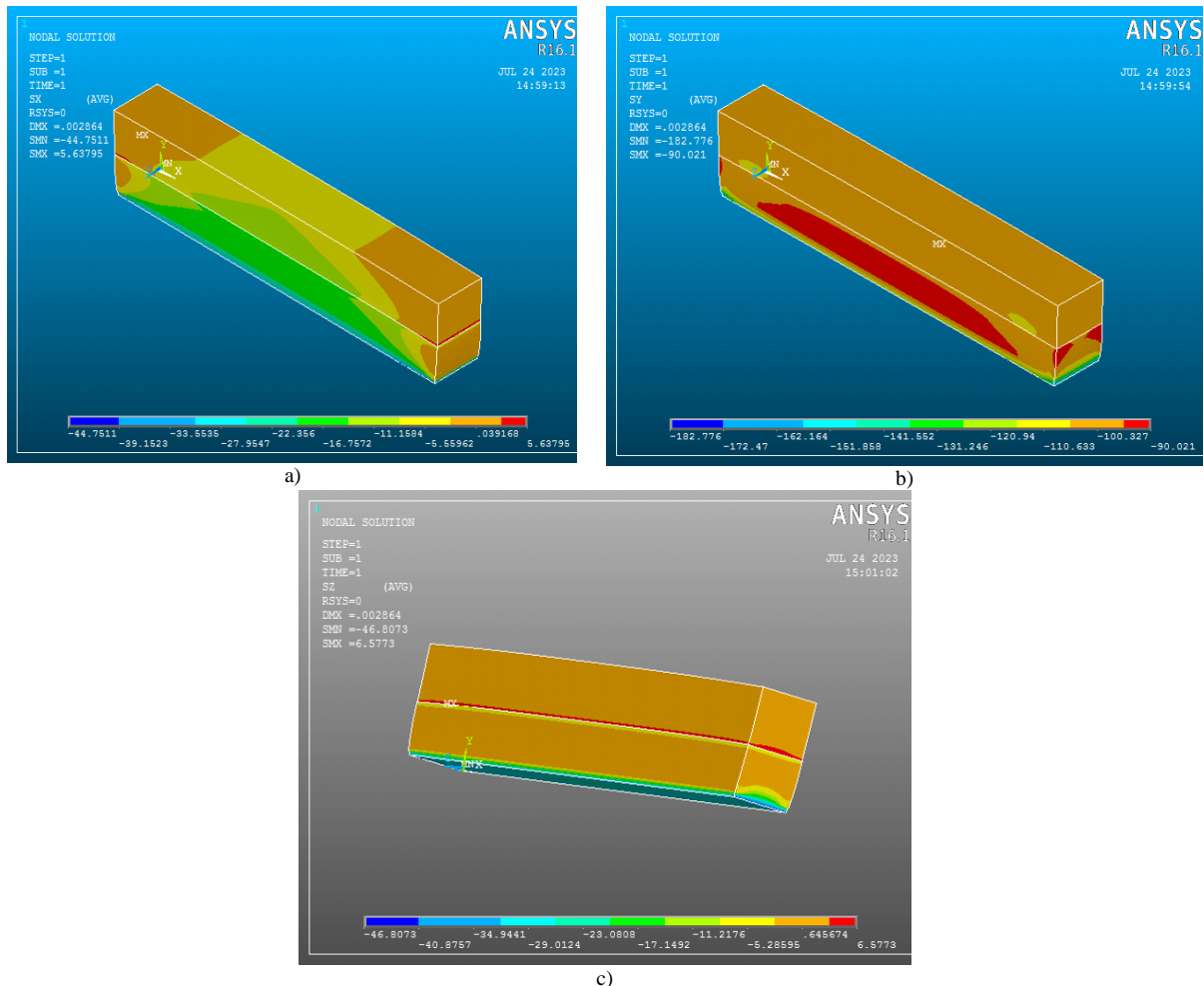


Figure 8. The stress conditions in different directions of GPC2-GPC1 (q=200, l=3, σ_x , σ_y , σ_z).

6 Conclusions

In this study, stress and deformation analyses were conducted on two geopolymer concrete layers with different material properties under different support and loading conditions. The layers were named GPC1 and GPC2 based on their properties. The analyses were performed by comparing the results with changes in the positions of the geopolymer layers. When GPC1, with a higher elasticity modulus, was positioned at the top, the deformation amounts were greater than those of GPC2. On the other hand, when GPC1, with a higher elasticity modulus, was positioned at the top, stress values were lower than in the other scenario. Most of the studies in the literature on geopolymer concrete consist of experimental studies. The main objective of this study is to investigate the mechanical behavior of geopolymer concretes using the finite element method, which is an alternative solution method. The results obtained showed that the mechanical behavior of geopolymer concretes can be investigated much faster and easier with the finite element method as an alternative to experimental studies.

Declaration

Ethics committee approval is not required.

References

- [1] McLellan, B. C., Williams, R. P., Lay, J., Van Riessen, A., & Corder, G. D. (2011). Costs and carbon emissions for geopolymer pastes in comparison to ordinary portland cement. *Journal of cleaner production*, 19(9-10), 1080-1090.
- [2] Aygörmez, Y. (2022). Performance of different binders doped Portland Cement-based mortars using volcanic slag, petroleum coke and EPS foam aggregates. *Construction and Building Materials*, 336, 127538.
- [3] Yılmaz, A., Ergün, S., Uysal, M., Dilbas, H., Aygörmez, Y., & Canpolat, O. (2023). Durability Performance of Fiber-Reinforced Metakaolin-Based and Red Mud-Fly Ash-Slag-Activated Geopolymers with Recycled Aggregates. *Arabian Journal for Science and Engineering*, 1-20.
- [4] Polat, B. Y. (2022). Self healing of alkali active mortars with expanded perlite aggregate. *Case Studies in Construction Materials*, 17, e01225.
- [5] Nguyen, K. T., Ahn, N., Le, T. A., & Lee, K. (2016). Theoretical and experimental study on mechanical properties and flexural strength of fly ash-geopolymer concrete. *Construction and Building Materials*, 106, 65-77.
- [6] Ganesan, N., Abraham, R., & Deepa, R. S. (2015). Experimental and Analytical Investigations on Geopolymer Concrete Columns under Repeated Axial Compression. *Asian Journal of Civil Engineering (bhrc)* Vol. 16, 5, P. 651-662.
- [7] Antonyamaladhas, M. R., Chachithanatham, S., & Ramaswamy, A. (2016). Performance and behaviour of ground granulated blast furnace slag imparted to geopolymer concrete structural elements and analyzed with ANSYS. *Advances in Materials Science and Engineering*, 2016.
- [8] Annapura, D., Kishore, R., & Sree, M. U. (2016). Comparative Study of Experimental and Analytical Results of Geo Polymer Concrete. *International Journal of Civil Engineering and Technology (IJCIET)*, 7(1), 211-219.
- [9] Aleem, M. A., & Arumairij, P. D. (2016). Analytical Modeling of Geopolymer Concrete with Manufactured Sand Using ANSYS. *International Journal of Advanced Engineering Technology*, 7, 1253-1255.
- [10] Waryosh W. A., & A.S. Ali, A. S. (2023). Behavior and Strength of Geopolymer Castellated Composite Beams. *Journal of Engineering and Sustainable Development (JEASD)*, Pages 365-374.
- [11] Polat, B. Y., Uysal, M., & Korkmaz, V. (2020). A research for bacterial self-healing in metakaolin based geopolymer mortars. *Sigma Journal of Engineering and Natural Sciences*, 38(3), 1401-1414.
- [12] Aydın, M. (2020). *Yeni ve Eski Nesil Betondan Üretilmiş Kompozit Kirişlerin Darbe Kuvveti Etkisi Altındaki Davranışının İncelenmesi* (Master's Dissertation Sakarya University).
- [13] Venkatachalam, S., Vishnuvardhan, K., Amarapathi, G. D., Mahesh, S. R., & Deepasri, M. (2021). Experimental and finite element modelling of reinforced geopolymer concrete beam. *Materials Today: Proceedings*, 45, 6500-6506.
- [14] Polat, B. Y., & Uysal, M. (2021). Bacterial crack healing in metakaolin based geopolymer mortars. *Journal of Building Engineering*, 39, 102291.



MODELING A SOLAR POWER PLANT WITH ARTIFICIAL NEURAL NETWORKS

Seren Arslan¹ , Hikmet Esen^{*2} , Engin Avci³ , Can Cengiz⁴ 

¹Marmara Private Education Institutions, 23200, Elazığ, Türkiye

²Firat University, Faculty of Technology, Department of Energy Systems Engineering, 23119, Elazığ, Türkiye

³Firat University, Faculty of Technology, Department of Software Engineering, 23119, Elazığ, Türkiye

⁴Vodafone, Technology Centers Operations Management, 06100, Ankara, Türkiye

Abstract

Original scientific paper

This study will enable us to estimate the power of the solar power plant with measurement data such as outdoor temperature-humidity, wind and precipitation amount, to protect the system from imbalance, and to determine the instant and daily effective energy trade more easily. By taking the data from the solar power plant installed in Samsun, Turkey, estimation was made with Artificial Neural Networks for electricity generation. In this study, Levenberg-Marguardt feed-forward backprop learning algorithm was used to find the best approach in the network. The best prediction results were obtained from the 2-layer and 5-neuron Artificial Neural Networks model, and it was observed that the system gave better training results as the number of iterations increased (multiple determination coefficient, R², 0.99818).

Keywords: Artificial neural network; solar; energy; power plant; electricity generation.

GÜNEŞ ENERJİSİ SANTRALİNİN YAPAY SİNİR AĞI İLE MODELLENMESİ

Özet

Orijinal bilimsel makale

Bu çalışma, dış ortam sıcaklığı-nemi, rüzgar ve yağış miktarı gibi ölçüm verileriyle güneş enerjisi santralının gücünü tahmin etmemizi, sistemi dengesizlikten korumamızı, anlık ve günlük efektif enerji ticaretini daha kolay belirlememizi sağlayacaktır. Samsun'da kurulu güneş enerjisi santralinden veriler alınarak elektrik üretimi için Yapay Sinir Ağları ile tahmin yapıldı. Bu çalışmada ağdaki en iyi yaklaşımı bulmak için Levenberg-Marguardt ileri beslemeli backprop öğrenme algoritması kullanılmıştır. En iyi tahmin sonuçları 2 katmanlı ve 5 nöronlu Yapay Sinir Ağları modelinden elde edilmiş olup, yineleme sayısı arttıkça sis-temin daha iyi eğitim sonuçları verdiği gözlemlenmiştir (çoklu belirleme katsayısı, R², 0,99818).

Anahtar Kelimeler: Yapay sinir ağı; güneş; enerji; enerji santrali; elektrik üretimi.

1 Introduction

As the world population increases, the need for energy is increasing day by day in proportion to the population. From past to present, human beings have always needed energy. Energy needs can be met naturally. However, until now, countries have met their energy needs from fossil fuels. The fact that this huge energy deficit in the world could not be met with non-renewable energy sources, namely fossil fuels (coal, oil, natural gas) in the long term, naturally increased the need for renewable energy sources.

Predicting the production values of SPP maximizes the profitability of the plant. Renewable energy sources are built with long-term guarantees and this causes the production risk shares of power plants to decrease. In order for renewable power plants to operate in the market,

production planning and estimations, like other energy sources, are very important for the manufacturer. In addition, determining the environmental conditions and predicting in advance while determining the efficient location and settlement will increase the profit rate.

It is seen that some studies that are considered important have come to the fore after a literature review on GES production estimation. SPP is a very popular energy production method in our country, as it is a clean and uninterrupted power source and in line with the incentives given. Due to Turkey's geographical location, the yield obtained from SPP also has a high potential. Electricity generation with solar energy has started to be recognized and applied more and more every day in the world and in Turkey [1]. Recently, when we examine these systems in terms of installation costs and turnaround times, troublesome processes come to mind. However, as

*Corresponding author.

E-mail address: hikmetesen@firat.edu.tr (H. Esen)

Received 02 August 2023; Received in revised form 22 November 2023; Accepted 05 December 2023

2587-1943 | © 2023 IJIEA. All rights reserved.

Doi: <https://doi.org/10.46460/ijiea.1336917>

the technology and market conditions in solar energy systems get stronger day by day, it will be inevitable that the costs will decrease and become widespread [2].

In the last 15 years, electricity generation from wind power plants has increased from 39836.3 GWh to 129637.0 GWh with an average annual growth rate of 8.2%. These rates are 4.6%, 41.0%, 32.5%, 192.7% and 29.2% in hydro, geothermal, wind, solar and biomass, respectively. These rates are 12 years for wind and geothermal and six years for solar [3].

SPP's are one of the energy production facilities that are increasing in importance with their clean and renewable features. Photovoltaic SPPs are the most common technology for renewable energy generation today, and since 2016 PV solar has been the technology with higher growth [4, 5].

A system has been developed for a SPP production facility located in Kahramanmaraş, which can make a production estimation the day before. ANN is used in this system. Weather forecasts and past production values were used as inputs. It has been observed that the cloud estimation used structure has lower MSE and higher R values. In addition, it has been observed that the artificial neural network created using 10 neurons is more successful than the 5-neuron structure. The results obtained from the system were evaluated and it was seen that the system using cloud forecasting was much more successful [6].

Environmental factors (solar radiation, temperature, wind, humidity, PV panel temperature) and power values obtained from photovoltaic panels were measured and recorded for 1 year with the measurement stations established in three pilot regions (Adiyaman-Malatya-Şanlıurfa), which differ from each other in terms of environmental factors. The effects of humidity, wind speed and PV panel temperature on panel power generation were determined by making an estimation by passively training the relevant parameters in the general algorithm, and the effects of these parameters on the PV panel power. It was observed that the humidity parameter was 2.6%, the wind parameter was 0.8%, and the PV panel temperature parameter was 1.6% effective on the estimation of the PV panel power. With the trained ANN models, the PV panel power generation for any day was predicted and a high accuracy (99.34%) was determined when the actual values obtained from the measurement station for that day were compared with the ANN estimation results [7].

In another study [8], forward feedback propagation artificial neural networks and KNN (K-Nearest Neighbors) methods are used to estimate power values using the production data of photovoltaic panels (temperature, humidity, pressure, radiation). Panel values taken from an active site, whose installation was completed, were trained with both methods and the results obtained were compared. In the results obtained, the power values of the photovoltaic panels were classified using the ANN model developed with the highest accuracy of 98.7945%. As a result of the developed study, it was seen that the learning models used for power estimation had very high performance and the obtained data predicted results very close to the real field data. It was concluded that both estimation models developed in

locations with different structural characteristics can be used according to the seasonally changing load demand.

He proposed a NARX model to estimate PV out put power using global solar radiation, sunlight intensity, hourly temperature, minimum temperature, maximum temperature, wind speed, relative humidity, air pressure and precipitation history data as inputs. The hour angle and the sun zenith angle of the mentioned place were also calculated and used in the modeling. In addition, the effects of increasing and decreasing the number of delays by changing the number of neurons in the hidden layer were also observed. The performance achieved by the NARX model is discussed using statistical evaluation parameters. The performance of the model is acceptably good and the power data can be predicted with errors of MAE, MAPE, MBE and n RMSE respectively 52.0815, 11.83%, 8.253 and 8.57% for the hourly forecast and 20.858, 4.60% for the daily forecast [9]. In this study, data were taken from the four 1 MW SPP fields in Samsun, based on June and July of 2022. Maximum, minimum, average temperature values, relative humidity, minimum, average, maximum wind speed and precipitation amount in these months were given to the forecast model as inputs. The daily production values of the SPP power plant were calculated as output. Very close results were obtained between the actual values obtained from the experiments and the estimated values.

2 Field Data

It has been determined that the production of the facilities varies periodically in the examinations made on a real solar power plant of the same size, installed in the province of Samsun, located in the Black Sea region of Turkey, for about 2 years.

What we think is valuable for academic study in the part of the established facility is that the power plant is located in the Black Sea Region of Turkey and was established in four different directions. The facility was established on the roofs of a chicken farm located within the borders of the Bafra district of Samsun province, and the roof slopes were established as 12 degrees. In the established facility, 1 MW system was installed in the North, South, East and West directions. Since the number of roofs is low in the North and South directions, 1283 kWp can be placed on 10 roofs by tight placement. Since there are 14 roofs on the east and west directions, 1308 kWp has been placed with a more comfortable layout. The top view of the facility is given in Fig.1 [1].



Figure 1. Top view of the SPP facility in Samsun [1].

Data from the established SPP systems continued to be collected in 2022. The 3-year production values of our

SPP systems installed in 2020 are given in Table 1. As a result of the data received, the production value in 2022 was 5.899.187 kWh. In 2022, the production was very close to the previous year and realized as 5.938.120. The production difference between 2021 and 2022 was around 1%. The target value in 2020 is the values predicted by the programs and the installation companies. In 2021, the value was taken to the highest value that can be produced by the company officials. This turned out to be a lack of overproduction. In 2022, the most obvious and appropriate target value was determined by taking the arithmetic average of two years, and it was seen that a production value very close to this value was realized at the end of the year.

Table 1. Comparisons by year of production [1].

Years	Target Production (kWh)	Actual Production (kWh)	Difference (%)
2020	5.624.888	6.409.125	13.9
2021	6.270.165	5.899.185	-5.9
2022	5.988.762	5.938.120	-0.8

The daily, monthly and annual data obtained in the system were recorded and the system efficiency was calculated with analyzes from different parameters. The efficiency of solar panels is calculated by using Eq. 1 [1].

$$\eta_{max} = P_{max} / (I \cdot A) \tag{1}$$

here, η_{max} is the maximum efficiency, P_{max} is the maximum power output (W), I is the amount of radiant flux from the sun (W/m^2), and A is the panel area (m^2). If we give an example from the panel we use; The area of our 310W panel is $1.64 m^2$ and its efficiency was calculated as in Eq. 1 under test environment conditions. As can be seen from the process below, the efficiency value of our panel, which was preferred for $1000 W/m^2$ radiation value, was 18.9%.

$$\eta_{max} = (310 W) / (1000 W/m^2 \cdot 1.64 m^2) = 0.189$$

System reviews have been advanced over two main scopes. It was made in the form of daily reviews and monthly reviews. Different evaluations were made by taking into account other factors (temperature, wind speed, pollution, etc.) by collecting the same radiation values by creating special data sets in daily examinations. In the monthly evaluation, the systems were examined by creating data sets over the monthly average factor values. Values were evaluated on days with irradiance values of $>1000W/m^2$ at full efficiency in the daily reference examinations. Since the number of days when the panel works at full capacity in terms of solar panels operating inefficiently in the Black Sea region except summer months, the evaluations were made by taking daily data in May, June, July and August. In Table 2, the sunshine duration of Turkey as a region and the amount of energy per square meter per year are given.

Table 2. In Turkey, the duration of sunshine by region and the amount of energy per square meter per year [4].

Region	Sunshine Duration (hours/year)	Total Solar Energy (kWh/ m^2 /year)
Southeastern	2.993	1.460
Anatolia	2.956	1.390
Mediterranean	2.664	1.365
Eastern Anatolia	2.628	1.314
Central Anatolia	2.738	1.304
Aegean	2.409	1.168
Marmara	1.971	1.120
Black Sea		

3 Modeling

Several different power estimation model studies have been published in recent years related to PV plants. The solutions in these studies can be classified as physical, statistical and hybrid methods. A few of these models used for PV plants were aimed at estimating the amount of solar radiation [10–12]. Some studies offer models dedicated to hourly power generation forecasting, especially in PV plants [13–16]. The intelligent method calculation technique known as Artificial Neural Networks (ANN) is the most applied technique in the different prediction models obtained, but different from this, simpler methods have been used in a few articles [17-21].

ANN is machine learning developed with the aim of automatically performing the human brain's advanced learning function, such as the ability to generate, create and explore new information on its own. It mimics the structure of biological neural networks in the human brain, learning, remembering and generalizing properties. The learning process in ANN is carried out by using different examples and making many trials. During learning, some rules are set by giving input and output information.

Artificial nerve cells come together to form the ANN. The coming together of nerve cells is not random. Nerve cells come together in three layers and in each layer parallel to each other to form the network. These layers are:

Input layer: It is called the layer in which the samples that come as input to a network are given as input. There should be input neurons up to the number of features of the examples to be taught in the input layers.

Hidden layers: The layer between the input layer and the output layer is called. In this layer, forward comprehensive calculations and backward comprehensive error propagation are performed. It is possible to have more than one middleware within a network. Having many layers causes computational complexity and computational processes to increase.

Output layer: The processing elements in this layer receive the data from the middleware and produce the output that the network should produce for the input set (sample) presented from the input layer. Each cell can have multiple inputs, but only one output. This output can be linked to any number of cells.

An image showing the network structure of the ANN is given in Fig. 2 [21].

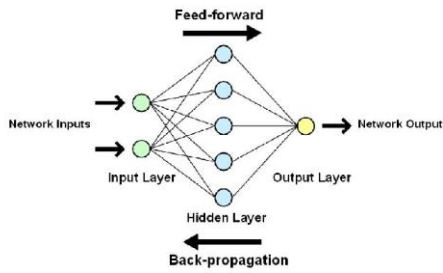


Figure 2. Artificial Neural Network Structure.

Just as biological neural networks have nerve cells, ANN has artificial nerve cells. Artificial nerve cells are also called processing elements in engineering science. Each processing element has 5 basic components. These; inputs, weights, summation function, feedforward neural network and backward computation [22].

In this study, it was tried to estimate the daily production values of a SPP using ANN. The data we use are the daily values for July and June from an established SPP. Maximum, minimum, average temperature values, relative humidity, minimum, average, maximum wind speed and precipitation amounts for the months of June and July were taken as input values to the ANN.

Evaluation was made on a total of 62 data taken daily for the months of July and June. Daily production values were estimated as output value. After completing the ANN training, the program that calculates the best prediction values was obtained by changing some structural features of the ANN in the next stages.

In the designed ANN system, the feed forward back propagation model was used as the network type by assigning the input and output values. In the system, there are 8 inputs as minimum, average and maximum temperature values, relative humidity, minimum, average, maximum wind speed and precipitation amount. The daily values of June and July were recorded over the SPP field of 2022. The image of the designed ANN model is given in Fig. 3.

In the designed MATLAB model, "TRAINLM and TRAINGDX" functions were tested separately as training functions. "LEARNGDM" is used for Adaptation

Function, MSE as performance function and "TANSIG" as transfer function.

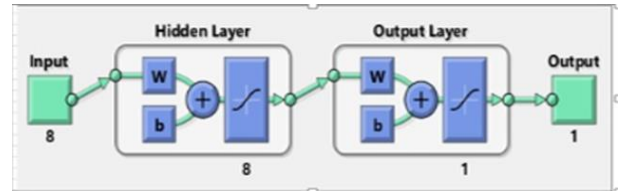


Figure 3. ANN model image used in the study.

In some trials, the number of iterations was increased and the number of neurons and layers was kept constant. In some trials, the best results were tried to be obtained with different trials by increasing or decreasing the number of neurons and layers and keeping the number of iterations constant. The results of training, accuracy, test and mean (all) values obtained in different trials are given in Table 3.

Table 3. General data obtained as a result of the analysis.

Iteration	Neuron	Layer	Training	Validation	Test	Average
250	5	1	0.687	0.540	0.765	0.664
500	5	2	0.722	0.571	0.536	0.640
1000	5	2	0.510	0.955	0.923	0.647
1000	3	1	0.820	0.757	0.896	0.822
1500	3	1	0.754	0.998	0.880	0.822
2000	10	1	0.847	0.855	0.811	0.832
2000	10	2	0.815	0.798	0.801	0.792
2000	5	2	0.835	0.916	0.996	0.879
2500	5	2	0.985	0.860	0.781	0.740
2500	5	1	0.844	0.901	0.940	0.875
3000	5	2	0.830	0.980	0.810	0.870
3000	10	2	0.886	0.812	0.986	0.887
3500	5	1	0.980	0.761	0.881	0.871
3500	8	1	0.764	0.938	0.914	0.817

When the experimental results are compared with the numerical analysis made using different trials, different neuron and layer numbers; The best results were obtained using 2 layers - 5 neurons. The results obtained under these conditions are shown in Table 4.

Table 4. The best results obtained in the study.

Iteration	Neuron	Layer	Training	Validation	Test	Average
2000	5	2	0.83519	0.91677	0.99632	0.8792
3000	5	2	0.83164	0.99818	0.94475	0.89333

Model validation is the process by which the input vectors from the input/output datasets on which the ANN is not trained are presented to the trained model to see how well the trained model predicts the corresponding dataset output values. In order to compare the estimated and actual values for model validation, the multiple determination coefficient (R^2) statistical method was found and interpreted.

The multiple determination coefficient (R^2) was obtained from Equation 2 below [21].

$$R^2 = 1 - \frac{\sum_{m=1}^n (y_{est,m} - t_{mea,m})^2}{\sum_{m=1}^n (t_{mea,m})^2} \quad (2)$$

where n is the number of data patterns in the independent data set, $y_{est,m}$ indicates predicted, $t_{mea,m}$ is the measured value of a data point (m).

In Fig. 4, the program results obtained in the study are given according to 2000 iterations. The R^2 value is shown according to the combination of training, accuracy, test and average values specified in Table 4. R^2 value was calculated as 0.91 according to 2000 iterations. In Fig. 5, the program results obtained in the study are given according to 3000 iterations. The R^2 value is shown according to the combination of training, accuracy, test and average values specified in Table 4. The R^2 value was calculated as 0.99 according to the number of 3000 iterations.

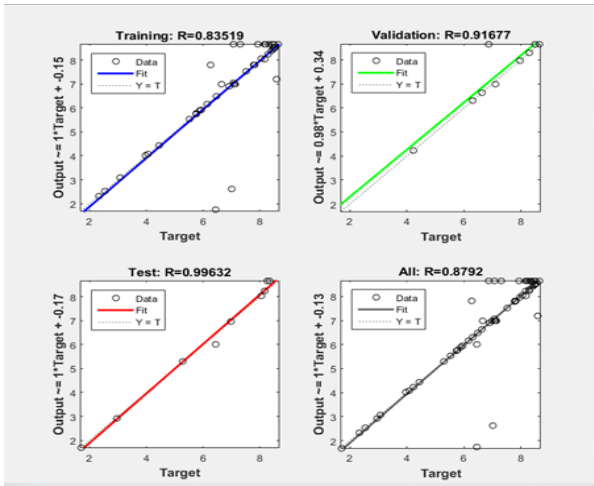


Figure 4. Training, validation, test and average values for 2000 iterations.

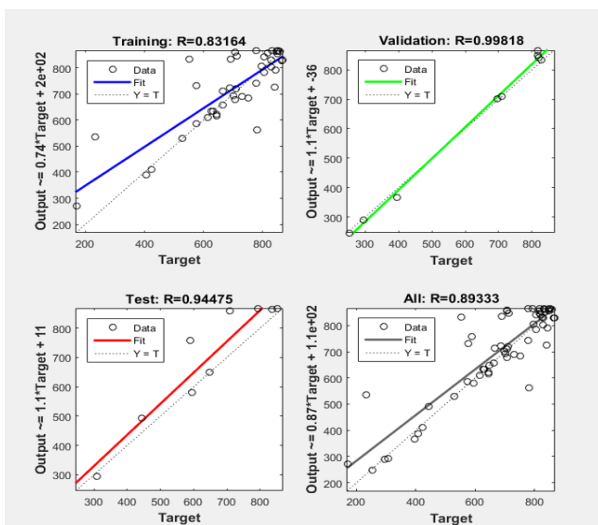


Figure 5. Training, validation, test and average values for 3000 iterations

As a result of the comparison, the best values were obtained in double-layered trials. It was observed that learning increased as the number of iterations and neurons increased. In the best ANN model we obtained, different values that we did not use in education were used as test data. The estimated results obtained by the ANN and the actual values measured over the SPP system are given in Fig. 6.

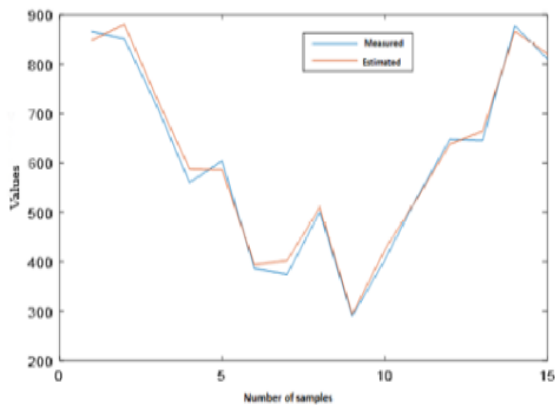


Figure 6. Image of comparison of estimated values with measured values.

4 Conclusion

In this study, which we have done using ANN, a system has been developed to estimate the production values of a SPP facility. In this developed system, minimum-maximum-average temperature, wind, relative humidity and precipitation values were used as input data. The results obtained by changing the structural features of the ANN (neuron-layer-iteration number) were evaluated. The best prediction results were obtained using 2 layers and 5 neurons. In addition, it was observed that the system gave better training results as the number of iterations increased ($R^2= 0.99818$). Thanks to this study, it will help to interpret the real field data for the SPP to be established in future studies.

Declaration

Ethics committee approval is not required.

References

- [1] Cengiz, C. (2023). *Comparison of the parameters of solar power plants with the same characteristics installed in four different directions*. (Master’s Dissertation, Firat University).
- [2] International Energy Agency (2023). *Solar PV Global Supply Chains – Analysis 2023*. Retrieved March 2, 2023 from <https://www.iea.org/reports/solar-pv-global-supply-chains/executive-summary>
- [3] Sahin, H., Esen, H. (2022). The usage of renewable energy sources and its effects on GHG emission intensity of electricity generation in Turkey. *Renew Energy* 192:859–69.
- [4] Republic of Turkey Ministry of Energy and Natural Resources. *Electricity (2023)*. Retrieved March 2, 2023 from <https://enerji.gov.tr/infobank-energy-electricity>
- [5] Alvara, R.R. (2018). *Design and Modelling of a Large-Scale PV Plant. Escola Tècnica Superior d’Enginyeria Industrial de Barcelona*.
- [6] Gök, A. O., Yıldız, C., & Şekeli, M. (2019). Yapay sinir ağları kullanarak kısa dönem güneş enerjisi santrali üretim tahmini: Kahramanmaraş örnek çalışması. *Uluslararası Doğu Anadolu Fen Mühendislik ve Tasarım Dergisi*, 1(2), 186-195.
- [7] İçel Y. (2019). *Güneş enerji sistemlerinin performans tahmini için yapay sinir ağları ile modellenmesi ve verimliliğin incelenmesi* (Master’s Dissertation, Inonu University)
- [8] Dinçer, A., & İlhan, U. (2022). Fotovoltaik Panellerde Güç Tahminlenmesi için Yapay Zekâ Yöntemlerinin Kullanılması. *Tekirdağ Ziraat Fakültesi Dergisi*, 19(2), 435-445.
- [9] Nkuriyongoma, O., & Selçuklu S. B. (2021). Solar power plant generation forecasting using NARX neural network model: A case study. *I. J. of Energy Applications and Technologies*, 8(3), 80-92.
- [10] Wang, F., Mi, Z., Su, S., & Zhao, H. (2012). Short-term solar irradiance forecasting model based on artificial neural network using statistical feature parameters. *Energies*, 5, 1355–1370.
- [11] Mellit, A., & Pavan, A. M. (2010). A 24-h forecast of solar irradiance using artificial neural network: Application for performance prediction of a grid-connected PV plant at Trieste, Italy. *Sol. Energy*, 84, 807–821.

- [12] Hocaoglu, F. O., Gerek, O. N., & Kurban, M. (2008). Hourly solar radiation forecasting using optimal coefficient 2-D linear filters and feed-forward neural networks. *Sol. Energy*, 82, 714–726.
- [13] Pedro, H. T. C., & Coimbra, C. F. M. (2012). Assessment of forecasting techniques for solar power production with no exogenous inputs. *Sol. Energy*, 86, 2017–2028.
- [14] Izgi, E., Öztopal, A., Yerli, B., Kaymak, M. K., & Sahin, A. D. (2012). Short-mid-term solar power prediction by using artificial neural networks. *Sol. Energy*, 86, 725–733.
- [15] Shi, J., Lee, W.J., Liu, Y., Yang, Y., & Wang, P. (2012). Forecasting power output of photovoltaic systems based on weather classification and support vector machines. *IEEE Trans. Ind. Appl.*, 48, 1064–1069.
- [16] Alamsyah, T., Sopian, K., & Shahrir, A. (2004). Predicting average energy conversion of photovoltaic system in Malaysia using a simplified method. *Renew. Energy*, 29, 403–411.
- [17] Monteiro, C., Fernandez-Jimenez, L. A., Ramirez-Rosadoc, I.J., Muñoz-Jimenez, A., & Lara-Santillan, P. M. (2013). Short-term forecasting models for photovoltaic plants: Analytical versus soft-computing techniques. *Math. Problems Eng.*
- [18] Ulbricht, R., Fischer, U., Lehner, W., & Donker, H. (23–27 September 2013). First steps towards a systematical optimized strategy for solar energy supply forecasting. In Proceedings of the European Conference on Machine Learning and Principles and Practice of Knowledge Discovery in Databases (ECMLPKDD 2013), Prague, Czech Republic.
- [19] Ogliari, E., Grimaccia, F., Leva, S., & Mussetta, M. (2013). Hybrid predictive models for accurate forecasting in PV systems. *Energies*, 6, 1918–1929.
- [20] Dolara, A., Grimaccia, F., Leva, S., Mussetta, M., & Ogliari, E. (2015). A physical hybrid artificial neural network for short term forecasting of PV plant power output. *Energies*, 8:1138–53.
- [21] Abdelhak K., Razika I., Ali B., Abdelmalek A., Müslüm A., Nacer L., & Nabila I. (2023). Solar photovoltaic power prediction using artificial neural network and multiple regression considering ambient and operating conditions, *Energy Conversion and Management*, Volume 288.
- [22] Rocha Vaz, A.G.C. (2014). Photovoltaic Forecasting with Artificial Neural Networks, (Master's Dissertation, Lisboa University.)



A REVIEW AND EVALUATION STUDY OF MAXIMUM POWER POINT TRACKING TECHNIQUES FOR PV SYSTEMS

Fuad Alhaj Omar^{*1} 

¹Department of Electric and Energy, Zonguldak Bülent Ecevit University, Turkey.

Abstract

Original scientific paper

The issue of improving the efficiency and effectiveness of PV (Photovoltaic) systems remains a concern for researchers and manufacturers who aim to make these systems cost-effective, thereby encouraging their wider adoption. To achieve this goal, increasing the efficiency of the PV generation system by implementing the Maximum Power Point Tracking (MPPT) system has been proposed. Enhancing the energy output from the PV system is considered a crucial aspect of improving efficiency, as it will lead to increased revenue. Consequently, the cost of the generated energy is reduced, approaching that of energy produced by conventional systems based on fossil fuels. This review paper discusses conventional MPPT techniques designed to extract the maximum available power from PV panels operating under uniform environmental conditions. Subsequently, it highlights why these techniques often fail to perform adequately under partial shading conditions. Following this, modern MPPT techniques explicitly designed to operate under non-uniform and partial shading conditions are analyzed.

Keywords: MPPT; photovoltaic system; partial shading conditions; hot spot phenomena; global tracking.

PV SİSTEMLERDE KULLANILAN MAKSİMUM GÜÇ NOKTASI İZLEME TEKNİKLERİNİN İNCELENMESİ VE DEĞERLENDİRİLMESİ

Özet

Orijinal bilimsel makale

PV sistemlerinin verimliliğini ve etkinliğini artırma konusu, bu sistemleri maliyet etkin hale getirmeyi ve böylece daha geniş çapta benimsenmesini teşvik etmeyi amaçlayan araştırmacılar ve üreticiler için bir endişe kaynağı olmaya devam etmektedir. Bu amaca ulaşmak için maksimum güç noktası izleme (MPPT) sistemi kullanılarak PV üretim sisteminin verimliliğinin artırılması önerilmiştir. PV sisteminden üretilen enerjiyi artırmak, gelirleri artıracacağı için verimliliği artırmada önemli bir unsur olarak kabul edilir. Sonuç olarak, üretilen enerjinin maliyeti düşmekte, bu da fosil yakıtı dayalı geleneksel sistemlerden üretilen enerjinin maliyetine yaklaşmasına neden olmaktadır. Bu makale, tek tip çevresel koşullar altında çalışan PV panellerinden maksimum kullanılabilir gücü çıkarmak için tasarlanmış geleneksel MPPT tekniklerini tartışmaktadır. Daha sonra bu tekniklerin kısmi gölgeleme koşulları altında yeterli performans gösterememesinin nedeni vurgulanmıştır. Bunu takiben, kısmi gölgeleme koşulları altında çalışmak üzere tasarlanmış modern MPPT teknikleri analiz edilir.

Anahtar Kelimeler: MPPT; fotovoltaik sistem; kısmi gölgeleme koşulları; sıcak nokta fenomeni; global izleme.

1 Introduction

Recently, the importance of renewable energy has reached an unmatched height as a result of fossil fuel depletion. Among all the renewable energy resources the PV systems have received the most attention due to several merits, for instance, environmental friendliness, availability, low maintenance, and a longer lifespan, (typically more than 20 years) [1]. These advantages have contributed to the rapid development of PV systems worldwide in comparison to other types of renewable

energy sources [2, 3]. The strong dependence of PV systems upon the atmospheric conditions makes extracting the maximum available power from its nonlinear characteristics more difficult [4], (see Figure 1).

During the past several years, with the intention of handling this issue and enhancing the efficiency of PV systems and extracting as much power as possible from PV modules, many MPPT strategies have been proposed and established [6, 7]. Proposed MPPT techniques differ in several aspects such as simplicity, efficiency, sensor requirements, cost, hardware implementation,

* Corresponding author.

E-mail address: fuad.a@beun.edu.tr (F. A. Omar)

Received 10 October 2022; Received in revised form 06 October 2023; Accepted 31 October 2023

2587-1943 | © 2023 IJIEA. All rights reserved.

Doi: <https://doi.org/10.46460/ijiea.118697>

convergence speed and other aspects. Each algorithm has its own features and applications. Since one is suitable for a specific application and not suitable for another, they can be classified into two categories: the conventional MPPT algorithms and new MPPT optimization algorithms. However, if employing a simpler and less expensive algorithm can yield similar even superior results, it does not seem sensible to adopt a more expensive or more sophisticated method. This is the reason why some of the proposed algorithms are not preferred in PV system realizations. In the following sections, an overview of the many proposed MPPT algorithms is presented.

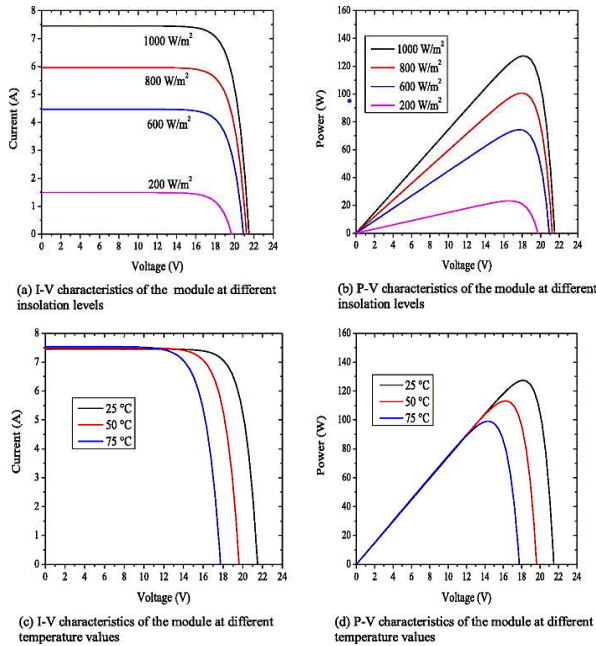


Figure 1. Characteristics of the PV module under different irradiance levels and temperatures [5].

2 Conventional MPPT Techniques

2.1 Constant Voltage (CV) Algorithm

This algorithm is considered one of the simplest and fastest MPPT techniques. By matching the measured solar module voltage V_{PV} to a constant reference voltage equal to the V_{MPP} , the operating point is kept near MPP [8]. In this technique, only one voltage sensor is employed to measure the solar module voltage V_{PV} and compare it with the reference voltage V_{MPP} , from which the corresponding duty cycle of the DC-DC converter is set up [9], as shown in Figure 2.

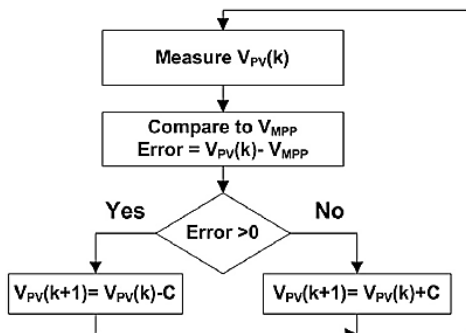


Figure 2. Constant voltage algorithm flowchart [10].

The main drawback of this technique is that it neglects the effects of ambient temperature and irradiance level on the solar module; therefore, the operating point does not exactly match the MPP. Generally, this technique is often integrated with other MPPT techniques to obtain high accuracy and enhance the efficiency of the PV system [10].

2.2 Open Circuit Voltage Method

This method relies on the linearly proportional relationship between open-circuit voltage V_{OC} and the PV module output voltage at MPP. The relationship is given in equation (1), where K_1 is a constant that relying on the fill factor FF, photocell features, and atmospheric conditions [11].

$$V_{MPP} \cong K_1 \cdot V_{OC} \tag{1}$$

The value of K_1 has to be determined beforehand by measuring the values (V_{OC}, V_{MPP}) for the PV module being used under various insolation and temperature levels and it is reported to be in the range between 0.71 and 0.8. Once the K_1 is known, the system is momentarily interrupted to measure V_{OC} . Subsequently, the V_{MPP} can be computed using the equation (1) and MPP will be updated [10]. This method can be achieved with the flowchart shown in Figure 3. Since the equation (1) is only an approximation, the operating point technically is never matching to the MPP and this incurs power loss. Even though this method is not a true MPPT technique, it is inexpensive and simple to implement as it is not necessary to use microcontrollers [12].

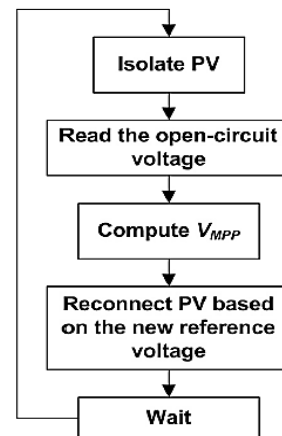


Figure 3. Open circuit voltage algorithm flowchart [10].

2.3 Short Circuit Current Method

Just like in the open-circuit voltage method, the short-circuit current method is based on the observed fact that, under fluctuating weather conditions, the PV module current at MPP (I_{MPP}) is nearly linearly related to the short-circuit current (I_{SC}) of the same PV module, as illustrated in equation (2) [12, 13].

$$I_{MPP} \cong K_2 \cdot I_{SC} \tag{2}$$

Where, K_2 is a proportionality constant depending largely on the photocell features, atmospheric conditions, and the fill factor FF. Similar to the previous method, K_2 has to be previously determined by performing a scan on the PV module being used under various insolation and temperature levels. However, the constant K_2 is between (0.78 and 0.92). In order to measure (I_{SC}) during the operation, a switch and a current sensor must be added to the system [14]. This will increase the complexity and cost.

If the DC-DC boost converter is used, then the transistor in the converter can be delegated to short the PV module [15]. Hence, the benefits and drawbacks of this method are similar to those of the open-circuit voltage method. The flow chart of this method is shown in Figure 4.

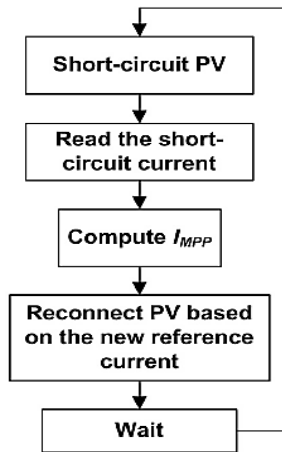


Figure 4. Short circuit current algorithm flowchart [10].

2.4 Open Circuit Voltage Pilot PV Cell Method

This method was proposed to eliminate the defects resulting from the interrupting process occurring in the open-circuit voltage method during the measurement of V_{OC} [10]. Wherein a pilot solar cell; which is electrically isolated from the rest of the PV module; is used to measure the value of open circuit-voltage V_{OC} , then according to the previous equation (1), the corresponding maximum voltage value V_{MPP} is determined. Under partial shading conditions, this technique suffers from inaccuracy. This results in a mismatch between the V_{MPP} of the pilot solar cell and the actual value of the used solar module [16].

2.5 Feedback Voltage or Current Method

Similar to the constant voltage method, in this technique, a feedback control loop is used to deliver the voltage (current) extracted from the solar module to a certain level. The control process is performed by using the error; the difference between the reference voltage and the solar module voltage (current); with a view to calibrating the duty cycle of the DC-DC converter [17], as shown in Figure 5.

The algorithm can bring the operating point of the system near to the actual MPP with a slight iteration. Although the algorithm has the advantages of high convergence speed, simplicity, and ease of implementation, it fails to find the real MPP under partial shading conditions [10].

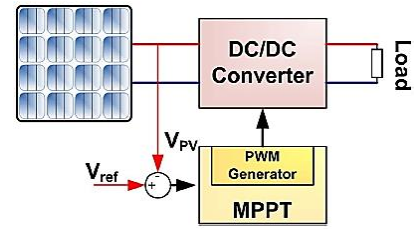


Figure 5. Voltage-feedback with PWM modulation [10].

2.6 P-N Junction Drop Voltage Tracking Method

This method is based on the physical fact that the thermal characteristics of the solar cell are similar to the thermal characteristics of the p-n junction diode. Consequently, low-cost p-n junction diodes are utilized to produce the reference voltage of the solar module, where they are integrated into the reverse side of the solar panel. Therefore, the surface temperature changes in the atmosphere will be detected by the diodes, causing a change in the forward voltage across the p-n junction diodes [18]. Figure 6 shows the control circuit used in this method, where the input voltage of the pulse width modulator is given as follows:

$$dV_R = K_2(V_{PV} - V_{ref}) = K_2(V_{PV} - K_1V_d) \tag{3}$$

where, V_{PV} is the output voltage of the PV module, V_{ref} is the reference voltage, V_d is the voltage across the p-n junction diodes, K_1 is the gain of the amplifier Amp1 and K_2 is the gain of the amplifier Amp2.

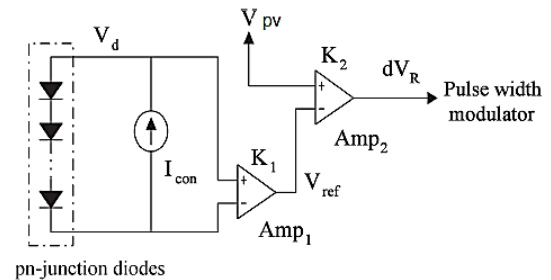


Figure 6. Control-circuit configuration of the P-N junction drop voltage tracking method [10].

2.7 Look-up Table Method

For the proposed MPPT technique, a look-up data table of all possible atmospheric conditions is formed in advance to be compared with actual atmospheric conditions. Then, depending on the control system, the saved values are compared with the actual values of the temperature and insolation. According to the comparison result, a duty cycle corresponding to the MPP is generated. The comparison process is carried out every cycle to ensure that the operating point is at the highest available power MPP [19, 20]. This method is predetermined based on practical tests under different atmospheric conditions. The controller used should contain a memory with a large enough storage capacity for storing the available input data.

2.8 Load Current or Load Voltage Maximization

When connecting a power converter to a PV module, maximizing the extracted power from the PV module leads to maximizing the output power of the converter. In contrast, maximizing the output power of the converter leads to a super extracting power from the PV module, on the assumption that energy losses in the converter are zero. It should be noted that most loads are either resistance, voltage-source, current source, or integration of all these kinds [21], as illustrated in Figure 7. In voltage source type load, in order to obtain the maximum output power, the load current should be maximized. For other kinds of loads, the output current or output voltage can be utilized to maximize the output power. In this technique, only one sensor is required. Therefore, maximizing the output power for all types of load can be carried out by maximizing either the output current or output voltage. In this technique, to control the power converter and adjust the operating point of the PV module to keep it near the MPP, a feedback loop is used. According to the assumption that the power converter losses are zero, operating cannot be achieved exactly at the MPP, and this is one of the drawbacks of this method [22, 23].

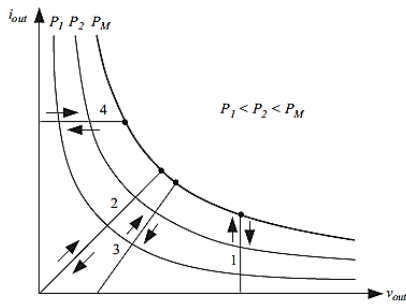


Figure 7. Load types: 1-voltage-source, 2-resistive, 3-resistive and voltage-source, 4-current-source [21].

2.9 Only Current Photovoltaic Method

In this algorithm, the output power can be maximized depending on the PV current [24]. In this system, a battery is connected to the PV module across a DC-DC converter; thus, regardless of the value of duty cycle D , the output voltage (battery voltage V_{bat}) will be constant. The block diagram of this technique is shown in Figure 8.

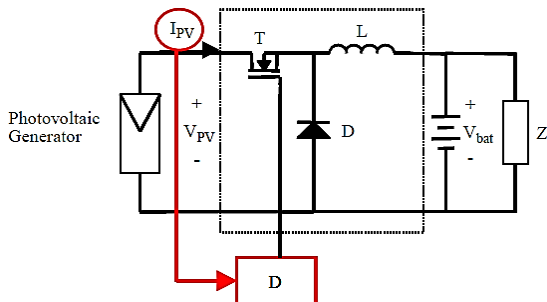


Figure 8. Block diagram of the only-current method [24].

In the case of buck converter, the output voltage (battery voltage) can be given as shown:

$$V_{bat} = \frac{T_{on}}{T} V_{PV} = D \cdot V_{PV} \tag{4}$$

where, T is the period time and T_{on} is the the duration of the controlled switch is ON.

The input power of the converter can be determined as:

$$P_{in} = V_{PV} \cdot I_{PV} = V_{bat} \cdot \frac{I_{PV}}{D} = V_{bat} \cdot P_{BUCK}^* \tag{5}$$

Where

$$P_{BUCK}^* = \frac{I_{PV}}{D} \tag{6}$$

According to the algorithm of Figure 9, four cases can be presented in Table 1.

$$\Delta P^* = P^*(t + \Delta t) - P^* \tag{7}$$

$$\Delta D = D(t + \Delta t) - D(t) \tag{8}$$

It can be seen from the algorithm that, after computing the present and the past data of P_{BUCK}^* , and based on the equation (8), the controller decides whether to reduce or enhance the duty-cycle ratio. This tracking process will be repeated until the MPP is reached [10].

The advantage of this method is the PV module current is the only control variable. Moreover, this method has a good efficiency even under different atmospheric conditions and can be implemented with any type of DC-DC converter not just with a buck converter [23].

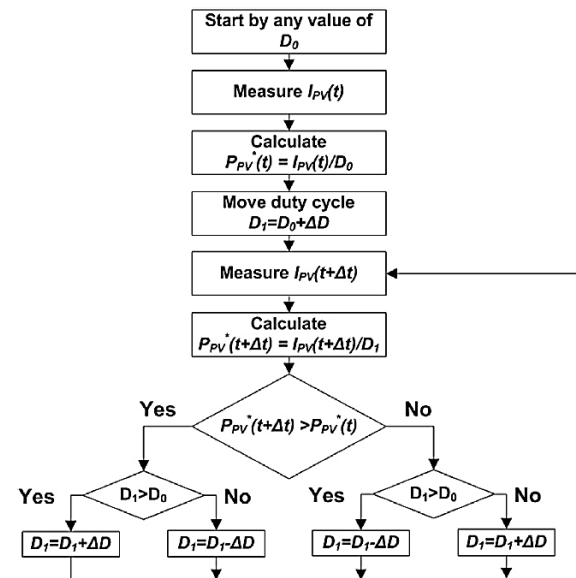


Figure 9. Flowchart of the only-current photovoltaic method [10].

Table 1. Decision the change in the duty cycle after measuring and storing the past and the present information [23].

Case	ΔP	ΔD	Following step
1	> 0	> 0	$+ \Delta D1$
2	> 0	< 0	$- \Delta D1$
3	< 0	> 0	$- \Delta D2$
4	< 0	< 0	$+ \Delta D2$

2.10 PV Output Senseless (POS) Control Technique

In the POS MPPT technique, the load voltage is omitted, and the load current is the only significant component. As known, the load power is related to the harvested power from the PV module, and multiplying the voltage with the current is equal to a load power. Therefore, increasing the load current leads to an increase in the load power and from there increases the generated power by the PV module. This simple algorithm (shown in Figure 10) can be applied to all PV generation systems. The POS MPPT technique finds the MPP by comparing the duty cycle with the load current value [25, 26]. The details of the POS algorithm are presented in Table 2 and Figure 11.

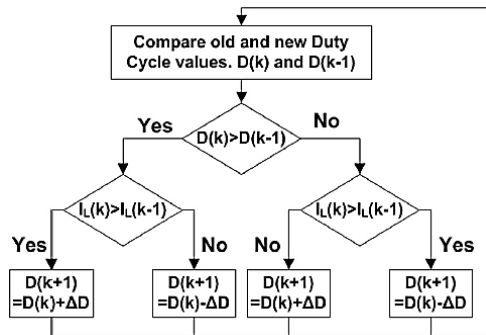


Figure 10. Flowchart of the POS MPPT technique [10].

Table 2. A conceptual explanation of POS MPPT technique [25].

Track	Duty ratio	Current (I)	Δ Duty ratio
1 (V ₀ → V ₁)	(-)	(+)	(-)
2 (V ₁ → V ₂)	(-)	(-)	(+)
3 (V ₂ → V ₃)	(+)	(+)	(+)
4 (V ₃ → V ₁)	(+)	(-)	(-)

From Figure 11: in track 1, if the value of the duty cycle decreases, the generated voltage by the PV module moves from V₀ to V₁, and the generated power increases from P₀ to P₁. In track 2, the value of the duty cycle will decrease, the generated voltage moves from V₁ to V₂ and the generated power decreases from P₁ to P₂. In track 3, if the duty cycle increases, the generated voltage decreases from V₂ to V₃ and the generated power increases from P₂ to P₃. In track 4, the duty cycle will increase, the generated voltage decreases from V₃ to V₁ and the generated power decreases from P₃ to P₁. Therefore, the duty cycle will decrease, and all of these steps will be repeated until POS MPPT reaches the MPP [25].

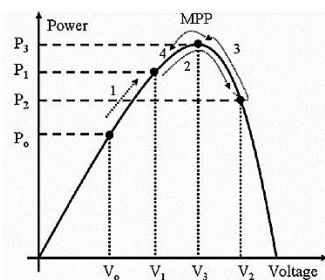


Figure 11. The explanation of POS MPPT technique [25].

This technique is very useful in extracting maximum power from the PV module with the feedback of only the

load current. Moreover, it can be operated effectively on a large scale PV generation system.

2.11 Perturb and Observe (P&O) Method

Among all the papers reviewed, significant attention was directed towards the Perturb and Observe (P&O) method, which is considered one of the most commonly used techniques for tracking the Maximum Power Point (MPP). This method operates on the principle of perturbing the duty cycle value and observing the resulting power extracted from the PV module [27]. In each cycle of the P&O method, the control unit calculates the power generated by the PV module, then adjusts the duty cycle and monitors the power variation. If the extracted power increases, the subsequent perturbation is made in the same direction until the MPP is reached. Conversely, if the extracted power decreases, the next perturbation is reversed [28]. The basic principle of the P & O algorithm is summed up in Table 3 and shown in Figure 12. The block diagram of this technique is illustrated in Figure 13.

Table 3. A Summary of the P&O method.

Perturbation	Change in Power	Next Perturbation
Positive	Positive	Positive
Positive	Negative	Negative
Negative	Positive	Negative
Negative	Negative	Positive

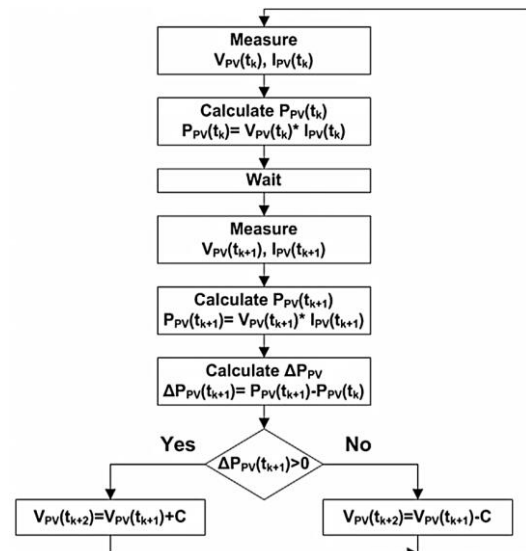


Figure 12. The flowchart of the P&O algorithm [10].

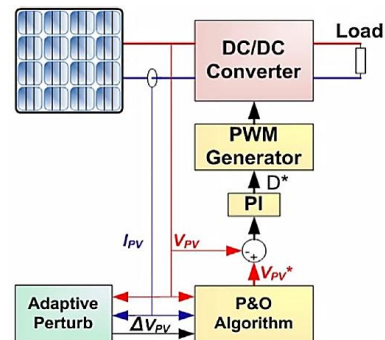


Figure 13. The block diagram of the P&O method [10].

After reaching the MPP, the operating point starts oscillating around the MPP leading to loss of power. With the aim of reducing the steady-state oscillation, the perturbation step size must be minimized. However, small step values cause a low speed of tracking the MPP. Using a two-stage algorithm that exhibits a large step value in the first stage and a low step value in the later stage is considered a solution to the problem between the faster tracking and steady-state oscillations [10].

However, this method suffers another drawback. This method fails under a swift change in atmospheric conditions as shown in Figure 14. Assuming that the operating point is A, if the atmospheric conditions stay nearly constant, the next perturbation will move the operating point to B and, due to reduction in power, the following perturbation will be reversed. However, within one iteration, if the atmospheric conditions change and displace the power curve from P_1 to P_2 , the operating point will shift from A to C. This will appear as an increase in power and the next perturbation will be kept in the same direction resulting in loss of power [21, 29].

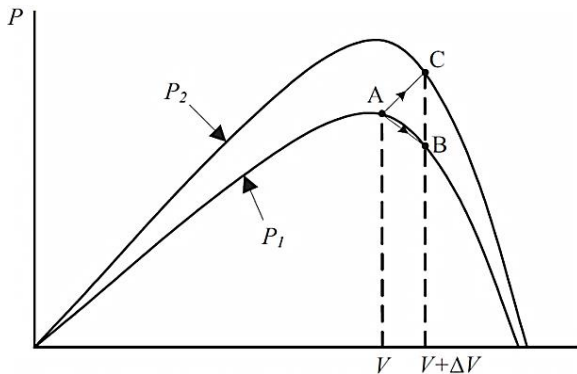


Figure 14. Divergence of the P&O from MPP [21].

The vital advantage of this method is that the characteristics of the PV module are not required, and it can be implemented for all types of PV modules. Two sensors, one for voltage and the other for current, are used to compute the extracted power from the PV module. DSPs or microprocessors are used in this technique.

2.12 Three-Point Weight Comparison Method

In the P&O algorithm, in order to monitor the change in power and determine whether to increase or decrease the subsequent duty cycle, the values of power at the current operating point and the subsequent operating point are compared. Additionally, the operating point in the P&O algorithm oscillates around the MPP resulting in a loss of the extracted power from the PV module. Therefore, to avoid the loss of power under rapid atmospheric condition changes, the three-point weight comparison algorithm was proposed [10, 30]. This algorithm runs periodically by perturbing the duty cycle which is applied on the DC-DC converter and comparing the PV module output power on three points on the P-V curve. The three points are as follows:

- A: The current operating point.
- B: perturbed positively from point A.
- C: perturbed negatively from point A.

To reach the MPP, nine possible states should be carried out in the control unit as depicted in Figure 15. The procedures of the algorithm are as follows:

- 1) If the power at point B is greater than or equal to the power at point A the status is assigned positively weighted; otherwise if the power at point B is smaller, the status is negatively weighted.
- 2) If the power at point C is greater than or equal to the power at point A, the status is negatively weighted; otherwise, the status is positively weighted.
- 3) According to the comparison of the three points, if two cases are negatively weighted, the duty cycle will be decreased in the next iteration; otherwise when two cases are positively weighted, the duty cycle will be increased. In other cases, if one is negatively weighted and the other is positively weighted, the MPP is reached and the duty cycle should not be changed. A flowchart of this algorithm is shown in Figure 16 [31].

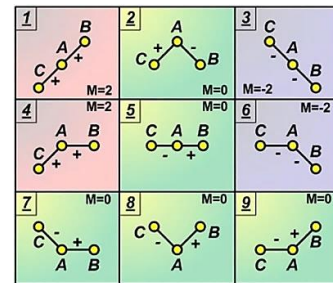


Figure 15. Possible states of the three-point weight comparison algorithm [10].

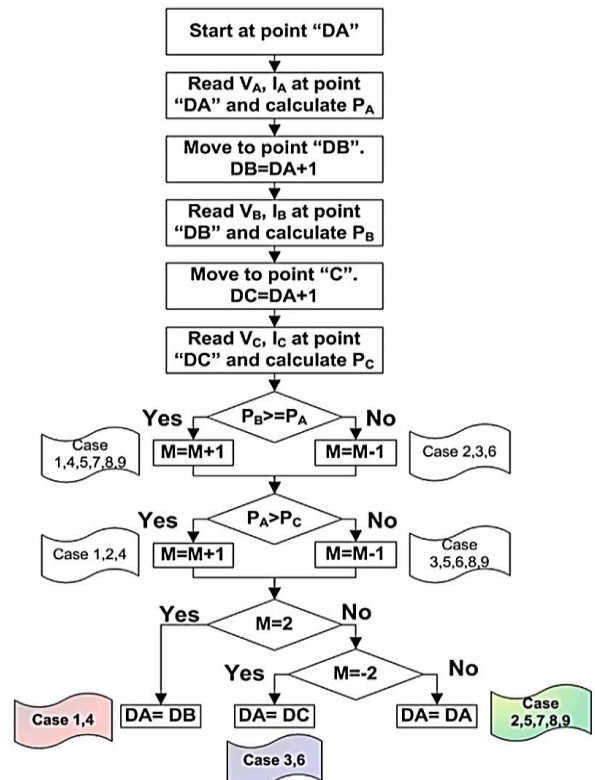


Figure 16. The flowchart of the three-point weight comparison algorithm [10].

2.13 On-line MPP search algorithm

In this algorithm, shown in Figure 17, the reference maximum power is determined and compared with the current power [10]. The difference between the two values is called the maximum power error. If the maximum power error is zero, the MPP is reached [32].

At first, the reference values of the maximum power, P_{ref} , and reference current, I_{ref} , are set to zero, and the reference voltage, V_{ref} , is equated to the open-circuit voltage V_{oc} of the PV module. At each iteration, the difference, P_{error} , between the reference power, P_{ref} , and the current operating power, P_{actual} , are computed and compared with the assumed error, $P_{tolerance}$. If the difference, P_{error} , is smaller than the assumed error, $P_{tolerance}$, the initial values, P_{ref} , I_{ref} and V_{ref} are reassigned by, $P_{actual,ref}$, $I_{actual,ref}$ and $V_{actual,ref}$, respectively, and used as reference values for the next iteration. If the difference, P_{error} , is greater than the assumed error, $P_{tolerance}$, a new MPP will be searched by the algorithm. If the current operating power, P_{actual} , is greater than the reference power, P_{ref} , then the operating values, P_{actual} , I_{actual} , and V_{actual} are reassigned by, $P_{actual,ref}$, $I_{actual,ref}$ and $V_{actual,ref}$, respectively, and used as reference values for the next iteration. If the operating power, P_{actual} , is smaller than the reference power, P_{ref} , then the operating current, I_{actual} , and voltage, V_{actual} , will be compared with I_{ref} and V_{ref} , respectively. If the operating current I_{actual} is greater than I_{ref} or the operating voltage is smaller than V_{ref} , then the operating values, P_{actual} , I_{actual} , and V_{actual} are reassigned by, $P_{actual,ref}$, $I_{actual,ref}$ and $V_{actual,ref}$, respectively [33].

The success of this algorithm in capturing the MPP is related to the operating power of the load P_{actual} . If P_{actual} is small, the algorithm will fail to find the MPP. To avoid that, extra loads must be connected to increase the operating power so MPP can be reached. This algorithm can find the new MPP under rapidly changing atmospheric conditions.

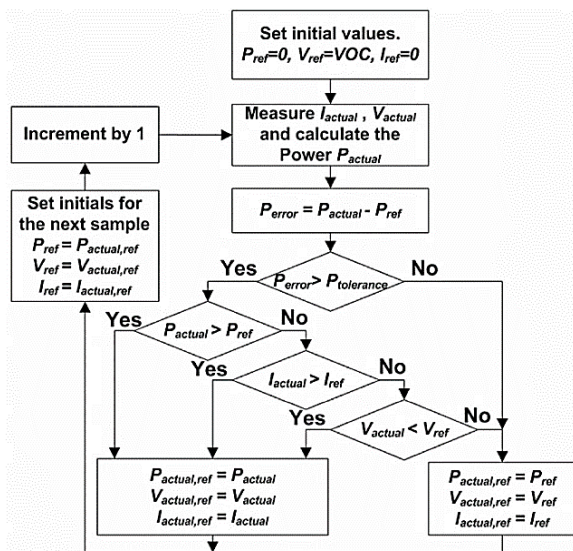


Figure 17. The flowchart of the on-line MPP search algorithm [10].

2.14 DC-Link Capacitor Droop Control

This method is particularly developed to be used with a PV system that is connected in parallel with a DC to AC inverter [10], as illustrated in Figure 18. Assuming that a boost converter is connected between the PV module and the inverter, the duty cycle on an ideal boost converter is given as:

$$D = 1 - \frac{V_{PV}}{V_{link}} \tag{9}$$

Where:

V_{PV} is the input voltage of the boost converter.

V_{link} is the output voltage of the boost converter, which is the voltage across the DC-link.

The control process in this MPPT method is based on discerning the voltage drop across the DC-link voltage V_{link} [34]. If the V_{link} is kept constant alongside increasing the current passing across the AC inverter, this leads to an increase in the power coming from the boost converter and consequently increases the extracted power from the PV module. When the required power by the inverter surpasses the maximum available power from the PV module, the DC-link voltage V_{link} begins dropping. Right before that point, the system works at the MPP and the current control command I_{peak} of the AC inverter is at its maximum value. The ac system line current is fed back to prevent V_{link} from drooping and the duty cycle is optimized to fetch I_{peak} to its maximum value; consequently, MPPT is achieved. The main drawback of this technique is the low response. This is because its response relies directly on the response of the dc voltage control loop of the AC inverter [35, 36].

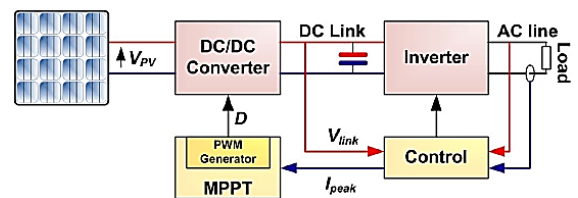


Figure 18. Topology of a DC-link capacitor droop control [10].

2.15 MPPT with a Variable Inductor

In this technique, a buck converter is used to make the load resistance equal to the resistance of the PV panel [37]. In this case, according to the max power transfer theorem, the maximum available power will be transferred from the PV panel to the load. The load resistance R_L is matched to the PV panel resistance R_{PV} by controlling the duty cycle D , R_{PV} is given as:

$$R_{PV} = \frac{V_{PV}}{I_{PV}} = \frac{V_L}{I_L D^2} = \frac{R_L}{D^2} \tag{10}$$

To satisfy the last equation, the buck converter must operate in the continuous current mode (CCM). During CCM the minimum inductance in a buck converter is given as:

$$L_{min} = \frac{R_L(1-D)}{2.f_s} \quad (11)$$

where, f_s is the switching frequency.

The relation between the input and the output current of a buck converter is given as:

$$I_{PV} = D \cdot I_L \quad (12)$$

By combining the last equations (10), (11) and (12), the relationship between L_{min} and the I_{PV} is given as:

$$L_{min} = \frac{D(1-D)V_{PV}}{2.f_s I_L} = \frac{D^2(1-D)V_{PV}}{2.f_s I_{PV}} \quad (13)$$

By assuming that the voltage does not change over the full range of the solar irradiance, the minimum inductance, which keeps the buck converter in the CMM, becomes related to the load current and the duty cycle or the PV current and the duty cycle [38].

2.16 Current Sweep Method

This method depends on determining the derivative of the PV array output power with regards to the array output current while the array output current is adapted as a decaying exponential sweep function [10]. In this method, a sweep waveform is used in order to obtain the I-V characteristic curve of the PV array, and this curve will be updated at fixed time periods [39]. Then, from the I-V characteristic curve, the V_{MPP} can be computed during the same periods. The current sweep waveform can be calibrated as a predefined function of time.

$$I_{PV}(t) = f(t) \quad (14)$$

The function $f(t)$ selected for the sweep waveform is directly proportional to its derivative as follows:

$$f(t) = k \cdot \frac{df(t)}{dt} \quad (15)$$

where, k is a proportionality constant. Along this sweep waveform the PV array power is given by:

$$P_{PV}(t) = V_{PV}(t) \cdot I_{PV}(t) = V_{PV}(t) \cdot f(t) \quad (16)$$

As known at MPP the derivative of $P_{PV}(t)$ is zero.

$$\frac{dP_{PV}(t)}{dt} = V_{PV}(t) \cdot \frac{df(t)}{dt} + f(t) \cdot \frac{dV_{PV}(t)}{dt} = 0 \quad (17)$$

Substituting $f(t)$ in the last equation gives:

$$\frac{dP_{PV}(t)}{dt} = \left[V_{PV}(t) + k \cdot \frac{dV_{PV}(t)}{dt} \right] \cdot \frac{df(t)}{dt} = 0 \quad (18)$$

The solution of the differential equation in (15) is given as:

$$f(t) = C \cdot e^{t/k} \quad (19)$$

where, C is the arbitrary constant which is selected to be equal to the maximum current of the PV array I_{max} . If k is selected to be negative, that leads to a decrease in exponential function with time constant $\tau = k$.

$$f(t) = I_{max} \cdot e^{-t/\tau} \quad (20)$$

By using some current discharging through a capacitor, the current in (20) can be easily obtained.

By dividing both sides of the (18) equation on $\frac{df(t)}{dt}$ with $f(t) = I_{PV}(t)$:

$$\frac{dP_{PV}(t)}{df(t)} = \frac{dP_{PV}(t)}{dI_{PV}(t)} = V_{PV}(t) + k \cdot \frac{dV_{PV}(t)}{dt} = 0 \quad (21)$$

Once V_{MPP} is calculated after the current sweep, the equation (21) is used to verify whether the MPP has been reached. This technique needs about 50 ms to reach MPP, resulting in some power loss. Therefore, this MPPT method is suitable if the tracking unit consumes power lower than the increase in power that it can extract from the PV array [40].

2.17 Incremental Conductance (IC) Technique

This technique depends on calculating the differential of the PV power to PV voltage to determine the location of the operating point [41], where the differential is zero at the MPP, positive on the left of the MPP and negative on the right of the MPP, as given by Hussein et al. [42]:

$$\begin{aligned} \frac{dP_{PV}}{dV_{PV}} &= 0, \text{ at MPP.} \\ \frac{dP_{PV}}{dV_{PV}} &> 0, \text{ left of MPP.} \\ \frac{dP_{PV}}{dV_{PV}} &< 0, \text{ right of MPP.} \end{aligned} \quad (22)$$

Since:

$$\frac{dP_{PV}}{dV_{PV}} = \frac{d(V_{PV} \cdot I_{PV})}{dV_{PV}} = I_{PV} + V_{PV} \cdot \frac{dI_{PV}}{dV_{PV}} \quad (23)$$

After measuring the values of V_{PV} and I_{PV} at different instants, the incremental variations, dV_{PV} and dI_{PV} , can be approached by the increments of both parameters ΔV_{PV} and ΔI_{PV} respectively. Therefore, parameters can be given as:

$$dV_{PV} \cong \Delta V_{PV} = V_{PV}(t) - V_{PV}(t - \Delta t) \quad (24)$$

$$dI_{PV} \cong \Delta I_{PV} = I_{PV}(t) - I_{PV}(t - \Delta t) \quad (25)$$

$$\frac{dP_{PV}}{dV_{PV}} \cong I_{PV} + V_{PV} \cdot \frac{\Delta I_{PV}}{\Delta V_{PV}} \quad (26)$$

The basic principle of the incremental conductance method can be rewritten as:

$$\begin{aligned} \frac{\Delta I_{PV}}{\Delta V_{PV}} &= -\frac{I_{PV}}{V_{PV}}, \text{ at MPP.} \\ \frac{\Delta I_{PV}}{\Delta V_{PV}} &> -\frac{I_{PV}}{V_{PV}}, \text{ left of MPP.} \\ \frac{\Delta I_{PV}}{\Delta V_{PV}} &< -\frac{I_{PV}}{V_{PV}}, \text{ right of MPP.} \end{aligned} \quad (27)$$

As shown in the flowchart in Figure 19, by comparing the incremental conductance ($\Delta I/\Delta V$) to the instantaneous conductance (I/V), the MPP can be reached [43]. The PV module is forced to operate at the reference voltage V_{ref} , where at the MPP, $V_{ref} = V_{MPP}$. Once the MPP is captured, the operating point will be stabilized at the MPP unless a change in PV current I_{PV} is noted, implying a change in atmospheric conditions; subsequently, there will be a change in the MPP. In this case, the algorithm decreases or increases the reference voltage V_{ref} with a view to reaching the new MPP [44].

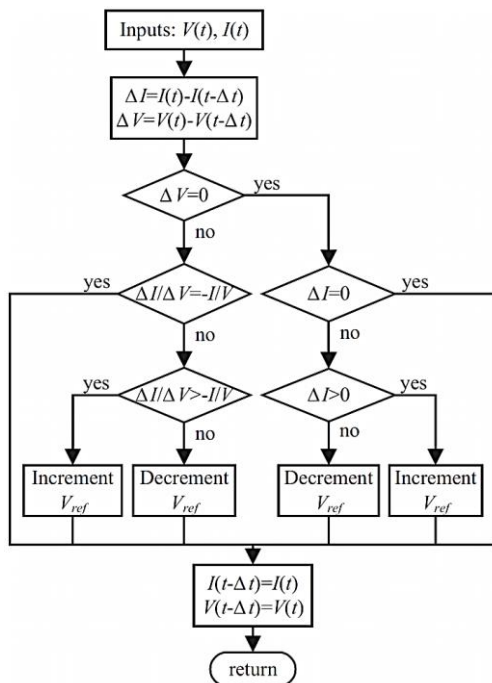


Figure 19. Incremental conductance algorithm flowchart [21].

How fast the MPP can be reached is specified by the increment size. With greater increments, rapid attainment of the MPP can be achieved but the operating point might not be at the MPP exactly and oscillate around it, so there is a tradeoff [45]. Two stages of tracking can be proposed to solve this drawback, in the first stage the operating point is brought near the MPP and then in the second stage the incremental conductance method is employed to track the exact MPP.

2.18 IMPP and VMPP Computation Technique

This technique is based on computing the current and voltage at the MPP, (V_{MPP}, I_{MPP}), from the standard PV current equation, including the irradiance level and ambient temperature. Once calculated, the PV module will be forced to operate at the MPP by using a feedback control loop. Then, the PV array current I_{PV} and voltage V_{PV} at the insolation E and temperature T are given as:

$$I_{PV} = \left[I_S + I_{SC} \left(\frac{E}{E_{STC}} - 1 \right) + \mu(T - T_{STC}) \right] \cdot N_P \quad (28)$$

$$V_{PV} = \left[V_S + \beta \cdot (T - T_{STC}) - R_S \left(\frac{1}{N_P} - I_S \right) - \frac{K \cdot I_{PV}}{N_P} (T - T_{STC}) \right] \cdot N_S \quad (29)$$

Where I_S & V_S are the output current and voltage of the PV module at the standard test conditions (STC). E_{STC} is the standard solar insolation ($1\text{kW}/\text{m}^2$), and T_{STC} is the standard module temperature (25°C). Moreover, I_{SC} is the short circuit current, μ is the temperature coefficient of I_{SC} , β is the temperature coefficient of V_{OC} , R_S is a series resistance of the module and K is the curve correction factor. N_P is the number of parallel-connected modules and N_S is the number of series-connected modules [46].

The output power P_{PV} is calculated as:

$$P_{PV} = V_{PV} \cdot I_{PV} = I_{PV} \cdot \left[V_S + \beta(T - T_{STC}) + R_S \cdot I_S - \frac{I_{PV}}{N_P} \cdot [R_S + K \cdot (T - T_{STC})] \right] \cdot N_S \quad (30)$$

The current I_{MPP} and the voltage V_{MPP} at the maximum power point are calculated by differentiating the P_{PV} with respect to the I_{PV} :

$$I_{MPP} = \frac{N_P}{2} \frac{V_S + \beta \cdot (T - T_{STC}) + R_S I_S}{R_S + K(T - T_{STC})} \quad (31)$$

$$V_{MPP} = \frac{N_S}{2} \cdot V_S + \beta \cdot (T - T_{STC}) + R_S \cdot I_S \quad (32)$$

It is notable that the last equations contain the temperature T and do not contain the insolation E . Usually, temperature affects the PV module voltage, and the insolation affects the PV module current. However, the equation of the output power P_{PV} contains the current I_{PV} , and I_{PV} is affected by the insolation E . Therefore, the output power P_{PV} is affected by the insolation E . As a result, even though insolation E does not appear in the equations of the V_{MPP} & I_{MPP} , those equations have effects on insolation E .

As pointed in the equations of the V_{MPP} & I_{MPP} , the maximum power point can be predicted with the module characteristics, and these module characteristics are computed by PV makers. At that time, if there is any difference between the real operating point and the predicted operating point, it indicates that there will be some error in the system. Therefore, this technique can be used for the error diagnosis of the PV system [10]

2.19 Ripple correlation control (RCC)

Once a DC-DC converter is connected to the PV array, the switching action of the power converter forces the current and voltage ripple on the PV array. As a result, the PV array output power will also be submissive to ripple. The MPPT in ripple correlation control is achieved by making use of ripple [47].

In this technique, in order to make the power gradient zero; MPP is reached; the time derivative of the time-varying PV power P_{PV} with the time derivative of the time-varying PV voltage V_{PV} or current I_{PV} is correlated.

If the voltage V_{PV} or the current I_{PV} is increasing ($V_{PV} > 0$ & $I_{PV} > 0$) and the power is increasing ($\dot{P}_{PV} > 0$), then the operating point is beneath the MPP; (on the left side of the P-V curve); ($I < I_{MPP}$ or $V < V_{MPP}$). On the other side, if the voltage V_{PV} or the current I_{PV} is increasing ($V_{PV} > 0$ & $I_{PV} > 0$) and the power is decreasing ($\dot{P}_{PV} < 0$), then the operating point is over the MPP; (on the right side of the P-V curve); ($I > I_{MPP}$ or $V > V_{MPP}$). If the power ($\dot{P}_{PV} = 0$), then the MPP is reached [48].

This method can be achieved by a simple and inexpensive analog circuit. In addition, RCC does not depend on the PV array characteristics, so it can be adapted to different PV systems straightforwardly.

2.20 Fuzzy Logic Control Based MPPT

Over the past decade, the fuzzy logic control method has become common for MPPT since it has many advantages of handling nonlinearity, not requiring an accurate mathematical model, and working with inaccurate inputs [49]. Generally, fuzzy logic control comprises three stages: fuzzification, rule base table lookup, and defuzzification. In the fuzzification stage and based on a membership function, shown in Figure 20, numerical input variables are changed into linguistic variables. In general, five fuzzy levels are used: NB (Negative Big), NS (Negative Small), ZE (Zero), PS (Positive Small), and PB (Positive Big). To increase accuracy, more fuzzy levels can be used [50, 51].

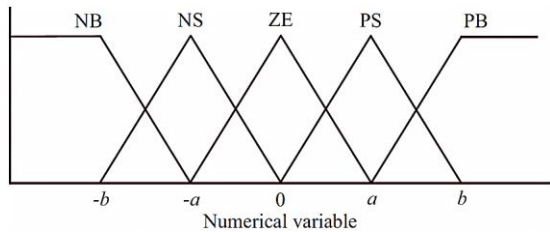


Figure 20. Membership function for inputs and output of fuzzy logic controller [21].

In Figure 20, a and b represent the range of the numerical variable values. Usually, the error E and the change in error ΔE are used as inputs to the MPPT fuzzy logic controller, and the user has the choice of how to compute them.

$$E(n) = \frac{P(n) - P(n-1)}{V(n) - V(n-1)} \tag{33}$$

$$\Delta E = E(n) - E(n - 1) \tag{34}$$

After calculating E and ΔE , they will be changed into linguistic variables and the output of the fuzzy logic controller, which is a change in duty cycle ΔD , can be found in the rule base, which is shown in Table 4.

The change in duty cycle ΔD for the various groups of E and ΔE is determined according to the type of power

converter being used and the knowledge of the user. From Table 4, for instance, if the operating point is at the far-right end of the MPP, that is the E is NB, and ΔE is ZE, then with a view to reaching the MPP, a large decrease in duty cycle is required, that is ΔD must be NB.

Table 4. The fuzzy logic rule base [21].

ΔE E	NB	NS	ZE	PS	PB
NB	ZE	ZE	NB	NB	NB
NS	ZE	ZE	NS	NS	NS
ZE	NS	ZE	ZE	ZE	PS
PS	PS	PS	PS	ZE	ZE
PB	PB	PB	PB	ZE	ZE

During the defuzzification stage, the linguistic variables are converted to numerical variables depending on the membership function, as shown in Figure 20. This generates a control signal used to converge the operating point to the MPP.

This method performs well under varying atmospheric conditions. However, its effectiveness is based substantially on the prior experience of the user [51].

2.21 Neural Network Based MPPT

This technique is well adapted for microcontrollers. The neural network typically consists of three layers: input, hidden, and output layers as illustrated in Figure 21. The input variables of the neural network can be the characteristics of the PV module being used or the atmospheric conditions. The output variable is the duty cycle used as a control signal to make the operating point at the MPP. The accuracy of the technique in tracking the MPP relies on the algorithm being used and how well the neural network was trained [52]. The link between nodes i and j is labelled as having a weight of w_{ij} . The more the w_{ij} 's are carefully determined through the training process, the more the MPP can be accurately tracked. In accordance with this, the right weight for every node is obtained by testing and recording the PV parameters over months or years. The disadvantage of this technique is that it needs to be particularly trained for the PV module which is being used. Moreover, the features of the PV module change with time, which means that the neural network should be periodically trained to accurately track the MPP [53].

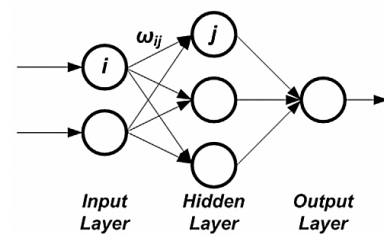


Figure 21. Neural network layers [21].

3 Characteristics During Non-Uniform Irradiance Condition

As is known, the I-V characteristic of a PV panel is directly affected by the change in atmospheric conditions;

in particular, the change of irradiance and temperature. When the PV panel receives a uniform irradiance, the P-V curve exhibits only one MPP which can be captured and tracked by using any one of the conventional MPPT techniques.

Due to many factors such as passing clouds, the shadow cast by the adjacent buildings, trees, bird droppings, dust deposition, etc. the PV panels do not receive uniform irradiance during the daytime. When the solar panel is exposed to partial shading, as shown in Figure 22, the current produced by the shaded cell is lower than the current produced by the unshaded cells, which will lead to negative bias in the shaded cells and instead of generating power will start consuming power leading to a loss in the total output power [54]. The power consumption in the individual shaded cell will lead to overheating which negatively affects surrounding cells. The overheating generates thermal stress on the whole PV panel and hot spot phenomena occurs [55].

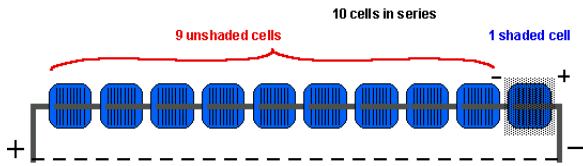


Figure 22. PV string during non-uniform irradiance pattern

To protect the shaded cell from the thermal destruction, (hot spot phenomena) as shown in Figure 23, bypass diodes should be integrated in parallel within the PV panel as shown in Figure 24.

Due to the presence of the bypass diodes, used to block hot spot formation, multiple maximum power points in PV characteristic occurs, as shown in Figure 25 [54].

In this case, conventional MPPT techniques would predominantly not succeed in tracking the appropriate global maximum power point (GMPP) and extra power losses result [56]. For that reason, many new MPPT optimizations have been proposed to address this issue which occurs during partial shading conditions.



Figure 23. Hot spot phenomena

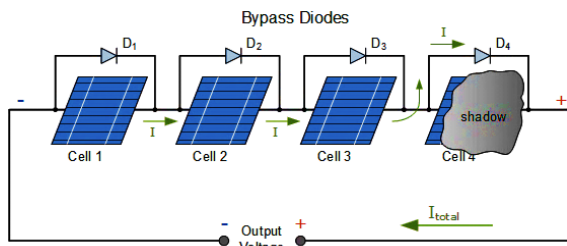


Figure 24. Bypass diodes connected in parallel within the PV panel [57].

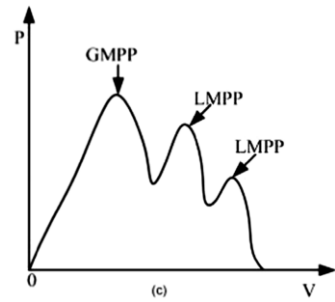


Figure 25. The P-V characteristic under non-uniform irradiance pattern [54].

4 Modern MPPT Optimizations

To overcome the drawbacks of the conventional MPPT techniques and address the PSCs issue, many modern MPPT techniques have been proposed. In this section, the most commonly used techniques are summarized.

4.1 Grey Wolf Optimization

It is inspired by the attack approach used by grey wolves during hunting. This technique has the capability of mimicking the hierarchy leadership as well as the hunting efficiency of grey wolves. With the intention of achieving the effective leadership hierarchy, one group of grey wolves is employed, this group contains four kinds of grey wolves; they are alpha (α), beta (β), delta (δ) and omega (ω).

The optimization consists of three procedures; hunting, chasing and tracking of the prey then encircling the prey and attacking it [58, 59]. The hunting mechanism of the grey wolves is led by α clans which are considered leaders and are followed by the β clans. During the hunting process, the wounded wolves are taken care of by the δ and ω clans. This hunting mechanism is employed in the PV system in order to handle the problem of multiple MPPs where the prey represents GMPP in this case. With a view to holding the duty cycle constant at GMPP and reducing steady-state oscillations, the optimization is combined with the direct duty cycle control [60]. The following equations are used to model the hunting technique of grey wolves:

$$\vec{E} = \vec{C} \cdot \overline{X_p(t)} - \overline{X_p(t)} \tag{35}$$

$$\overline{X(t+1)} = \overline{X_p(t)} - \vec{F} \cdot \vec{E} \tag{36}$$

where, t refers to the present iteration; C , E and F are called the coefficient vectors. The position vector of the prey is symbolized by X_p whereas the position vector for the grey wolf is symbolized by X .

By using the following equations, vectors F and C are calculated:

$$\vec{F} = 2\vec{a} \cdot \vec{r}_1 - \vec{a} \tag{37}$$

$$\vec{C} = 2 \cdot \vec{r}_2 \tag{38}$$

The value of α is reduced linearly from 2 to 0, also the vector values of \vec{r}_1 & \vec{r}_2 are in [0, 1]. In MPPT applications, the grey wolf represents duty cycle D. Thus, the equation (36) is adjusted as equation (39) and the fitness function of the optimization is calculated by equation (40).

$$D_i(k + 1) = D_i(k) - F \cdot E \tag{39}$$

$$P(D_i^k) > P(D_i^{k-1}) \tag{40}$$

where P refers to power; D refers to duty cycle; i represents the number of grey wolves; k denotes the number of iterations. One of the most important advantages of this optimization is eliminating the steady-state oscillations [54].

4.2 Ant Colony Optimizations

This optimization is based on the behavior of ants searching for food [61, 62]. During the food search process, the ants try to find the optimal paths. In this technique, a fitness function $f(k)$ is used to represent the output power, $f(k) = I(k) \times V(k)$ and the ants denote the duty cycle. This technique consists of three steps as shown in Figure 26:

- 1) Initialization and distribution of ants according to the fitness function.
- 2) Limiting the search interval.
- 3) Ants move towards the optimal point, the MPP.

After finding the optimal path, the technique provides the proper duty cycle, which is used to drive the DC-DC converter [63, 64].

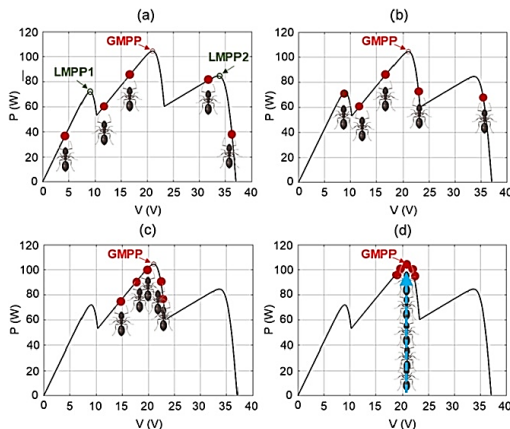


Figure 26. The action steps of the ant colony technique [65].

4.3 Bee Colony Optimization

This technique is considered one of the simplest techniques since it utilizes very few controlled parameters and the initial conditions of the system do not affect the algorithm convergence criteria [66]. It is inspired by the behavior of bees searching for food. As is widely known, the bee colony is divided into three main groups- they are the employed bees, which constantly search the food sources or benefit from the food sources, onlooker bees, which wait in the hive and their role are restricted to making the decisions to choose the food source. The last

group is the scouts, which conduct a random search to find a new food source. In order to get the optimal solution in a short time, the three groups communicate and coordinate together [67, 68]. In MPPT applications, the food position represents the duty cycle, and the food source represents the maximum power. With the aim of implementing this technique in MPPT applications, the duty cycle used to drive the DC-DC converter is calculated as follows:

$$\vec{F} = 2\vec{a} \cdot \vec{r}_1 - \vec{a} \tag{41}$$

$$\vec{C} = 2 \cdot \vec{r}_2 \tag{42}$$

Here, D_e is the current value of duty cycle, D_{min} is the minimum value of duty cycle, D_{max} is the maximum value of duty cycle, Θ_e is a constant ranging between (-1, 1) and D_k is the previous value of the duty cycle [68]. The technique was accurate and efficient in finding the GMPP under partial shading conditions.

4.4 Particle Swarm Optimization (PSO)

Among the most popular bio-inspired computation algorithms, PSO is inspired by the social behavior of bird flocking and fish schooling. With different capabilities of reaching optimum solutions, it is good for dealing with problems on which a point or surface represent the best solution [69]. In this algorithm, several cooperative particles are used to conduct the research of the optimal point. If there is available information regarding the location of the GMPP in the search space, the initial position of the particles can be in a fixed position; otherwise, they will be spread in the space randomly. The position of the particle represents the value of the duty cycle [70]. In this algorithm, each particle conducts the search process and collects information, then they exchange the information obtained in their respective search. After that, the particles move toward the optimal point by following the best performing particle. In this way, each particle ultimately evolves to an optimal or close to the optimal solution. Using a large number of particles will increase the accuracy in capturing GMPP; however, that will make the convergence process to the GMPP slow [71, 72]. Although PSO is simple in implementation and able to achieve GMPPT, it is computationally intensive and time-consuming which gradually reduces search accuracy.

4.5 Deterministic Particle Swarm Optimization (DPSO)

To improve the tracking capability and reduce the problem of random searches, this optimization was modified from conventional particle swarm optimization. In conventional optimization, more iterations will be required to reach the final solution when the change in the duty cycle for two sequential iterations is low. In addition, if the particle is far from the desired point, then a large change in convergence speed is needed, which may make the particle move away from the GMPP. In DPSO, by eliminating the acceleration factor in the convergence speed equation and restricting the convergence speed factor according to the range between two peaks, the

DPSO becomes simpler than the conventional optimization. The optimization has two modes, global mode and local mode. During the partial shading condition, the global mode becomes active. In this case, the algorithm changes into DPSO subroutine, and variable step size perturbation is used during the local mode [72, 73]. The range of duty cycle in global mode is determined as follows:

$$D_{min} = \frac{\sqrt{\eta R_{Lmin}}}{\sqrt{R_{PVmax} + \sqrt{\eta R_{Lmin}}}} \tag{43}$$

$$D_{max} = \frac{\sqrt{\eta R_{Lmax}}}{\sqrt{R_{PVmin} + \sqrt{\eta R_{Lmax}}}} \tag{44}$$

where D_{min} & D_{max} denote the minimum and the maximum values of the duty cycle respectively. η refers to the efficiency of the DC-DC converter being used. R_{Lmin} & R_{Lmax} denote the minimum and the maximum values of the load. $R_{PV min}$ & $R_{PV max}$ refer to the reflective impedances of the PV panels [54].

4.6 Switched PV Approach

In this approach, each string in the PV array is equally divided into two parts; the parts are connected together by using two diodes and one controlled switch, as shown in Figure 27.(a). The operating process of this technique has three stages:

- 1) Stage 1: switches are closed, in this case, the highest output voltage is (V_{OC}) and the highest output current is ($n.I_{SC}$), where n is the number of parallel-connected strings.
- 2) Stage 2: switches are opened, in this case, the highest output voltage is ($0.5V_{OC}$) and the highest output current is ($2.n.I_{SC}$).
- 3) Stage 3: Selecting the State: MPPT algorithm will activate state1, searches GMPP1. Afterwards, activates state 2, searches for GMPP2 as shown in Figure 27.(b). After that, the MPPT algorithm will compare the values of obtained powers and then decide to switch the system to the state providing increased power [74].

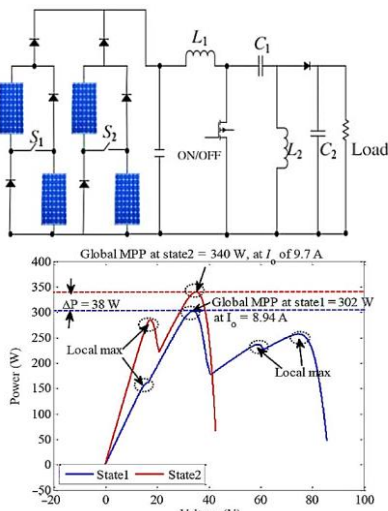


Figure 27. (a) The schematic diagram of the Switched PV technique, (b) Power-voltage characteristic in both states [74].

4.7 A Novel MPPT Method Based on Irradiance Measurement

In the proposed approach, the photodiodes are used as light sensors as shown in Figure 28; the presence of photodiodes gives an innovation feature to this method. The signals provided by the photodiodes allow the algorithm to work properly in spite of the changes in the climatic conditions. The operating process of the proposed method consists of three stages:

- 1) Detect partial shading.
- 2) Find the region of the GMPP.
- 3) Tracking the GMPP by using a conventional technique.

When the photodiodes detect partial shading, the algorithm waits for 30 s to discover whether the shadow is transient or permanent. If the shading continues for more than 30 seconds, the MPPT executes the analysis of the entire PV output curve. Usually, ten points measured along the P-V curve are enough to find the region of the GMPP. Finally, a direct technique, such as P&O, is launched to find and track GMPP [75].

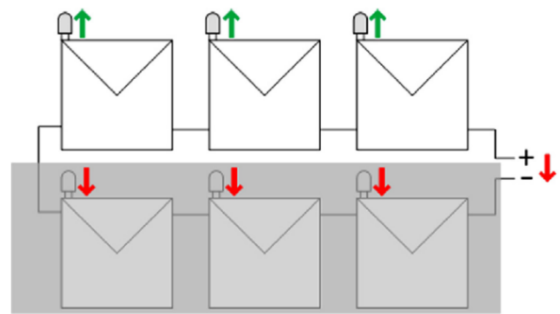


Figure 28. The schematic diagram of the novel MPPT technique [75].

4.8 A Variable Step Size Perturbation & Observation Method

This method is a modified form on conventional P&O and it was proposed to accelerate the convergence to GMPP. In this method, the real MPP is captured and tracked in two modes of operation: the first is the voltage search mode and the second is the MPP search mode. The tracking process used in this method is shown in Figure 29.

During the voltage mode, the operating point of the system is brought near the reference voltage. The reference voltage (V_{ref}) is set at about $0.80 * V_{OC}$ to give an approximate location of the real MPP. In the voltage search mode, to increase the convergence speed, the size of the duty cycle is kept large. The size of the duty cycle is gradually reduced as the operating point of the system gets near the reference voltage. When the operating point becomes close to MPP at $t1$, the MPP search mode becomes activated. The objective of this mode is to bring the operating point as near as possible to the MPP. In this mode, the size of the duty cycle is decreased each time the operating point passes through the MPP. This mode continues until the operating point converges to the MPP at time $t2$. In this phase, there are two states if the captured

MPP is the GMPP and no other GMPP is available to be captured, a constant and small step size P&O algorithm is activated to start the global tracking. On the other hand, if there is another GMPP, which requires capturing and tracking, the technique switches through the voltage search mode and the MPP search mode to track the other MPPs. This process carries on until all the MPPs are captured one by one. Then the system operates near the real GMPP [76].

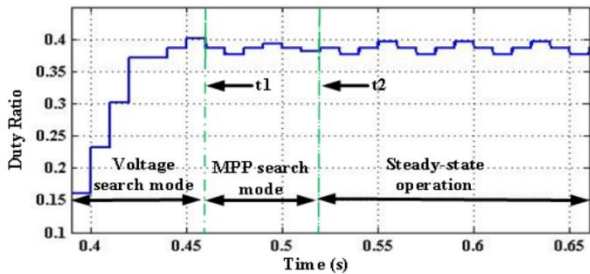


Figure 29. The tracking process in the variable step size P&O technique [76].

4.9 P&O Combined with Particle Swarm Optimization

This technique has two operating stages. In the first stage, in order to conduct a swift search for the first local maximum power point (LMPP), the P&O technique is used. To investigate whether the operating point is going up or down in the P-V characteristic, the operating voltage is perturbed each cycle by a small amount of voltage.

The processing time in the first stage depends on the convergence criterion which must be chosen accurately to determine the first LMPP. If the convergence criterion is large, the algorithm may turn into the second stage before capturing the first LMPP. In contrast, if it is small, a long time may be needed to accomplish the first stage. After reaching the first LMPP, the second stage begins. During this stage, the particle swarm optimization searches for the GMPP. The initial condition of the first particle is chosen according to the value of the convergence voltage in the first stage. For the other particles, the initial conditions range from the convergence voltage to the last point in the search area [77]. The schematic diagram of the proposed system is shown in Figure 30.

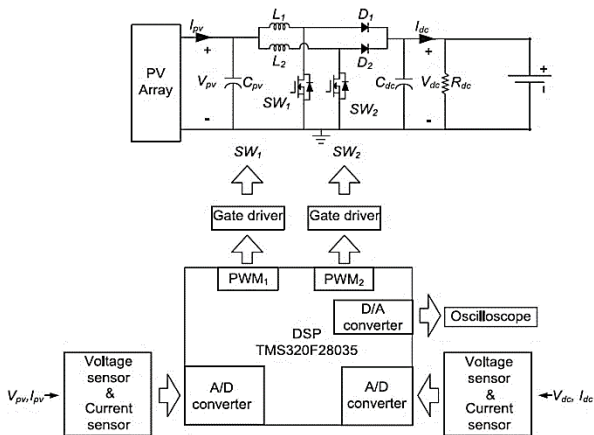


Figure 30. The schematic diagram of the P&O combined with PSO [77].

The most important advantage of this combination that is allows the GMPP to be obtained quickly since the search space is reduced by using the P&O beforehand. In order to improve the efficiency, raise the reliability, and reduce the ripple current; the DC-DC boost converter with an interleaved topology is used.

4.10 A novel technique based on an image of PV modules

The proposed technique relies on estimating the incident irradiance received by the solar panel to calculate the Global Maximum Power Point (GMPP) analytically. This process involves the continuous capture of images of the solar panel using an optical camera, as illustrated in Figure 31. Subsequently, the captured images are input into a mathematical model, as depicted in Figure 32, to determine the incident irradiance. To compute the incident irradiance, the mathematical model takes into account the camera response function and the reflectance characteristics of the solar cells. Once the incident irradiance has been estimated, it becomes possible to calculate the GMPP and its corresponding voltage, relying on the Lambert PV circuits model. To enhance the precision of GMPP calculation and mitigate any inaccuracies stemming from the estimation of incident irradiance, the Perturb and Observe (P&O) technique is employed. This corrective step ensures that external factors such as moisture and dirt, which can adversely impact incident irradiance estimation, do not compromise the accuracy of GMPP determination [78].

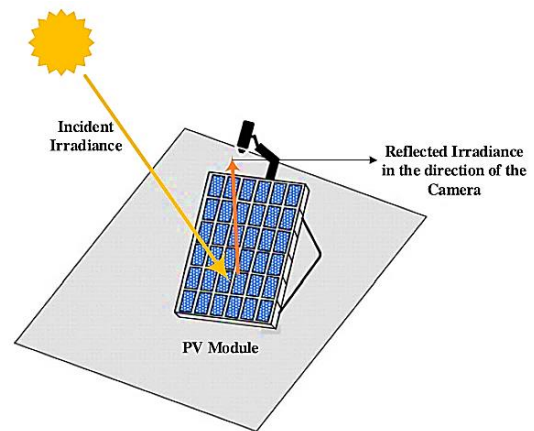


Figure 31. The proposed technique to capture the image of the solar panel [78].

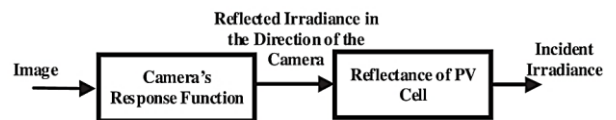


Figure 32. The flowchart for estimating the incident irradiance [78].

4.11 Simulated Annealing Optimization

This optimization is inspired by the metal annealing process. In this optimization, some parameters such as the nominal cooling rate, final temperature rate and initial temperature rate are used to capture the GMPP of the PV system. For every temperature, the optimization measures the corresponding energy to many perturbations it does at

the operating voltage. After that, the measured energy is compared with reference energy. If the measured energy at the new operating point is greater than the reference energy, it is considered as the new operating point. On the other hand, if the measured energy is less than reference energy, it may still be considered based on the acceptance possibility P_r as follows:

$$P_r = \exp \left[\frac{P_k - P_i}{T_k} \right] \quad (45)$$

Here, P_i refers to the power at the previous operating point, P_k refers to the power at the new operating point, and T_k refers to the current system temperature. This optimization consists of two cooling processes, one is adaptive and the other is static kind. The geometric cooling process is expressed as follows:

$$T_k = \alpha T_{k-1} - 1 \quad (46)$$

where, T_k refers to the temperature at the current step, T_{k-1} refers to the temperature at the previous step and α is a constant ($\alpha < 1$) [79].

4.12 Fuzzy Logic Controller Based on a Single Input

Since the structure of conventional fuzzy logic-based MPPT uses mainly two inputs and has at least 25 rules, it needs a long time for computation and is difficult to be implemented. For these reasons a fuzzy logic controller based on a single input, three rules and three linguistic variables is proposed. In this method, the structure of MPPT is facilitated. According to the P&O technique, the error was taken as $E = (\Delta P / \Delta V)$, for each step, it was concluded that:

If $E < 0$, then $D = D + \Delta D$.

If $E > 0$, then $D = D - \Delta D$.

If $E = 0$, then $D = D$.

In this method, the input signal to the controller is the error E and the output signal of the controller is the change of the duty cycle ΔD . The membership function of the proposed method is shown in Figure 33, where it has three linguistic variables: negative N , positive P and zero ZO . The values of ϕ , r and K are set based on the user experience. The author set them to 4.96, 0.33 and 1, respectively. According to the given membership function, the rules and the linguistic expressions are as follows:

Rule 1: If E is positive mid or positive big, that means the operating point is on the left of the MPP (near or far), then the duty cycle will be negative mid or negative big.

Rule 2: If E is negative mid or negative big, the operating point is on the right of the MPP (near or far), then the duty cycle will be positive mid or positive big.

Rule 3: If E is zero, means the MPP is reached and the change in the duty cycle will be zero.

Once the GMPP is reached, the step of the duty cycle is reduced in order to decrease the steady-state oscillation [80].

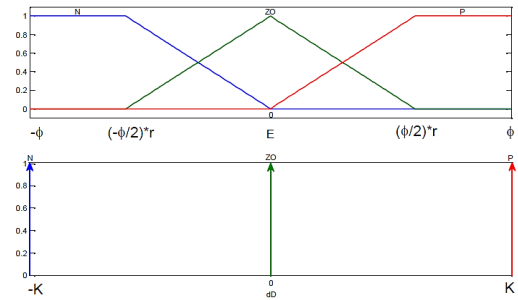


Figure 33. The membership functions of the proposed FLC [80].

4.13 Artificial Neural Network Based MPPT

The proposed technique has two procedures; one becomes active under uniform irradiance conditions, and the other under partial shading conditions. The values of the current and voltage of the PV modules are measured in each sampling time and the difference between the current value of the power and the previous value is calculated. After that, the change in produced power is compared with a preselected threshold value. If the change in the power is less than the certain threshold value, it is considered that the characteristics keep the same shape and the tracking is performed by using one of the conventional MPPT techniques such as P&O or IC. On the other hand, if the threshold value is overflown, which means there is a real change in P-V characteristics, then the ANN-based method is activated to determine the location of GMPP and is followed by one of the conventional methods to perform the tracking. A flowchart of the ANN technique is shown in Figure 34.

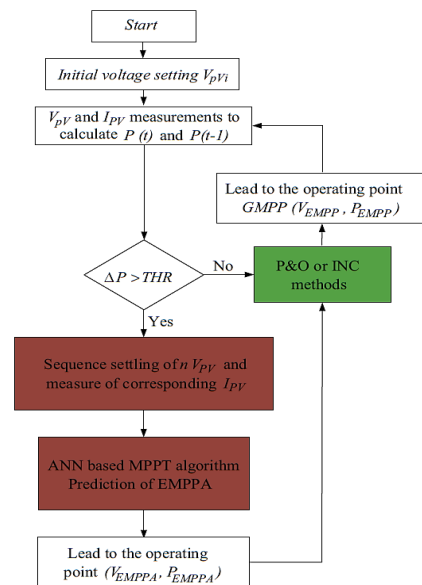


Figure 34. The flowchart of the ANN technique [81].

After activating the ANN method, the power converter, connected between the PV modules and the load, forces the PV modules to sequentially operate at different values of voltage, and then the corresponding current values are measured. The values of current and voltage (I_{PV} , V_{PV}) represent the inputs of the ANN technique. According to the inputs, the ANN provides the value of the voltage corresponding to the GMPP, and then

by the power converter, the operating point is imposed on the PV modules. To improve accuracy, one of the conventional methods is used to make the operating point exactly at the GMPP. In this method, the time needed to predict the GMPP is short and the accuracy is good [81].

4.14 Dormant Particle Swarm Optimization

Since conventional particle swarm optimization (CPSO) uses a random number of particles, it suffers from some drawbacks. First, more iterations are needed by CPSO if the random number of the particles is small; second, if the power values of LMPP and GMPP are close to each other, CPSO may not capture the real GMPP. To overcome these drawbacks, dormant particle swarm optimization (DPSO) is proposed in which the random number of particles is eliminated, and the velocity factor is finite to a certain value. To explain how it functions, let us suppose there are three particles, which are utilized when the PV panels are subjected to partial shading conditions as shown in Figure 35. In CPSO, each particle will search its neighborhood frequently, which means its effect will be limited in a small region leading to an increase in the search time and decrease in efficiency. Nevertheless, in DPSO the process will be as follows:

- 1) First case: the first particle P1 is near the neighborhood of the second particle P2. In the CPSO, P1 will search frequently the neighbourhood of P2, whereas, in DPSO, this particle will be turned into a dormant state and not participate in the next iteration. Furthermore, the neighborhood of P1 will be dominated by P2.
- 2) Second case: as shown in Figure 35, since the distance between P2 and P3 is big, P3 will continue sweeping the region between LP3 and LP2.
- 3) Third case: as has been shown, P2 can catch the GMPP at first since its initial position is near the GMPP. P2 will keep sweeping the region around GMPP during the next iterations.

So in DPSO, the particles have an active state and dormant state. In addition, like the volcano, the dormant particle has an alive state and a dead state. The particle in the first case is in dead dormancy since it will not participate in the next iteration. In contrast, the particles in the second and third cases are in the alive dormancy and they will participate in the next iterations. The DPSO algorithm is combined with the IC algorithm in a dual-algorithm model. After determining the location of GMPP, the IC algorithm is employed to track it accurately [82].

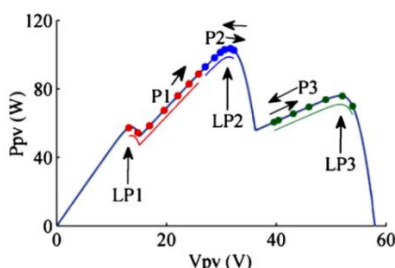


Figure 35. Distribution of particles in PSO [82].

4.15 Genetic Algorithm (GA)

The genetic algorithm (GA) was inspired by natural selection [83]. It is an algorithm based on the concept of survival of the fittest population. Through the iterative use of genetic operators on the existing individuals, the new populations are produced. The main elements of GA are chromosome, selection, crossover, mutation, and fitness functions. The fundamental procedure for GA can be summarized as follows [84]:

- 1) Defining the input variables which are the population size and the maximum number of iterations.
- 2) A number of candidate solutions called chromosomes are first evaluated by the fitness function.
- 3) Choosing a pair of chromosomes from the initial population based on fitness value.
- 4) Applying the crossover operations on the selected pair with crossover probability.
- 5) Applying mutation on the offspring with mutation probability.
- 6) Replacing the old population with the newly generated population.
- 7) Finding the best global solution.

The working steps of the GA are shown in Figure 36. GA has been used to achieve MPP in many studies. A real-time GA was presented in Ref. [85]. The validity of the proposed method was tested for the identical parameters. It has been found through simulation and experiments that stability can be improved by maximizing a fitness function. The proposed method was effective in finding the GMPP under partial shading conditions and reducing the oscillation around the MPP. However, the GA is complex and requires a long computational time to capture the GMPP.

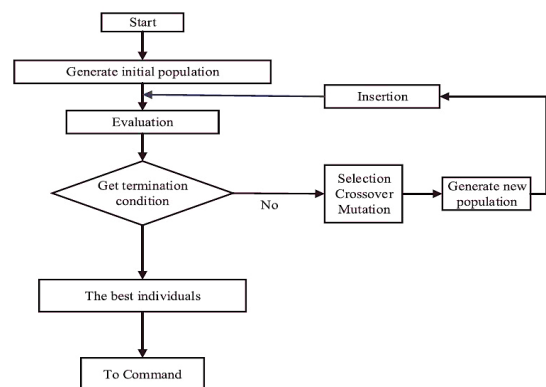


Figure 36. The flowchart of the GA [86].

4.16 Bat Algorithm (BA)

The Bat Algorithm (BA) is a population-based optimization technique bio-inspired on the echolocation features of the microbats in locating their prey [87]. Yang [88] developed the BA by optimizing some of the echolocation characteristics of microbats. This algorithm adopts the features of single microbes in searching and catching prey even in complete darkness [89, 90]. When implementing the main theory of the BA, the following ideas are considered [91]:

- 1) All bats use their echolocation to feel the distance to their prey. Moreover, they can detect the difference between available foods and physical obstacles.
- 2) When searching for prey, each bat flies randomly with a constant frequency, loudness, and changing wavelength. Depending on the proximity of the prey, they automatically adjust their wavelength or frequency of the pulse emission rate.
- 3) With the decreased distance of the prey, the loudness of the bat's changes from a high value to a low fixed value.

In many studies, this algorithm has been employed to address the problems associated with local and global maximum points. Initially, each microbe is given a random frequency value that is distributed between a predefined minimum and maximum value, and once the first-best solution for each microbat is reached in the local search, it proceeds to the second step to find the best new solution. The algorithm conducts a comparison involving all solutions provided by microbats to reach the best global solution [91]. The BA has been used in many studies to deal with PSCs for MPPT applications [92]. Experimental and simulation studies were conducted, and the results showed the efficiency of the algorithm in finding GMPP. The BA was employed to achieve MPP for a Switched Reluctance Motor (SRM) [93]. The optimization was achieved by monitoring the power generated by the solar array and adjusting the duty cycle of the DC-DC converter to obtain the optimum parameters of the control system. The simulation results validated the effectiveness of the proposed method in providing the maximum power of SRM under atmospheric conditions.

4.17 Firefly Algorithm (FA)

This algorithm is based on the firefly phenomenon. The flash produced by the fireflies has many fundamental functions such as mating, hunting and protecting; however, in order to simplify the firefly algorithm (FA), the following assumptions can be made:

- 1) All fireflies are attracted to each other depending only on brightness and regardless of sex, where the less bright firefly moves to the brighter and more attractive firefly. They will keep moving randomly until they find a brighter one.
- 2) The objective function affects and determines the level of brightness. Herein, the level of brightness is in direct proportion to the value of the objective function.

In this algorithm, the brightness of the firefly expresses the energy produced from the PV array while the position of the firefly is the duty cycle.

Assuming X_P and X_R are the coordinates for the P & R fireflies, respectively, the distance between them is given as:

$$X_{PR} = \|X_P - X_R\| \tag{47}$$

If the brightness of P is less than the brightness of R, then the firefly P will move towards the firefly R and the new coordinate of P becomes:

$$X_{P_{new}} = X_P + \beta \cdot (X_P - X_R) + \alpha \cdot (rand - \frac{1}{2}) \tag{48}$$

where β is a function of the distance between two fireflies, rand is a random number uniformly distributed between [0, 1] for each movement of firefly, α is a constant ranging between [0, 1] [94].

The performance of this proposed algorithm is good compared with PSO and P&O algorithms. However, the gradual change in the positions of the fireflies leads to an increase in the convergence time to the GMPP, especially if the number of brighter fireflies is high. This can be explained from Fig. 37. (a), If there are four fireflies and their brightness gradually increases from 1 to 4, then the least bright firefly 1 will first move to firefly 2, then to firefly 3 and later to firefly 4 respectively and the brightness of firefly 1 will change as its position changes. These movements cause an increase in the convergence time to the GMPP. To overcome such a drawback, a modified firefly algorithm (MFA) was proposed [95]. The author suggested that instead of moving the less bright firefly sequentially towards the brighter fireflies, it should move towards the average of the coordinates of all the brighter fireflies as a representative point, as shown in Figure 37. (b). In this case, the final coordinate of the firefly 1 is the average coordinate of the fireflies 2, 3 and 4. It can be formulated as:

$$X_P = X_P + \beta \cdot (X_{j_{avg}} - X_P) + \alpha \cdot (rand - \frac{1}{2}) \tag{49}$$

Here $X_{j_{avg}}$ represents the average coordinates of the brighter fireflies, and is given as:

$$X_{j_{avg}} = \frac{1}{L} \sum_{m=1}^L X_j \tag{50}$$

Here L is the number of the brighter firefly.

Thus, the number of computational operations is reduced resulting in decreasing the time required to converge to GMPP. Although the experimental results showed that MFL has a better performance than FL, the search space will scale up if the GMPP is too far from the initial point.

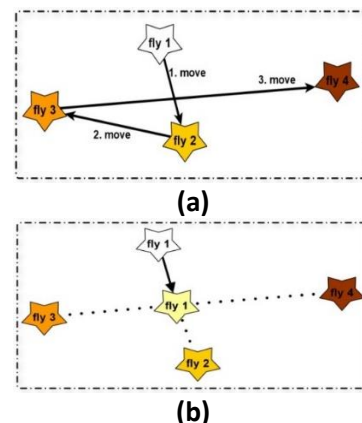


Figure 37. The movement of firefly in: (a) conventional FA; (b) modified FA [96].

4.18 A Hybrid Approach Based on Firefly and P&O Algorithms

With the intention of dealing with the issue of PSCs and improving the convergence speed to GMPP, a hybrid algorithm based on the modified firefly algorithm and the P&O algorithm was proposed [96]. The proposed MPPT technique achieved global tracking by employing three loops. The first loop is called the identifying loop where the location of GMPP is determined. In this loop, seven fireflies are used, and their initial location is manually given. The second loop is called the approximating loop where the operating point of the system is brought near the GMPP. In this loop, the fireflies that produced less power move near the firefly that produced maximum power during the first approximation as shown in Figure 38. Then in the second approximation the fireflies that produced less power in the first approximation, move toward the firefly that produced the maximum power, as shown in Figure 39. At the end of the second loop, one point called a reference point is obtained. From the reference point, the third loop starts tracking the GMPP. In the first and second loops, the Firefly algorithm was used, while the P&O algorithm was used in the third loop. The flowchart of the proposed hybrid algorithm is shown in Figure 40. It is noteworthy that the search range of this algorithm has been reduced which reduced the time required for convergence with the GMPP. Furthermore, the convergence process with GMPP was simplified by manually defining the initial locations of the fireflies. The simulation and experimental results showed the effectiveness and robustness of this algorithm in capturing and tracking the GMPP under different PSCs patterns.

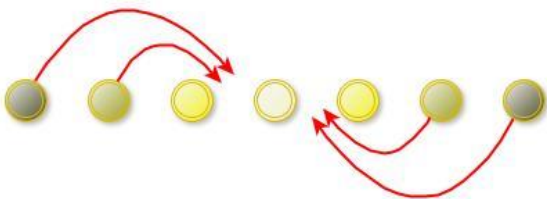


Figure 38. The movement of the fireflies after identifying loop [96].

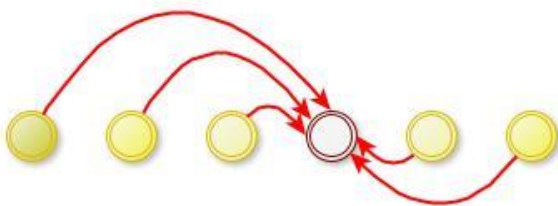


Figure 39. The movement of the fireflies after first approximation [96].

5 Discussion

Research into MPPT techniques to enhance performance is an ongoing endeavor. When evaluating MPPT algorithms and making appropriate selections for a successful design, several criteria must be considered:

1) **Hardware Implementation:** The ease of implementing the proposed algorithm is a crucial factor in selecting the appropriate MPPT technology. Some techniques are

straightforward to implement, requiring minimal maintenance and calibration. In contrast, others are more challenging to implement and may necessitate ongoing adjustments to account for changes in surrounding conditions.

2) **Dynamic Response:** Given the rapid changes in climatic conditions that can shift the location of the Maximum Power Point (MPP) on the P-V curve, MPPT algorithms must exhibit a swift response to identify and track the new MPP. This responsiveness is crucial to avoid energy losses.

3) **Sensors Requirement:** Knowledge of input parameters (such as insolation and temperature) and output parameters (voltage and current) of the solar module is essential for MPPT algorithms. Consequently, many MPPT systems employ multiple sensors. However, modified MPPT algorithms often aim to reduce complexity and cost by using fewer sensors.

4) **Tracking Efficiency:** Tracking efficiency is a pivotal characteristic that defines the quality of MPPT algorithms. It is associated with the speed and accuracy of tracking the optimal maximum power point. Tracking efficiency is quantified as the ratio between the actual power extracted from the solar module and the theoretical power under the same atmospheric conditions and during the same period. A well-designed MPPT system should offer high tracking efficiency to improve overall P-V system performance under variable atmospheric conditions.

5) **Cost:** Several factors influence the cost of MPPT systems, including complexity, system features, the number of required sensors, and the difficulty of programming and implementation. Generally, digital systems based on microprocessors tend to be more expensive than analog systems.

In Table 5, a comparison of several conventional and modern MPPT techniques is presented. Notably, the cost was omitted from the comparison due to the challenge of estimating the cost of each technique accurately. However, it's important to note that as the complexity of a technique increases, there is typically a greater reliance on sophisticated systems, which inevitably leads to increased costs.

The ability of the techniques to reliably deal with PSCs was indicated by "no" if it is unreliable and "yes" if it is reliable to converge to the GMPP. The convergence speed is categorized as "fast", "low" and "varies". Here, "varies" means that the convergence to MPP depends on the selection of parameters, for example, the step size of the P&O approach.

The oscillation around MPP is categorized as "no", "yes", "sometimes" and "common". "Sometimes" expresses that the technique may exhibit oscillation around the MPP depending on the implementation and parameter selection, while "common" expresses that the technique often makes oscillation.

The efficiency is indicated as "high", "low", and "varies". It expresses the ability of the technique to reliably track the MPP.

Implementation complexity is categorized as "high", "moderate" and "low". The complexity depends on the need to use sophisticated systems, as well as on the

characteristics of the technique in terms of the implementation difficulty.

Dependence on the characteristics of the PV panels used is shown by "no" or "yes". The case "yes" indicates that initialization is required with the PV panels parameters.

The table shows that there is no single technique that can deal with PSCs while meeting all the required criteria such as simplicity, tracking efficiency, convergence speed, durability, low cost, and others. In general, the weight in choosing the appropriate technique depends on the type of application and the goal to be achieved.

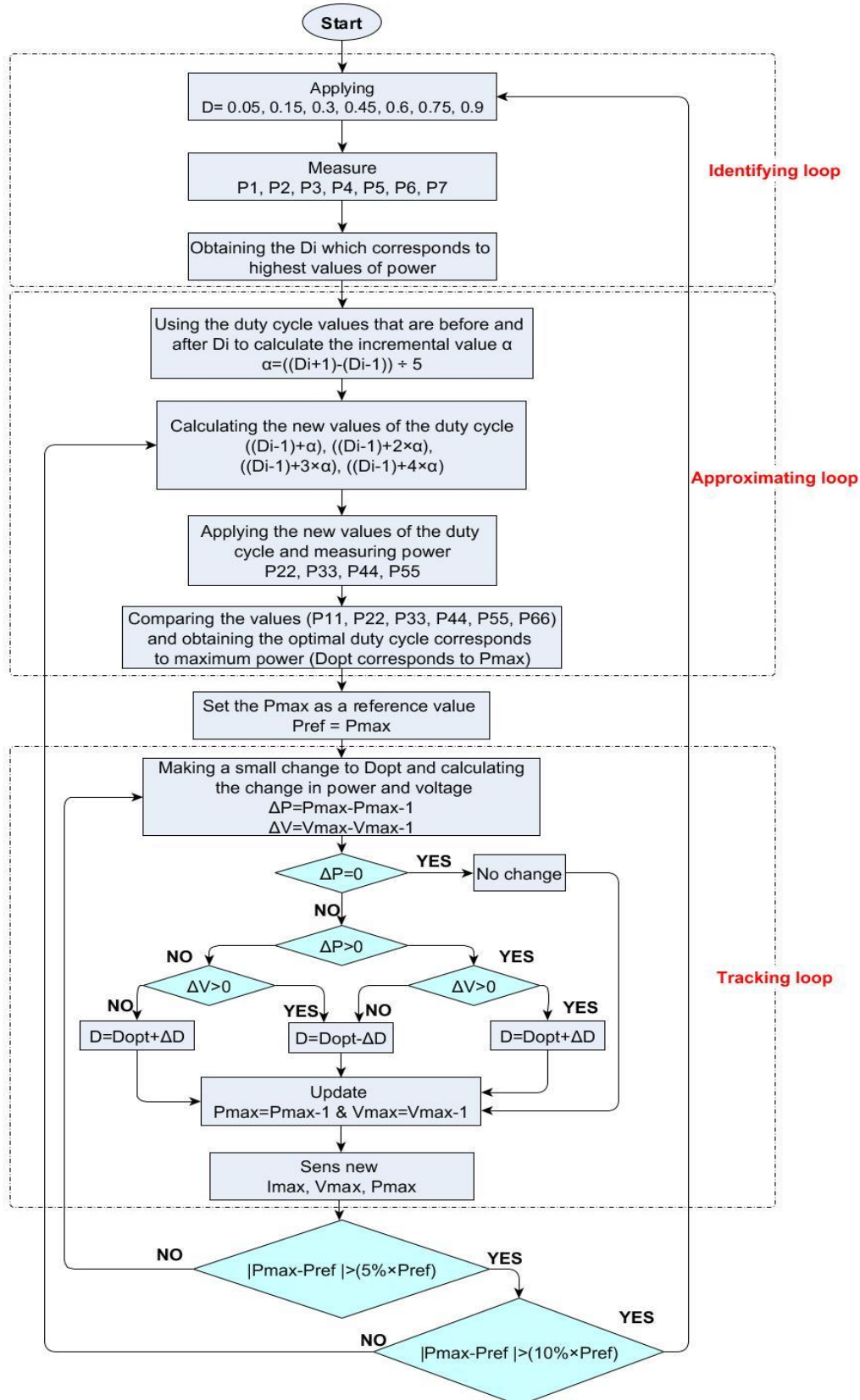


Figure 40. The flowchart of the hybrid approach based on Firefly and P&O algorithms [96].

Table 5. Comprehensive comparison of various conventional and global MPPT techniques

Conventional MPPT techniques							
Technique	Ability to find GMPP	Implementation Complexity	Convergence speed	Efficiency	Sensor requirement	Oscillation around MPP	Dependence on PV panel parameters
Constant voltage (CV)	No	Low	Varies	Low	Voltage	Common	Yes
Open-circuit voltage	No	Low	Fast	Low	Voltage	No	Yes
Short-circuit current	No	Low	Fast	Low	Current	No	Yes
Feedback voltage or current	No	Low	Fast	Low	Voltage or Current	Yes	No
P-N junction drop voltage tracking	No	Low	Varies	Low	Voltage	Yes	Yes
Look-up table	No	Moderate	Varies	Low	Irradiance - Temperature	Common	Yes
Load current or load voltage maximization	No	Low	Varies	Low	Voltage or Current	Yes	No
Only current photovoltaic	No	Low	Varies	Varies	Current	Yes	No
PV output senseless (POS) control	No	Low	Varies	Varies	Current	Yes	No
Perturbation & Observation (P&O)	No	Low	Varies	Varies	Voltage- Current	Common	No
Three-point weight comparison	No	Low	Varies	Varies	Voltage- Current	Sometimes	No
On-line MPP search	No	Moderate	Varies	Varies	Voltage- Current	Common	Yes
DC-link capacitor droop control	No	Low	Low	Varies	Voltage- Current	Common	No
Current sweep	No	Moderate	Low	Low	Voltage- Current	Common	Yes
Incremental conductance (IC)	No	Low	Varies	Varies	Voltage- Current	Common	No
I_{MPP} and V_{MPP} computation	No	Moderate	Varies	Varies	Voltage- Current- Irradiance- Temperature	Common	Yes
Ripple correlation control (RCC)	No	Low	Fast	Varies	Voltage- Current	No	No
Fuzzy logic (FL)	No	High	Fast	Varies	Voltage- Current	No	Yes
Neural network	No	High	Fast	Varies	Irradiance -Voltage- Current	No	Yes
Global MPPT techniques							
Technique	Ability to find GMPP	Implementation Complexity	Convergence speed	Efficiency	Sensor requirement	Oscillation around MPP	Dependence on PV panel characteristics
Grey wolf	Yes	High	Fast	High	Voltage- Current	No	No
Ant colony	Yes	High	Fast	High	Voltage- Current	No	No
Bee colony	Yes	High	Varies	High	Voltage- Current	No	No
Particle swarm (PSO)	Yes	Moderate	Fast	High	Voltage- Current	No	No
Deterministic particle swarm (DPSO)	Yes	High	Fast	High	Voltage- Current	No	No
A variable step size P&O	Yes	Moderate	Fast	Varies	Voltage- Current	Sometimes	Yes
Hybrid P&O and PSO	Yes	High	Fast	High	Voltage- Current	No	No
Simulated annealing (SA)	Yes	High	Fast	High	Voltage- Current- Temperature	Sometimes	No
FL controller based on a single input	Yes	High	Varies	High	Voltage- Current	No	Yes
Artificial neural network (ANN)	Yes	High	Fast	Varies	Voltage- Current	No	Yes
Genetic algorithm (GA)	Yes	High	Varies	Varies	Voltage- Current	No	No
Bat algorithm (BA)	Yes	High	Fast	High	Voltage- Current	No	No
Firefly algorithm (FA)	Yes	Moderate	Fast	High	Voltage- Current	No	No
Hybrid FA and P&O	Yes	Low	Fast	High	Voltage- Current	No	No

Conclusion

This paper has comprehensively reviewed various MPPT algorithms for PV systems, encompassing both conventional and modern techniques. Over the past few decades, many MPPT algorithms have been developed and documented. They exhibit variations in critical aspects such as convergence speed, complexity, cost,

required implementation hardware, necessary sensors, and their overall effectiveness.

However, in the pursuit of optimizing PV system performance, it is crucial to adopt a pragmatic approach. If a simpler and more cost-effective algorithm can yield similar or even superior results compared to a more expensive or sophisticated counterpart, it stands to reason that the former should be preferred. This is precisely why

some of the proposed algorithms may not find widespread adoption in real PV system implementations.

Under the challenging conditions of partial shading, conventional MPPT techniques often struggle to accurately track the global maximum power point (GMPP), resulting in significant power losses. In response to this challenge, numerous modern MPPT optimizations have been proposed in the literature. These optimizations demonstrate the ability to capture and track the GMPP effectively. However, it's important to note that many of these modern techniques are constrained by varying degrees of complexity and power dissipation. Furthermore, they rely on intricate computational processes, utilizing artificial intelligence algorithms or soft computing algorithms.

In light of these observations, we hope that the near future will witness the development of high-performance, low-complexity, and cost-effective MPPT techniques. By fully harnessing the output power from PV systems at minimal costs, we can take significant strides towards reducing our dependence on conventional fossil fuel resources.

In conclusion, this study not only provides a comprehensive overview of MPPT techniques for PV systems but also underscores the need for continued research in this field. The pursuit of innovative, efficient, and cost-effective solutions is essential to further the adoption of solar energy and ultimately mitigate our reliance on non-renewable energy sources. This, we believe, will be a vital direction for future research in this domain.

Declaration

Ethics committee approval is not required.

References

- [1] Burrett, R., Clini, C., Dixon, R., Eckhart, M., El-Ashry, M., Gupta, D., ... & Ballesteros, A. R. (2009). Renewable energy policy network for the 21st century. *REN21 Renewables Global Status Report*.
- [2] Gielen, D., Boshell, F., Saygin, D., Bazilian, M. D., Wagner, N., & Gorini, R. (2019). The role of renewable energy in the global energy transformation. *Energy strategy reviews*, 24, 38-50.
- [3] Jalil, M. F., Khatoon, S., Nasiruddin, I., & Bansal, R. C. (2022). Review of PV array modelling, configuration and MPPT techniques. *International Journal of Modelling and Simulation*, 42(4), 533-550.
- [4] Worku, M. Y., Hassan, M. A., Maraaba, L. S., Shafiullah, M., Elkadeem, M. R., Hossain, M. I., & Abido, M. A. (2023). A Comprehensive Review of Recent Maximum Power Point Tracking Techniques for Photovoltaic Systems under Partial Shading. *Sustainability*, 15(14), 11132.
- [5] Dayaramani, R., Bharadwaj, S. K., & Gawre, S. K. (2017). Simulation and designing of MPPT based solar PV system with DC-DC boost converter. *Simulation*.
- [6] Mao, M., Cui, L., Zhang, Q., Guo, K., Zhou, L., & Huang, H. (2020). Classification and summarization of solar photovoltaic MPPT techniques: A review based on traditional and intelligent control strategies. *Energy Reports*, 6, 1312-1327.
- [7] Singh, D., & Singh, H. (2019, October). Technical Survey and review on MPPT techniques to attain Maximum Power of Photovoltaic system. In *2019 5th International Conference on Signal Processing, Computing and Control (ISPCC)* (pp. 265-268). IEEE.
- [8] Lasheen, M., Rahman, A. K. A., Abdel-Salam, M., & Ookawara, S. (2016). Performance enhancement of constant voltage based MPPT for photovoltaic applications using genetic algorithm. *Energy Procedia*, 100, 217-222.
- [9] Yu, G. J., Jung, Y. S., Choi, J. Y., & Kim, G. S. (2004). A novel two-mode MPPT control algorithm based on comparative study of existing algorithms. *Solar Energy*, 76(4), 455-463.
- [10] Karami, N., Moubayed, N., & Outbib, R. (2017). General review and classification of different MPPT Techniques. *Renewable and Sustainable Energy Reviews*, 68, 1-18.
- [11] Ngan, M. S., & Tan, C. W. (2011, April). A study of maximum power point tracking algorithms for stand-alone photovoltaic systems. In *2011 IEEE applied power electronics colloquium (IAPEC)* (pp. 22-27). IEEE.
- [12] Shebani, M. M., Iqbal, T., & Quaicoe, J. E. (2016, October). Comparing bisection numerical algorithm with fractional short circuit current and open circuit voltage methods for MPPT photovoltaic systems. In *2016 IEEE Electrical Power and Energy Conference (EPEC)* (pp. 1-5).
- [13] Vălcan, D. M., Marinescu, C., & Kaplanis, S. (2008, May). Connecting a PV supplied micro-grid to the public grid. In *2008 11th International Conference on Optimization of Electrical and Electronic Equipment* (pp. 369-374).
- [14] Ngan, M. S., & Tan, C. W. (2011, April). A study of maximum power point tracking algorithms for stand-alone photovoltaic systems. In *2011 IEEE applied power electronics colloquium (IAPEC)* (pp. 22-27).
- [15] Oh, T., Hassan, O., Shamsir, S., & Islam, S. K. (2019, June). DC-DC boost converter design with maximum power point tracker (MPPT) used in RF-energy harvester. In *2019 IEEE International Symposium on Medical Measurements and Applications (MeMeA)* (pp. 1-5).
- [16] Baimel, D., Shkoury, R., Elbaz, L., Tapuchi, S., & Baimel, N. (2016, June). Novel optimized method for maximum power point tracking in PV systems using Fractional Open Circuit Voltage technique. In *2016 International Symposium on Power Electronics, Electrical Drives, Automation and Motion (SPEEDAM)* (pp. 889-894). IEEE.
- [17] Hui, J. C., Bakhshai, A., & Jain, P. K. (2015). A sensorless adaptive maximum power point extraction method with voltage feedback control for small wind turbines in off-grid applications. *IEEE Journal of Emerging and Selected Topics in Power Electronics*, 3(3), 817-828.
- [18] Kobayashi, K., Matsuo, H., & Sekine, Y. (2006). An excellent operating point tracker of the solar-cell power supply system. *IEEE Transactions on Industrial Electronics*, 53(2), 495-499.
- [19] Kim, Y., Jo, H., & Kim, D. (1996, August). A new peak power tracker for cost-effective photovoltaic power system. In *IECEC 96. Proceedings of the 31st Intersociety Energy Conversion Engineering Conference* (Vol. 3, pp. 1673-1678). IEEE.
- [20] Kota, V. R., & Bhukya, M. N. (2016, February). A simple and efficient MPPT scheme for PV module using 2-dimensional lookup table. In *2016 IEEE Power and Energy Conference at Illinois (PECI)* (pp. 1-7). IEEE.
- [21] Esram, T., & Chapman, P. L. (2007). Comparison of photovoltaic array maximum power point tracking techniques. *IEEE Transactions on energy conversion*, 22(2), 439-449.
- [22] Kislovski, A. S., & Redl, R. (1994, June). Maximum-power-tracking using positive feedback. In *Proceedings of 1994 Power Electronics Specialist Conference-PESC'94* (Vol. 2, pp. 1065-1068). IEEE.

- [23] Salas, V., Olias, E., Lazaro, A., & Barrado, A. (2005). New algorithm using only one variable measurement applied to a maximum power point tracker. *Solar energy materials and solar cells*, 87(1-4), 675-684.
- [24] Salas, V. O. E. L. A., Olias, E., Lazaro, A., & Barrado, A. (2005). Evaluation of a new maximum power point tracker (MPPT) applied to the photovoltaic stand-alone systems. *Solar energy materials and solar cells*, 87(1-4), 807-815.
- [25] S.-J. Lee et al., "The experimental analysis of the grid-connected PV system applied by POS MPPT," in *2007 International Conference on Electrical Machines and Systems (ICEMS)*, 2007: IEEE, pp. 1786-1791.
- [26] Kim, S. Y., Park, S., Jang, S. J., Kim, G. H., Seo, H. R., Park, M., & Yu, I. K. (2009, November). An effective POS MPPT control method for PV power generation system. In *2009 International Conference on Electrical Machines and Systems (pp. 1-6)*. IEEE.
- [27] Mohammed, S. S., Devaraj, D., & Ahamed, T. I. (2016). A novel hybrid maximum power point tracking technique using perturb & observe algorithm and learning automata for solar PV system. *Energy*, 112, 1096-1106.
- [28] Omar, F. A., Gökkuş, G., & Kulaksız, a. A. (2019). Şebekeden Bağımsız FV Sistemde Maksimum Güç Noktası Takip Algoritmalarının Değişken Hava Şartları Altında Karşılaştırmalı Analizi. *Konya Journal of Engineering Sciences*, 7(3), 585-594.
- [29] Motahhir, S., El Hammoumi, A., & El Ghzizal, A. (2018). Photovoltaic system with quantitative comparative between an improved MPPT and existing INC and P&O methods under fast varying of solar irradiation. *Energy Reports*, 4, 341-350.
- [30] Roy, C. P., Naick, B. K., & Shankar, G. (2013). Modified three-point weight comparison method for adaptive MPPT of photovoltaic systems. In *Fifth International Conference on Advances in Recent Technologies in Communication and Computing (ARTCom 2013)* (s. 146-156).
- [31] Hsiao, T., & Chen, C. H. (2002). Maximum power tracking for photovoltaic power system. In *Conference Record of the 2002 IEEE Industry Applications Conference. 37th IAS Annual Meeting* (s. 1035-1040). IEEE.
- [32] Altas, I. H., & Sharaf, A. M. (1996). A novel on-line MPP search algorithm for PV arrays. *IEEE Transactions on Energy Conversion*, 11(4), 748-754.
- [33] Altas, I., & Sharaf, A. (1996). A novel on-line MPP search algorithm for PV arrays. *IEEE Transactions on Energy Conversion*, 11(4), 748-754.
- [34] Godoy, R. B., Bizarro, D. B., De Andrade, E. T., de Oliveira Soares, J., Ribeiro, P. E. M. J., Carniato, L. A., ... & Canesin, C. A. (2016). Procedure to match the dynamic response of MPPT and droop-controlled microinverters. *IEEE transactions on industry applications*, 53(3), 2358-2368.
- [35] Matsui, M., Kitano, T., Xu, D.-h., & Yang, Z.-q. (1999). A new maximum photovoltaic power tracking control scheme based on power equilibrium at DC link. In *Conference Record of the 1999 IEEE Industry Applications Conference. Thirty-Forth IAS Annual Meeting* (s. 804-809). IEEE.
- [36] Kitano, T., Matsui, M., & Xu, D.-h. (2001). Power sensorless MPPT control scheme utilizing power balance at DC link-system design to ensure stability and response. In *IECON'01. 27th Annual Conference of the IEEE Industrial Electronics Society* (s. 1309-1314). IEEE.
- [37] Zhang, L., Hurley, W. G., & Wölfle, W. H. (2011). A New Approach to Achieve Maximum Power Point Tracking for PV System With a Variable Inductor. *IEEE Transactions on Power Electronics*, 26(4), 1031-1037.
- [38] Zhang, L., Hurley, W. G., & Wölfle, W. H. (2010). A new approach to achieve maximum power point tracking for PV system with a variable inductor. *IEEE Transactions on Power Electronics*, 26(4), 1031-1037.
- [39] Husain, M. A., et al. (2017). Comparative assessment of maximum power point tracking procedures for photovoltaic systems. *Green Energy & Environment*, 2(1), 5-17.
- [40] Bodur, M., & Ermis, M. (1994). Maximum power point tracking for low power photovoltaic solar panels. In *Proceedings of MELECON'94. Mediterranean Electrotechnical Conference (s. 758-761)*. IEEE.
- [41] AlhajOmar, F., Gokkus, G., & Kulaksiz, A. A. (2019). Rapid Control Prototyping Based on 32-bit ARM Cortex-M3 Microcontroller for Photovoltaic MPPT Algorithms. *International Journal of Renewable Energy Research*, 9.
- [42] Hussein, K., Muta, I., Hoshino, T., & Osakada, M. (1995). Maximum photovoltaic power tracking: an algorithm for rapidly changing atmospheric conditions. *IEE Proceedings-Generation, Transmission Distribution*, 142(1), 59-64.
- [43] Anwer, A. M. O., Omar, F. A., Bakir, H., & Kulaksiz, A. A. (2020). Sensorless Control of a PMSM Drive Using EKF for Wide Speed Range Supplied by MPPT Based Solar PV System. *Elektronika ir Elektrotechnika*, 26(1), 32-39.
- [44] Salas, V., Olias, E., Barrado, A., & Lazaro, A. (2006). Review of the maximum power point tracking algorithms for stand-alone photovoltaic systems. *Solar Energy Materials and Solar Cells*, 90(11), 1555-1578.
- [45] Anwar, M. H., & Roy, P. (2019). A Modified Incremental Conductance Based Photovoltaic MPPT Charge Controller. In *2019 International Conference on Electrical, Computer and Communication Engineering (ECCE)* (pp. 1-5).
- [46] Takashima, T., Tanaka, T., Amano, M., & Ando, Y. (2000). Maximum output control of photovoltaic (PV) array. In *Collection of Technical Papers. 35th Intersociety Energy Conversion Engineering Conference and Exhibit (IECEC)* (Vol. 1, pp. 380-383). IEEE.
- [47] Rafiei, M., Abdolmaleki, M., & Mehrabi, A. H. (2012). A new method of maximum power point tracking (MPPT) of photovoltaic (PV) cells using impedance adaption by Ripple correlation control (RCC). In *2012 Proceedings of 17th Conference on Electrical Power Distribution*, 2-3 May 2012 (pp. 1-8).
- [48] Midya, P., Krein, P. T., Turnbull, R. J., Reppa, R., & Kimball, J. (1996). Dynamic maximum power point tracker for photovoltaic applications. In *PESC Record. 27th Annual IEEE Power Electronics Specialists Conference* (Vol. 2, pp. 1710-1716).
- [49] Bendib, B., Krim, F., Belmili, H., Almi, M. F., & Boulouma, S. (2014). Advanced Fuzzy MPPT Controller for a Stand-alone PV System. *Energy Procedia*, 50, 383-392.
- [50] Anwer, A. M. O., Omar, F. A., & Kulaksiz, A. A. (2020). Design of a Fuzzy Logic-based MPPT Controller for a PV System Em-ploying Sensorless Control of MRAS-based PMSM. *International Journal of Control Automation Systems*.
- [51] Kottas, T. L., Boutalis, Y. S., & Karlis, A. D. (2006). New maximum power point tracker for PV arrays using fuzzy controller in close cooperation with fuzzy cognitive networks. *IEEE Transactions on Energy Conversion*, 21(3), 793-803.
- [52] Liu, Y.-H., Liu, C.-L., Huang, J.-W., & Chen, J.-H. (2013). Neural-network-based maximum power point tracking methods for photovoltaic systems operating under fast changing environments. *Solar Energy*, 89, 42-53.
- [53] Hiyama, T., Kouzuma, S., & Imakubo, T. (1995). Identification of optimal operating point of PV modules using neural network for real time maximum power tracking control. *IEEE Transactions on Energy Conversion*, 10(2), 360-367.

- [54] Mohapatra, A., Nayak, B., Das, P., & Mohanty, K. B. (2017). A review on MPPT techniques of PV system under partial shading condition. *Renewable Sustainable Energy Reviews*, 80, 854-867.
- [55] Gosumbonggot, J., & Fujita, G. (2019). Photovoltaic's Hotspot and Partial Shading Detection Algorithm Using Characteristic Curve's Analysis. In *2019 9th International Conference on Power and Energy Systems (ICPES)* (pp. 1-6).
- [56] Omar, F. A., Pamuk, N., & Kulaksız, A. A. (2023). A critical evaluation of maximum power point tracking techniques for PV systems working under partial shading conditions. *Turkish Journal of Engineering*, 7(1), 73-81.
- [57] Chaudhary, A., Gupta, S., Pande, D., Mahfooz, F., & Varshney, G. (2015). Effect of partial shading on characteristics of PV panel using Simscape. *International Journal of Engineering Research and Applications*, 5(10), 85-89.
- [58] Laxman, B., Annamraju, A., & Srikanth, N. V. (2021). A grey wolf optimized fuzzy logic based MPPT for shaded solar photovoltaic systems in microgrids. *International Journal of Hydrogen Energy*, 46(4), 3182-3193.
- [59] Pamuk, N. (2023). Performance Analysis of Different Optimization Algorithms for MPPT Control Techniques under Complex Partial Shading Conditions in PV Systems. *Energies*, 16(8), 3358.
- [60] Mohanty, S., Subudhi, B., & Ray, P. K. (2015). A new MPPT design using grey wolf optimization technique for photovoltaic system under partial shading conditions. *IEEE Transactions on Sustainable Energy*, 6(1), 181-188.
- [61] Phanden, R. K., Sharma, L., Chhabra, J., & İ. Demir, H. (2020). A novel modified ant colony optimization based maximum power point tracking controller for photovoltaic systems. *Materials Today: Proceedings*.
- [62] Huang, K.-H., Chao, K.-H., & Lee, T.-W. (2023). An Improved Photovoltaic Module Array Global Maximum Power Tracker Combining a Genetic Algorithm and Ant Colony Optimization. *Technologies*, 11(2), 61.
- [63] Jiang, L. L., Maskell, D. L., & Patra, J. C. (2013). A novel ant colony optimization-based maximum power point tracking for photovoltaic systems under partially shaded conditions. *Energy Buildings*, 58, 227-236.
- [64] Jiang, L. L., & Maskell, D. L. (2014). A uniform implementation scheme for evolutionary optimization algorithms and the experimental implementation of an ACO based MPPT for PV systems under partial shading. In *2014 IEEE Symposium on Computational Intelligence Applications in Smart Grid (CIASG)* (pp. 1-8). IEEE.
- [65] Motahhir, S., El Hammoumi, A., & El Ghzizal, A. (2020). The most used MPPT algorithms: Review and the suitable low-cost embedded board for each algorithm. *Journal of cleaner production*, 246, 118983.
- [66] Fanani, M. R., Sudiharto, I., & Ferdiansyah, I. (2020). Implementation of Maximum Power Point Tracking on PV System using Artificial Bee Colony Algorithm. In *2020 3rd International Seminar on Research of Information Technology and Intelligent Systems (ISRITI)* (pp. 117-122).
- [67] Sundareswaran, K., Sankar, P., Nayak, P. S. R., Simon, S. P., & Palani, S. (2014). Enhanced energy output from a PV system under partial shaded conditions through artificial bee colony. *IEEE transactions on sustainable energy*, 6(1), 198-209.
- [68] Benyoucef, A. S., Chouder, A., Kara, K., & Silvestre, S. (2015). Artificial bee colony based algorithm for maximum power point tracking (MPPT) for PV systems operating under partial shaded conditions. *Applied Soft Computing*, 32, 38-48.
- [69] Wasim, M. S., Amjad, M., Habib, S., Abbasi, M. A., Bhatti, A. R., & Muyeen, S. (2022). A critical review and performance comparisons of swarm-based optimization algorithms in maximum power point tracking of photovoltaic systems under partial shading conditions. *Energy Reports*, 8, 4871-4898.
- [70] Wei-Ru, C., Chen, L., Chia-Hsuan, W., & Ci-Min, L. (2015). Multiclustor-based particle swarm optimization algorithm for photovoltaic maximum power point tracking. In *2015 IEEE 2nd International Future Energy Electronics Conference (IFEEEC)* (pp. 1-6).
- [71] Liu, Y.-H., Huang, S.-C., Huang, J.-W., & Liang, W.-C. (2012). A particle swarm optimization-based maximum power point tracking algorithm for PV systems operating under partially shaded conditions. *IEEE Transactions on Energy Conversion*, 27(4), 1027-1035.
- [72] Ishaque, K., Salam, Z., Taheri, H., & Shamsudin, A. (2011). Maximum power point tracking for PV system under partial shading condition via particle swarm optimization. In *2011 IEEE Applied Power Electronics Colloquium (IAPEC)* (pp. 5-9).
- [73] Ishaque, K., Salam, Z., Amjad, M., & Mekhilef, S. (2012). An improved particle swarm optimization (PSO)-based MPPT for PV with reduced steady-state oscillation. *IEEE transactions on Power Electronics*, 27(8), 3627-3638.
- [74] Elserougi, A. A., Diab, M. S., Massoud, A. M., Abdel-Khalik, A. S., & Ahmed, S. (2015). A switched PV approach for extracted maximum power enhancement of PV arrays during partial shading. *IEEE Transactions on Sustainable Energy*, 6(3), 767-772.
- [75] Bayod-Rújula, A.-A., & Cebollero-Abián, J.-A. (2014). A novel MPPT method for PV systems with irradiance measurement. *Solar Energy*, 109, 95-104.
- [76] Ahmad, J., Spertino, F., Di Leo, P., & Ciocia, A. (2016). A variable step size perturb and observe method based MPPT for partially shaded photovoltaic arrays. In *PCIM Europe 2016; International Exhibition and Conference for Power Electronics, Intelligent Motion, Renewable Energy and Energy Management* (pp. 1-8).
- [77] Lian, K., Jhang, J., & Tian, I. (2014). A maximum power point tracking method based on perturb-and-observe combined with particle swarm optimization. *IEEE journal of photovoltaics*, 4(2), 626-633.
- [78] Mahmoud, Y., & El-Saadany, E. F. (2016). A novel MPPT technique based on an image of PV modules. *IEEE Transactions on Energy Conversion*, 32(1), 213-221.
- [79] Lyden, S., & Haque, M. E. (2015). A simulated annealing global maximum power point tracking approach for PV modules under partial shading conditions. *IEEE Transactions on Power Electronics*, 31(6), 4171-4181.
- [80] Benlahbib, B., Bouarroudj, N., Mekhilef, S., Abdelkrim, T., Lakhdari, A., & Bouchafaa, F. J. E. i. E. (2018). A Fuzzy Logic Controller Based on Maximum Power Point Tracking Algorithm for Partially Shaded PV Array-Experimental Validation. *Elektronika ir Elektrotechnika*, 24(4), 38-44.
- [81] Rizzo, S. A., & Scelba, G. (2015). ANN based MPPT method for rapidly variable shading conditions. *Applied Energy*, 145, 124-132.
- [82] Shi, J., Zhang, W., Zhang, Y., Xue, F., & Yang, T. (2015). MPPT for PV systems based on a dormant PSO algorithm. *Electric Power Systems Research*, 123, 100-107.
- [83] Chao, K.-H., & Rizal, M. N. (2021). A Hybrid MPPT Controller Based on the Genetic Algorithm and Ant Colony Optimization for Photovoltaic Systems under Partially Shaded Conditions. *Energies*, 14(10), 2902.
- [84] Katoch, S., Chauhan, S. S., & Kumar, V. (2021). A review on genetic algorithm: past, present, and future. *Multimedia tools and applications*, 80, 8091-8126.

- [85] Hadji, S., Gaubert, J.-P., & Krim, F. (2018). Real-Time Genetic Algorithms-Based MPPT: Study and Comparison (Theoretical and Experimental) with Conventional Methods. *Energies*, 11(2), 459.
- [86] Baba, A. O., Liu, G., & Chen, X. (2020). Classification and evaluation review of maximum power point tracking methods. *Sustainable Futures*, 2, 100020.
- [87] Asim, M., Agrawal, P., Tariq, M., & Alamri, B. (2021). MPPT-based on Bat algorithm for photovoltaic systems working under partial shading conditions. *Journal of Intelligent & Fuzzy Systems*, Preprint, 1-9.
- [88] Yang, X.-S. (2010). A new metaheuristic bat-inspired algorithm. In *Nature inspired cooperative strategies for optimization (NICSO 2010)*. Springer, pp. 65-74.
- [89] Kaced, K., Larbes, C., Ramzan, N., Bounabi, M., & Dahmane, Z. e. (2017). Bat algorithm based maximum power point tracking for photovoltaic system under partial shading conditions. *Solar Energy*, 158, 490-503.
- [90] Wu, Z., & Yu, D. (2018). Application of improved bat algorithm for solar PV maximum power point tracking under partially shaded condition. *Applied Soft Computing*, 62, 101-109.
- [91] Da Rocha, M. V., Sampaio, L. P., & da Silva, S. A. O. (2020). Comparative analysis of MPPT algorithms based on Bat algorithm for PV systems under partial shading condition. *Sustainable Energy Technologies and Assessments*, 40, 100761.
- [92] Eltamaly, A. M. (2021). Optimal control parameters for bat algorithm in maximum power point tracker of photovoltaic energy systems. *International Transactions on Electrical Energy Systems*, 31(4), e12839.
- [93] Oshaba, A. S., Ali, E. S., & Abd Elazim, S. M. (2015). MPPT control design of PV system supplied SRM using BAT search algorithm. *Sustainable Energy, Grids and Networks*, 2, 51-60.
- [94] Sundareswaran, K., Peddapati, S., & Palani, S. (2014). MPPT of PV systems under partial shaded conditions through a colony of flashing fireflies. *IEEE Transactions on Energy Conversion*, 29(2), 463-472.
- [95] Teshome, D., Lee, C., Lin, Y., & Lian, K. (2016). A modified firefly algorithm for photovoltaic maximum power point tracking control under partial shading. *IEEE Journal of Emerging Selected Topics in Power Electronics*, 5(2), 661-671.
- [96] Alhaj Omar, F., & Kulaksiz, A. A. (2021). Experimental evaluation of a hybrid global maximum power tracking algorithm based on modified firefly and perturbation and observation algorithms. *Neural Computing and Applications*, 33(24), 17185-17208.